In compliance with the
Canadian Privacy Legislation
some supporting forms
may have been removed from
this dissertation.

While these forms may be included
in the document page count,
their removal does not represent
any loss of content from the dissertation.

University of Alberta

Condition monitoring scheme based on stator current spectrum analysis for a random wound medium size skewed induction motor

by

Sergio Paulo Bertani Hernandez

A thesis submitted to the Faculty of Graduate Studies and Research in partial fulfillment of the requirements for the degree of **Master of Science**.

Department of Electrical Engineering

Edmonton, Alberta

Fall 2003

National Library of Canada
Acquisitions and Bibliographic Services
395 Wellington Street
Ottawa ON K1A 0N4
Canada

Bibliothèque nationale du Canada
Acquisisitons et services bibliographiques
395, rue Wellington
Ottawa ON K1A 0N4
Canada

Your file Votre référence
ISBN: 0-612-87721-3
Our file Notre référence
ISBN: 0-612-87721-3

The author has granted a non-exclusive licence allowing the National Library of Canada to reproduce, loan, distribute or sell copies of this thesis in microform, paper or electronic formats.

The author retains ownership of the copyright in this thesis. Neither the thesis nor substantial extracts from it may be printed or otherwise reproduced without the author's permission.

L'auteur a accordé une licence non exclusive permettant à la Bibliothèque nationale du Canada de reproduire, prêter, distribuer ou vendre des copies de cette thèse sous la forme de microfiche/film, de reproduction sur papier ou sur format électronique.

L'auteur conserve la propriété du droit d'auteur qui protège cette thèse. Ni la thèse ni des extraits substantiels de celle-ci ne doivent être imprimés ou aturement reproduits sans son autorisation.

Canada

University of Alberta

Library Release Form

Name of Author: Sergio Paulo Bertani Hernandez

Title of Thesis: Condition monitoring scheme based on stator current spectrum analysis for a random wound medium size skewed induction motor

Degree: Master of Science

Year this Degree Granted: 2003

Permission is hereby granted to the University of Alberta Library to reproduce single copies of this thesis and to lend or sell such copies for private, scholarly or scientific research purposes only.

The author reserves all other publication and other rights in association with the copyright in the thesis, and except as herein before provided, neither the thesis nor any substantial portion thereof may be printed or otherwise reproduced in any material form whatever without the author's prior written permission.

Date: September 26th, 2003

University of Alberta

Faculty of Graduate Studies and Research

The undersigned certify that they have read, and recommend to the Faculty of Graduate Studies and Research for acceptance, a thesis entitled **Condition monitoring scheme based on stator current spectrum analysis for a random wound medium size skewed induction motor** submitted by Sergio Paulo Bertani Hernandez in partial fulfillment of the requirements for the degree of **Master of Science**.

Date: 19 September 2003

Abstract

As the workhorse of industry, the induction motor is extensively used and it represents a critical component in many industrial processes. Condition monitoring based on stator current spectrum analysis represents a low-cost, non-invasive and powerful method to monitor the motor's condition. This thesis focuses on identifying bearing related faults using stator current monitoring in a medium size induction motor. The airgap flux density distribution of the machine is analyzed to study the effects of stator and rotor slotting and skewing the rotor bars. Airgap eccentricity conditions are also included. A test rig designed specifically to introduce different degrees of airgap static eccentricity is explained. Simulation results, which verify these conditions in the spectrum, along with experimental work are discussed. The results indicate that current condition monitoring may be suitable for implementation in different industrial environments and its application may bring significant benefits for optimal performance of the induction motor.

To my parents:

Claudio and Esperanza.

You have been of constant admiration in my life.

To my siblings:

Claudia

Claudio

Melissa

Monica

David

Your support and encouragement throughout my professional preparation has been exceptional.

I Love you all, my dear family.

Acknowledgements

- I would like to express my sincere gratitude to my supervisor Dr. Andy Knight. His guidance, patience and assistance throughout the completion of my master's program has been exceptional. I am truly blessed for the opportunity he provided me to reach one of my desired goals: to live and study in Canada.

- I wish to sincerely thank the CONACYT (Consejo Nacional de Ciencia y Tecnologia) for providing the financial support for my graduate program. They have enabled me to have a remarkably positive experience studying abroad.

- I also want to thank the members of my supervisory committee, Dr. John Salmon and Dr. Ming Zuo for taking the time to review my thesis work.

- I am grateful for all the encouragement, love and support that my family has provided me throughout my professional education. God bless you.

- My dear Stephanie, I deeply appreciate all your time and dedication to help me edit my thesis. You have been a great source of encouragement, patience and love.

- I am really thankful for all my good friends in the faculty, especially Glenn Peters, Albert Terheide and Aisha Yahya who have been more than willing to help me and provide me with advice. Thank you Donna Neustaeter for all your prayers toward the completion of my program and my living in Edmonton.

Contents

1 Introduction 1

1.1 The Induction Motor: Workhorse of Industry 1

1.2 Machine Condition Monitoring 2

1.3 Fault Detection 3

1.4 Electrical Machines Faults 5

1.4.1 Stator faults 5

1.4.2 Rotor faults 7

1.4.3 Bearing faults 8

1.5 The Monitoring Strategy 8

1.6 The Type of Motor 9

1.7 Research Objective 10

1.8 Research Approach 10

2 Condition Monitoring Methods and Diagnosis in Induction Motors 12

2.1 Monitoring Methods 12

2.1.1 Vibration monitoring 13

2.1.2 Flux monitoring 14

2.1.3 Temperature monitoring 15

2.1.4 Current monitoring 16

2.2 Fault Identification 17

2.2.1 Rotor faults detection: broken bars 17

2.2.2 Load effects 18

2.2.3 Stator fault detection 19

2.3 Signal Processing Analysis 20

2.3.1 Signals and time series 20
2.3.2 Fourier analysis 21
2.3.3 Fourier series 21
2.3.4 The fast Fourier transform 22
2.3.5 Power spectrum 23
2.3.6 Sampling and windowing 23

3 Mechanical Irregularities in Induction Motors 26
3.1 Rolling Element Bearing Faults 26
3.1.1 Bearing schematic 28
3.1.2 Characteristic bearing frequencies 28
3.1.3 Misalignment 30
3.2 Airgap Eccentricity 30

4 Motor Theoretical Anaylsis 35
4.1 The Induction Motor Structure 35
4.2 Magnetic Flux Density 37
4.3 Slot Geometry 38
4.4 Windings 38
4.5 MMF Calculation 40
4.5.1 The rotating magnetic field 42
4.6 Winding Factors 47
4.7 The MMF of a 3-Phase Winding 49
4.8 Airgap Field Flux Density 50
4.8.1 Airgap slot harmonics 55
4.9 Rotor Eccentricity 61
4.10 Flux Density Harmonics 65
4.11 The Reference Frame 65
4.11.1 The MMF of squirrel cage rotor 67
4.12 The Skewed Rotor 70
4.13 Summary 70

5 Simulations **72**

5.1 Permeance Model Calculation and Skew Effect 72

5.2 Simulation Results 77

5.3 Summary 82

6 Experimental Test Rig **83**

6.1 Experimental Setup 83

6.2 Induction Motor Characteristics 84

6.2.1 New housing bearings 85

6.3 Data Acquisition 86

6.4 Labview: Monitoring Graphic Interface 89

7 Experiment Results **93**

7.1 Experiments Classification 93

7.2 Experiments and Evaluation 94

7.2.1 Healthy motor 94

7.2.2 Step harmonics 96

7.2.3 Load effects and rotor asymmetries 103

7.2.4 Rotor slot harmonics (RSH) 105

7.3 Faulty Motor 105

7.3.1 Airgap eccentricity 105

7.3.2 Introduction of static eccentricity by rotor radial movement . 109

7.3.3 Low frequency harmonics 110

7.3.4 Rotor slot harmonics 119

7.3.5 RSH with time harmonics 119

7.3.6 Experimental work with a damaged bearing 124

8 Conclusions and Future Work **129**

Bibliography **132**

List of Figures

1.1 Various schemes to integrate a MCM system 3
1.2 Failure percentage of all induction motor components (IEEE/EPRI/Thorson survey) 6

2.1 A simple piezoelectric accelerometer [1] 14
2.2 A search coil in the stator slots 15

3.1 Bearing schematic 28
3.2 Bearing geometry 30
3.3 Misalignment of the bearing [2] 31
3.4 Static eccentricity 32
3.5 Dynamic eccentricity 33
3.6 Static and dynamic eccentricity 34

4.1 Induction motor components 36
4.2 Airgap and slot openings 38
4.3 Air gap magnetic field of a coil placed in a flat air gap 40
4.4 Magnetic field intensity variation of a single coil placed along the air gap 41
4.5 Single layer 3 phase primitive machine and resultant MMF 43
4.6 MMF space traveling wave along the airgap 51
4.7 MMF traveling wave in space and time 52
4.8 MMF space traveling wave along the airgap (physical arrangement) . 53
4.9 Variation of air gap flux density due to slotting in one side of the air gap. 54
4.10 Stator and rotor slots harmonics as function of $f_{1,2}(\alpha)$ 58
4.11 Airgap flux density 59

4.12 Rotor eccentricity 62
4.13 Reference frame 66
4.14 Rotor MMF space traveling wave along the airgap 69
4.15 Skewing of rotor slots 70

5.1 Skewing of rotor slots and fragmentation 74
5.2 Simulated airgap flux density FFT spectrum with 0% eccentricity . . 77
5.3 Low frequencies of the flux density FFT spectrum seen from the stator reference frame for both a skewed and an unskewed rotor 79
5.4 Low frequencies of the flux density FFT spectrum seen from the rotor reference frame for an unskewed rotor 79
5.5 Effect of skewing the rotor bars in the rotor slot harmonics of the flux density spectrum 80
5.6 Comparison of the rotor slotting harmonics when different percentages of static eccentricity are introduced in the motor seen in the stator reference frame 81
5.7 Comparison of the stator slotting harmonics when different percentages of static eccentricity are introduced in the motor seen in the rotor reference frame 81

6.1 Test rig basic representation 84
6.2 Experimental test rig 84
6.3 Stator winding configuration 85
6.4 AutoCAD design of the bearing housing 87
6.5 New bearing housing 87
6.6 Bearing housing components 87
6.7 Current monitoring scheme 88
6.8 Data measurement and waveform screen 90
6.9 FFT signal processing screen 91
6.10 Search coil screen and signal processing 92

7.1 PSD current spectrum for healthy motor at different load levels . . . 97

7.2 PSD Current spectrum for healthy motor at different load levels. Left, low frequency sidebands around the fundamental at $\pm\omega_r$ ($\approx$ 30 & 90 Hz). Right, rotor slot harmonics. The frequency value is indicated by the grid of the plot 98
7.3 PSD Current spectrum for healthy motor at different load levels. Stator slot harmonics 99
7.4 Current spectrum for healthy motor: Stator step harmonics 101
7.5 Current spectrum for healthy motor: Rotor step harmonics 102
7.6 PSD current spectrum for a healthy motor: Rotor asymmetry and load effects harmonics 104
7.7 Rotor slot frequency components in the PSD current spectrum at No Load 106
7.8 Rotor slot frequency components in the current spectrum at Half Load 107
7.9 Rotor slot frequency components in the current spectrum at Full Load 108
7.10 Low frequency components at 0%, 22%, 36% and 54% static eccentricity. No load with $n = 1$ and $k = 1, 3, 5$ 112
7.11 Low frequency components at 0%, 22%, 36% and 54% static eccentricity. Half load with $n = 1$ and $k = 1, 3, 5$ 113
7.12 Low frequency components at 0%, 22%, 36% and 54% static eccentricity. Full load with $n = 1$ and $k = 1, 2, 3, 4, 5$ 114
7.13 Low frequency components at 0%, 22%, 36% and 54% static eccentricity. Half load with $n = 3$ and $k = 1, 3, 5$ 116
7.14 Low frequency components at 0%, 22%, 36% and 54% static eccentricity. Full load with $n = 3$ and $k = 1, 3, 5$ 117
7.15 Variation in magnitude of the low frequency components obtained from $\omega \pm k\omega_r$ when the motor is running at no load, half load and full load conditions and with different percentages of static eccentricity 118
7.16 First RSH and sidebands at No Load 120
7.17 First RSH and sidebands at Half Load 121
7.18 First RSH and sidebands at Full Load 122

7.19 Variation in magnitude of the first $RSH_{n,p}$ and their sidebands at $\pm\omega_r$ when the motor is running at no load, half load and full load conditions and with different percentages of static eccentricity 123
7.20 RSH with different combinations of time harmonics n and integer k . 125
7.21 Comparison of the low frequency components when a damaged bearing and 54% eccentricity is introduced in the motor 127
7.22 Comparison of the RSH positive sidebands when a damaged bearing and 54% eccentricity is introduced in the motor 128

1 Bearing housing drawing a) 142
2 Bearing housing drawing b) 143
3 Bearing housing drawing c) 144

List of Tables

4.1 MMF spatial and time harmonics combinations 46
4.2 Stator and rotor slots parameters 56
4.3 Stator and rotor slots harmonic coefficients for $v = 0, 1, 2, \ldots, 14, 15$. 57
4.4 Airgap flux density components in the rotor reference frame 67
4.5 MMF spatial and time harmonics combinations for a squirrel-cage rotor winding 68
4.6 Summary of equations to determined the set of frequencies identifiable in the current spectrum: slotting and airgap eccentricities 71
4.7 Summary of equations to determined the set of frequencies identifiable in the current spectrum: step harmonics and rotor speed 71

5.1 Motor data 73
5.2 Low frequency harmonics seen in the spectrum 78
5.3 Rotor and stator slot harmonics 80

6.1 Motor data 86

7.1 Motor paramenters and conditions 95
7.2 Frequency values for a healthy motor 100
7.3 Step harmonics frequencies (Hz) 100
7.4 Rotor asymmetries and load effect harmonics 103
7.5 Rotor slot harmonic frequencies 109
7.6 Frequencies components at $n\omega \pm k\omega_r$ 111
7.7 Rotor slot harmonic frequencies 124

List of Symbols

A_n, B_n	n^{th} harmonic component of the Fourier series
BD	ball diameter
B	Flux density
b_{os}	stator slot opening
b_{or}	rotor slot opening
dB	decibels
e	voltage induced
I_{nb}	current component of the rotor's asymmetry
I_e	fundamental current component
f_1	fundamental supply frequency
f_b	rotor broken bars frequency
f_e	line frequency (60 Hz)
f_{ecc}	eccentricity frequency
f_i	inner race bearing frequency
f_k	rotor asymmetry frequency
f_{load}	load effects frequencies
f_{bng}	bearing frequencies seen in the current spectrum
f_o	outer race bearing frequency
f_r	rotor rotational speed
f_{rsh}	rotor slot harmonic frequency
f_{ssh}	stator slot harmonic frequency
f_s	sampling frequency
f_{sp}	ball spin frequency
f_c	cage frequency

f_{tt}	axial flux component frequency
f_v	stator voltage frequency component after switch off
H	magnetic field intensity
k, v	harmonic index
k_{dn}	winding distribution factor
k_{pn}	winding pitch factor
k_{wn}	winding factor
k_c	Carter factor
m	number of phases
n	number of bearing balls
n_b	number of contiguous rotor broken bars
N	number of turns in a coil
N_r	number of rotor slots
N_s	number of stator slots
o	slot opening
p	number of pole pairs
$P(\alpha)$	permeance function
PD	pitch diameter
q	number of slots per pole per phase
s	slip
t	time
t_d	slot pitch
W	number of turns per phase
W_c	number of turns per coil
α	mechanical angular position
α_{el}	angular distance between slots
β	ball bearing contact angle
δ	airgap
$\epsilon_{s,d}$	degree of static or dynamic eccentricity
γ	electrical angular displacement
ω_o	fundamental frequency
ω_e	electrical fundamental frequency

ω_r	rotor angular velocity
τ_p	pole pitch
μ	permeability constant
μ_o	permeability of free space
μ_r	relative permeability constant

Chapter 1

Introduction

This chapter presents an overview of the induction motor and the importance of machine condition monitoring for fault detection which provides background information for this research. This is followed by the rationale for the monitoring strategy and type of induction motor chosen. Finally, the research objective and approach is described.

1.1 The Induction Motor: Workhorse of Industry

The induction motor is the most common electrical motor and is known as the workhorse of many modern industrial processes [3]. Since its conception and development in the late 1800's, the induction motor has been the most reliable machine to convert electricity into mechanical power. Most induction motors are fed from three-phase or single-phase power grids; however, advances in asynchronous motor control technology allowed motors to be supplied through adjustable frequency drives to provide variable speed and torque control capabilities. As a result, their usage in higher performance applications has developed [4].

An induction motor represents a critical component in many industrial processes. As previously mentioned, its use is extensive as it has a number of advantages when compared to other electrical machines of its kind. Benefits of this machine include: a simple rugged construction, low cost, high efficiency and straightforward maintenance. In an industrialized nation, induction motors can typically consume between 40 to

50% of all the generated electrical capacity of that country [5].

Like all motors, induction motors are subject to gradual deterioration. Under certain operating conditions, the induction motor can be under significant physical, thermal and electromechanical stresses for long periods of time. Different internal motor faults (e.g. inter-turn short circuit, broken rotor bars, worn bearing) along with external stresses (e.g. mechanical overload, locked rotor, supply unbalance) are possible during the lifetime of the machine. Hostile environments, misoperation and manufacturing defects can lead to the progression of incipient faults leading to a breakdown of the motor and consequent expensive downtime. Hence, a condition monitoring scheme is desirable to identify on time any potential failure.

1.2 Machine Condition Monitoring

Machine Condition Monitoring, MCM, is the basis of many maintenance techniques known as preventive, predictive, proactive or reliability based [6]. Condition Monitoring is defined as a continuous or periodical evaluation of the health-state of the machine throughout its operative life and involves the collection and assessment of various signatures such as temperature, current, vibration, pressure, flow, etc. without the interruption of its operation [6].

Condition monitoring is applied as a diagnostic tool of electrical machines that allows the acquisition of information regarding the status of its operation and performance. Hence, a condition monitoring system represents a very important factor to achieve efficient and profitable operation of a large variety of industrial processes [7]. Planned maintenance strategies using condition monitoring have been used in industry for many years to ensure that motor faults are kept to a minimum [8]. Knowledge of the health-state of the machine can be obtained by carefully analyzing the monitored parameters. MCM provides information on various forms of damage and can recognize the development of malfunctions and asymmetries at an early stage, preventing potential breakdowns. By continuously monitoring the system, the condition of equipment is known and readily available. A warning signal can be released prior to any failure. This allows for advanced planning of maintenance tasks and replacement of failing components at optimum periods. As a result, diagnosis and prognosis

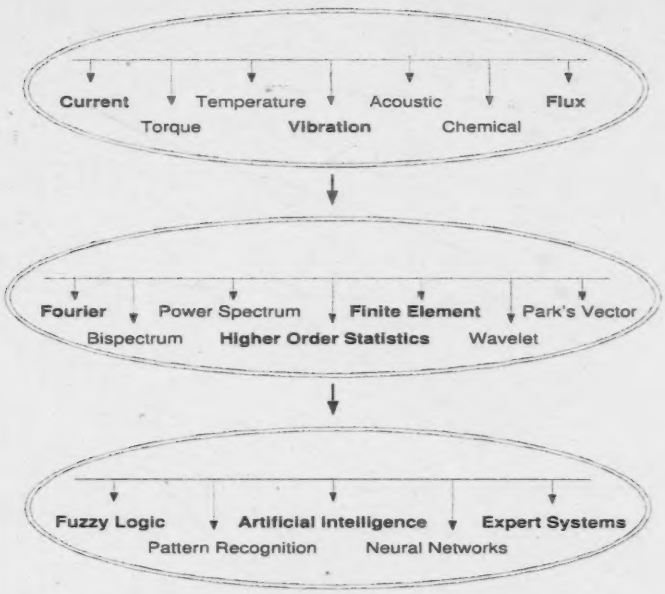

Figure 1.1: Various schemes to integrate a MCM system

of the condition permits properly planned preventive equipment maintenance that could be carried out during scheduled downtimes, averting upset deadlines and heavy financial losses [7, 9]. Research into condition monitoring is quite diverse, in both applications and the approaches necessary for implementation. Figure 1.1 illustrates various schemes that can be used to integrate a MCM system to diagnose the health of an electrical machine.

1.3 Fault Detection

A fault is defined as a deviation of one characteristic property from the acceptable, usual or standard condition of a system. Fault detection aims at recognizing abnormal behavior of components or processes through inherent faults based on measured signals. Measurable signals are acquired by sensors located in the system and these signals are used to monitor its condition. Faults can show up with an abrupt, incipient or intermittent behavior. Faults may lead to a failure, which might cause a permanent interruption of a required function. Fault diagnosis uses processed signals

to determine the kind of faults, their magnitude and location [10].

Traditional methods for condition monitoring and fault-detection in induction motors are mainly based on the analysis of several measurable quantities by carrying out different signal processing techniques. The well-known methods applied to electrical motors include analysis techniques such as the Fast Fourier Transform (FFT), Power Spectrum Density (PSD), higher order statistical analysis, wavelet decomposition, Park's vector approach and bispectrum. These methods can be applied to records of measurements from the motor [2, 11, 12].

A variety of sensors can be used to collect these measurements from an induction motor. These sensors may measure stator voltages and currents, airgap and external magnetic flux densities, rotor position and speed, output torque, internal and external temperature or bearing vibrations [13]. Thus, a robust condition monitoring system can monitor and identify a variety of motor failures.

Condition monitoring methods are often categorized as being invasive or non-invasive. Invasive monitoring techniques involve dissembling the motor for the purpose of introducing specific transducers or to conduce a visual inspection. A drawback of invasive methods is that the machine has to be stopped for installation and maintenance of the sensors which sometimes are delicate and expensive. On the other hand, cost reduction relies on continuous operation of the motor system. Non-invasive monitoring techniques allow the operator to know the motor's health while the motor is running in normal operating conditions, without stopping it for the placement of sensors. As a result, on-line, non-invasive techniques for fault detection are preferred over invasive techniques since they allow continuous system monitoring under all operating conditions with minimum disturbance.

In general, there exist several non-invasive and invasive monitoring techniques that are applicable for condition monitoring of induction motors. The most common ones include [9, 13]:

a) Electromagnetic field monitoring

b) Temperature measurement

c) Infrared recognition

d) Radio Frequency (RF) emissions monitoring

e) Noise and vibration monitoring

f) Chemical analysis

g) Acoustic noise measurement

h) Motor current spectrum analysis

A further discussion of a), b), e) and h) will be presented in chapter no. 2 as these are the most frequently used monitoring techniques.

1.4 Electrical Machines Faults

Electrical machines are exposed to a wide variety of scenarios and conditions. Deterioration and consequent failure is probable if the machine is not properly monitored and evaluated. The majority of all failures in an electrical machine are caused by a combination of stresses that act on three principal motor components: the stator, rotor and bearings [7, 9, 14]. The stresses can be grouped as thermal, electrical, mechanical and environmental. Figure 1.2 shows the breakdown of induction motor component failures reported by IEEE (Institute of Electrical and Electronics Engineers), EPRI (Electric Power Research Institute) and Thorson [15]. A brief discussion of the failures encountered in induction motors follows.

1.4.1 Stator faults

Stator failures in induction motors represent around 30% of all reported problems. [16]. These faults are usually related to insulation failure. The winding insulation system in the motor is under severe strain during continuous operation of the machine. Lifetime of the insulation is reduced when an increase in temperature on the windings is present. As a rule of thumb, for every 10^oC above normal temperature, the insulation life is halved. Once the insulation system has lost its physical integrity, it will no longer resist the normal dielectric, mechanical and enviromental stresses leading to a consequent winding failure [14].

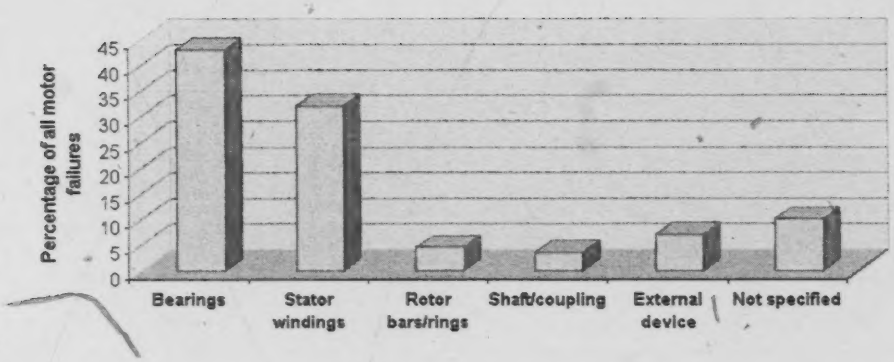

Figure 1.2: Failure percentage of all induction motor components (IEEE/EPRI/Thorson survey)

Voltage variations also affect the motor performance and the winding insulation. A small amount of voltage unbalance may cause significant increase in the winding temperature. Cycling or repeated starts of the motor produce a similar effect. Overloading and obstructed ventilation in the machine generate excessive heat that may produce severe damage in the windings. In addition, stator failures caused by electrical stresses may develop as phase-to-ground or phase-to-phase faults. It is assumed that these faults start as undetected turn-to-turn faults that eventually expand and cause a major problem [9].

Presently, there exist a number of techniques to detect these faults. For large generators and motors rated above 4kV, on-line Partial Discharge (PD) test methods give reliable results [17]. For low-voltage motors, stator fault detection could be achieved by using methods such as axial flux monitoring [18] or stator terminal voltage monitoring after switch off [16]. Stator current monitoring is a further technique that may be applied. Thomson [19] has demonstrated that shorted turns in 2 and 4 pole, low voltage, squirrel cage induction motors can be identified by looking at specific frequency components of the current spectrum.

1.4.2 Rotor faults

The most common type of induction motor has a squirrel cage rotor where cast aluminum conductors or copper bars are shorted together at both ends by end rings of the same material. A poor casting during the manufacturing process may introduce air bubbles along the bars resulting in poor conduction or a "broken bar". This defect may not be detected during normal operation as the motor may continue to give acceptable performance but with lower efficiency [14]. Rotor related problems represent around 10 % of the failures among utility-size squirrel cage induction motors [13, 20]. Broken rotor bars or end rings along with rotor eccentricities are the main asymmetries encountered in the rotor. In the case of rotor broken bars, the machine can keep operating but the number of broken bars will inevitably increase, reaching the limits of safe operating conditions. Therefore, a reliable diagnostic technique to monitor the machine condition is beneficial.

Thermal overloading and thermal unbalance effects also lead to rotor failures. These thermal stresses are mainly caused by the following:

1. Abnormal number of consecutive starts generating excessive bar temperature
2. Unbalanced phase voltages producing skin effect and consequent surface heating
3. Insufficient ventilation inside the machine, generating hot spots
4. Smeared laminations or poor shorting of the bars leading to excessive losses

Similarly, magnetic stresses generate electrodynamic forces that in turn produce vibration, a consequent deflection or bending and possible rupture of the bar. Due to inherent asymmetries and eccentricities in the airgap, an unbalanced magnetic pull (UMP) may cause the rotor to bend and strike the stator core, damaging the machine. Pulsating mechanical loads such as reciprocating compressors can subject the rotor cage to high mechanical stresses. Similarly, environmental stresses originating from contamination, corrosion or abrasion of the rotor material due to a chemical or moisture may lead to an eventual fatigue of the rotor and possible failure [14].

During recent years, much of the work to detect faults in induction motors has been focused on rotor bar failure. Different monitoring techniques already exist to

identify broken rotor bars or end rings in squirrel cage induction motors. Vibration monitoring, axial flux and stator current monitoring are the most prominent methods to accomplish such a task. A considerable amount of work has been published in literature regarding the usefulness, reliability and low cost of stator current monitoring to identify rotor related problems. Thomson [5, 13] has presented several on-site case histories, confirming its industrial applicability.

1.4.3 Bearing faults

The rolling element bearing is a widespread component in industrial rotating machinery and over 40% of rotating electrical machinery failures can be attributed to bearing failure [1]. Hence, the rolling element plays an important role in the operation of the machine. Briefly, when a ball of the bearing passes a defect spot on the race, the clearance between the inner and outer race grows allowing a radial movement of the rotor. This radial movement changes the air gap of the motor generating an increase of eccentricity. A high degree of eccentricity increases the UMP and therefore the tendency to increment the radial movement of the rotor. Thus, subsequent damage of the bearing may be produced that in turn could lead to potential rotor to stator rub and motor breakdown.

Bearing faults might manifest themselves as a rotor asymmetry and/or an eccentricity related problem. Bearing faults are usually distinguished by means of flux-based measurements and vibration analysis. Stator current spectrum analysis has been implemented to detect airgap eccentricities in large machines, but little work has been reported in the literature regarding the detection of bearing problems using motor current techniques [2].

1.5 The Monitoring Strategy

Most electric motor failures interrupt a process and reduce production leading to substantial losses. A significant amount of research to provide better condition monitoring strategies has been done in order to prevent sudden motor failures, especially in ac induction motors.

Flux monitoring schemes by means of search coils in the stator slots, rotor shaft or end coils give significant information of the health-state of the machine [9]. However, its practical application is generally limited since it requires a shutdown of the motor and corresponding down-time to install the sensors.

On-line vibration monitoring schemes are often used solely in large machines since its implementation is only cost effective for this size of machinery. Vibration monitoring for low-voltage electrical machines is carried out by a portable signal analyzer. The equipment and the vibration transducers are expensive and therefore, care should be taken for mechanical installation and transmition of the signal [21]. Similar problems exist with other sensors such as temperature or speed. Hence, implementation and analysis of invasive techniques might be expensive and delicate.

Stator current spectrum analysis is considered a powerful, non-invasive and low cost technique for monitoring the health of three-phase induction motors [5]. A significant amount of information can be extracted from the current signals which can be easily accesed for condition monitoring and control purposes [21]. In fact, current sensors can often be found already in place (e.g. drives, motor control centers). For these reasons, stator current monitoring has been chosen for this research.

As previously mentioned, the detection of stator and rotor failures by means of current monitoring has been demonstrated in literature [5, 19, 20, 21]. However, the majority of previous research has been dedicated to detect airgap eccentricity problems in large machines [8] with little work presented regarding the detection of bearing problems and airgap eccentricities in medium size industrial motors [2].

1.6 The Type of Motor

Various industrial case histories have illustrated that a proper integration of stator current monitoring in an industrial environment could offer a reliable diagnostic strategy to identify stator, rotor and bearing related problems [8, 19, 22, 23, 24, 25]. However, much of this work does not consider medium size random wound skewed squirrel cage induction motors which are the predominant type used in industry. Therefore, this thesis focuses on this type of motor. Medium size low voltage induction motors normally have a random-wound winding and are built for voltages below 1kV. For

the purpose of this work, motors within 1-200 HP as described in NEMA-MG1 are targeted.

A random wound winding is made of coils of multiple strands per conductor randomly packed in a round wire. There are two types of random wound windings. The first type is concentric wound. This type is usually used in NEMA frame sizes ≤ 440 and the coils are placed in the stator slots in a single layer configuration. The second type consist of distributed coils that may be placed in slots in a double layer configuration and is typical for NEMA frame sizes above 440 [26]. The end connections of the coils are arranged in several ways designated as lap or wave windings. The squirrel cage can be composed of unskewed or skewed bars. A skewed squirrel cage is often used since it helps to reduce the magnitude of certain harmonic components, limiting pulsating torques and reducing audible noise that can arise from slotting effects.

1.7 Research Objective

This research examines the advantages of using stator current spectrum analysis as a non-invasive, reliable and inexpensive method for an on-line computer-based machine condition monitoring strategy to identify mechanical faults such as airgap eccentricty and worn bearings in a medium size skewed rotor induction motor.

The research objective is to study, understand and interpret the frequency components of the motor's stator current spectrum in order to project a suitable application for an on-line monitoring system by making use of LabView as the data acquisition and signal processing software.

1.8 Research Approach

A low-cost condition monitoring system for fault detection is desirable. This thesis concentrates on mechanical irregularities of an induction motor such as bearing faults and airgap eccentricity as these faults represent around 40% of machine failures. In addition, current monitoring has not been extensively researched as a reliable and inexpensive technique for condition monitoring of mechanical faults in induction motors of this size. Therefore, it is of interest to analyze the ability of current monitoring as

detection technique to identify a known fault.

The approach for obtaining the results is as follows:

1) Design and specify a motor test rig for the purpose of measurement and analysis of a created known fault. This test rig consists of an induction motor loaded to a DC generator via a flexible coupling. The end plates of the machine are modified and the bearing housings are arranged to adjust the rotor radial position with respect to the stator in order to introduce different levels of static airgap eccentricity in the system. A detailed description of the test rig is presented in chapter no. 6.

2) Make use of a signal conditioner system such as LabView to sample and collect on-line information from the stator current of a healthy motor. In addition, on-line information of a motor in various degrees of static eccentricity and with a damaged bearing during normal and steady state operation is collected. Transient situations were left out from the scope of this work because condition monitoring is usually implemented during normal operation.

3) Analyze and evaluate the data based on a model of the permeance function of the machine's airgap. A program created in Matlab computes the model and simulates the motor's performance in order to identify the frequency components related to eccentricity problems. The code of this program is found in appendix A.

Based on the information obtained, stator current spectrum analysis for mechanical fault detection in an induction motor is evaluated.

Chapter 2

Condition Monitoring Methods and Diagnosis in Induction Motors

A successful condition monitoring scheme relies on the availability of information that allows the diagnosis of a motor's condition and the prognosis of its future state. Condition monitoring techniques have been continuously developed over the years, resulting in a range of available methods for detection and diagnosis of failures in machinery. Stator, rotor and bearing failures in the motor are frequently identified using methods such as vibration, electromagnetic field, temperature and current monitoring. A brief description of their application and an overview of the signal processing technique used for this research is given next.

2.1 Monitoring Methods

Modern monitoring techniques in combination with different data processing and acquisition methods make use of spectral analysis to determine the condition of the motor according to the apparition of certain frequency components or their change in magnitude. The most common monitoring techniques for induction motor that may utilized the results of spectral analysis are described as follows.

2.1.1 Vibration monitoring

Machine vibrations result from a complex combination of effects caused by a variety of internal sources. An ideal motor would generate minimal vibration when operating. Thus, vibration signals are measured and analyzed to provide a method for diagnosing possible development of a faulty condition. Vibration monitoring is the most widely used method in industry for detection and diagnosis of rolling element bearing problems, gear mesh defects and rotor related malfunctions such as misalignment and mass unbalance [27]. In general, the large majority of problems in rotating machinery are caused by faulty bearings. Therefore, vibration monitoring is mainly used to identify bearing problems. Vibration measurements are taken directly (radially or axially) from the bearing housing of the motor since the forces from the shaft are transferred through the rolling elements to the bearing outer race and then ultimately to the bearing housing. The quality of any measured vibration signal will depend on the sensor location, sensor mounting, sensor performance and the selection of parameters to be measured such as acceleration, velocity or displacement.

The sensor of choice for most vibration data collection on industrial machinery is a piezoelectric accelerometer. Figure 2.1 shows the construction of a simple piezoelectric accelerometer. An inertial mass is separated from the frame by piezoelectric discs and the assembly is pre-loaded by the clamp nut. When the device is attached to a vibrating surface the acceleration forces of the mass are applied to the piezoelectric discs which produce an electric output signal proportional to the compression forces and consequently proportional to the absolute acceleration of the vibrating surface. The output signal is proportional to acceleration, however it is often integrated once or twice to display units of velocity (in/s) or vibration displacement, respectively [1].

Vibration analysis provides evidence of the bearing condition and allows the operator to know when a bearing needs to be replaced to avert machine failure. The vibration signals obtained are subjected to frequency analysis and compared to the harmonic frequency components of a healthy machine. Abnormal machine conditions are revealed by the increase of amplitude of those frequency components that are above normal reference frequencies [7]. It is possible to distinguish various fault conditions in an electrical machine by observing and detecting the dominant frequencies

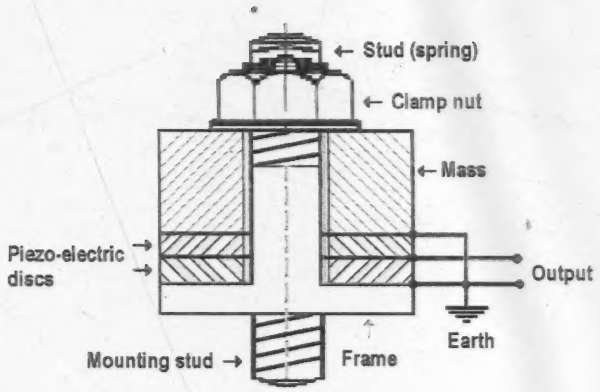

Figure 2.1: A simple piezoelectric accelerometer [1]

caused by these faults.

Existing on-line vibration monitoring equipment is very expensive and its installation is only cost-effective in very large machines (i.e., multi-Megawatts generators). Consequently, it is standard practice to observe bearing vibrations by a permanent monitoring scheme mainly in large machinery. Vibration monitoring for medium size induction motors is generally carried out periodically by a condition monitoring portable data collector which provides low-cost monitoring.

2.1.2 Flux monitoring

The magnetic field in the motor's airgap can also be monitored to predict mechanical abnormalities. During normal conditions, ideally the airgap flux varies sinusoidally both in space and time, however the presence of some stator and rotor faults may cause deviations of such sinusodial variation [22]. Search coils placed in the stator slots of the motor can sense the airgap magnetic flux. Spectrum analysis of the induced electro-motive force (EMF) can provide the frequency components related to a faulty condition. A search coil consists of a conductor wire of N turns that encloses a known area. The flux linkage is measured with the coil according to the induced voltage at the terminals. Figure 2.2 depicts a search coil positioned around one tooth of the stator slots.

In industrial installations, the insertion of a series of search coils in the stator

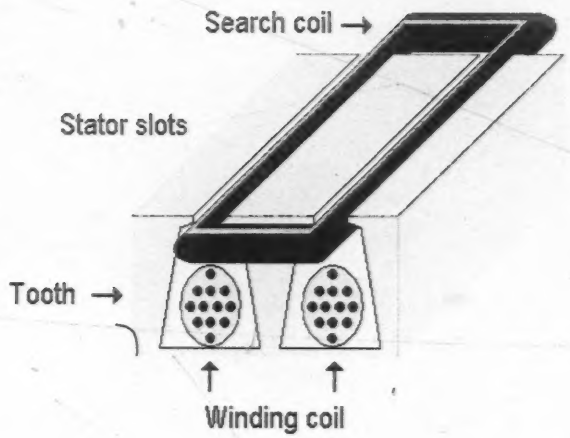

Figure 2.2: A search coil in the stator slots

slots represents a highly invasive monitoring technique and is not a practical option for motors already in situ. The placement of search coils in new motors is not widely considered since this requires approval of design modifications by the manufacturer and safety legislations authorities [25]. There are also practical problems due to the modern stator core and high voltage winding designs.

Monitoring magnetic flux in the airgap can provide significant information of the health-state of the motor but due to the practical reasons given, this technique has not been widely applied by the operators of medium size and large machines [25].

2.1.3 Temperature monitoring

Temperature monitoring is a simple and effective method for condition monitoring of electrical machines. It is often utilized as a primary tool to recognize irregular temperature conditions in the machine and it does not makes use of spectral analysis. An infrared, non-contact pyrometer is often used to detect abnormal hot spots, bearing problems, airflow and cooling problems in an induction motor [26]. Furthermore, this technique can make use of thermocouples and thermistors. Such devices give indications of gross changes inside the machine and are extremely effective if mounted and monitored in precise sites. Monitoring an increment in temperature on specified

components of the machine may lead to incipient problems that need to be identified before the machine breaks down. For example, a rise in bearing temperature might indicate incipient friction problems when checked on a routine basis [6, 22]. In industrial applications, this technique is widely used to monitor electrical drives and generators as a basic diagnostic tool or an alarm signal. A typical temperature monitoring system incorporates various channels for outputting signals to external alarms or protection relays by comparing an input signal with a predetermined set point value [6].

2.1.4 Current monitoring

Current monitoring utilizes results of spectral analysis of the stator motor current or supply current of an induction motor in order to identify an existing or incipient failure of the motor [2]. Fault detection based on stator current monitoring depends upon locating specific frequency harmonic components in the current spectrum that are related to mechanical or electrical asymmetries in the machine. The motor line current spectrum is influenced by many factors since the frequency components which are indicative of motor faults may be a function of load conditions, electric supply, noise, motor geometry, winding designs, speed, rotor and stator design and airgap variations.

The supply current may be monitored very easily without interfering with the machine, simply by fitting a clamp-on current probe around the supply cable of the motor. A great amount of information can be extracted from the stator current by applying signal processing techniques such as FFT, Bispectrum, High-resolution spectral analysis, Wavelet analysis or Park's vector approach. The characteristic spectral signature obtained may be used to distinguish potential failure modes of the machine by comparing it to the signature of normal operating conditions. The presence of any fault can be observed by looking at the change of magnitude of those frequency components related to any abnormal condition [28].

Clearly, stator current monitoring is a powerful monitoring tool that can provide information for fault detection without requiring access to the motor. The stator current is indeed a very convenient medium for measurement and diagnostic since

it is easily accessible. Current monitoring can be implemented inexpensively on the machines by use of a clamp-on current transformer and can be used for monitoring a number of remotely located motors.

Overall, current monitoring represents a low cost monitoring method when compared with vibration monitoring which is prohibitively expensive for small machines. Current condition monitoring for mechanical fault detection will be discussed extensively in chapter 3.

2.2 Fault Identification

A comprehensive condition monitoring scheme for an induction motor should recognize a fault in any of the three components: rotor, stator and bearing. In this section, a brief description to detect rotor asymmetries and stator failures is presented.

2.2.1 Rotor faults detection: broken bars

Current monitoring has been successfully applied to detect rotor circuit asymmetries [20, 29]. When a rotor fault exists, the flux distribution in the airgap of the machine is disturbed, resulting in a set of predicable frequencies in the line current given by [20]

$$f_k = f_e[\frac{k}{p}(1-s) \pm s] \tag{2.1}$$

and

$$f_b = f_e(1 \pm 2ks) \tag{2.2}$$

where, f_e is the line frequency (60 hz,), s is the slip of the motor, p number of pole pairs, $k = 1, 2, 3, \ldots$ is a harmonic index and due to normal winding configuration $k/p = 1, 5, 7, 11, \ldots$.

The most prominent of these frequencies appear at twice the slip frequency around the fundamental supply frequency and generally they are related to the presence of a broken rotor bar. Thus, the detection and severity of a broken bar relies on the measurement of the amplitude of these sidebands. Care should be taken to distinguish

those sidebands due to broken bars from other rotor asymmetries. Pulsating load and particular rotor design also cause sideband current components [29]. Therefore, the examination of higher harmonic amplitudes should be considered in order to confirm the presence of broken bars.

Kliman [20] carried out a field test on 23 plant motors to determine the relative distribution of magnitudes of the lower sideband (LSB1) of the line current in order to predict the severity of a damaged bar and establish a criterion of rotor health with a single measurement. A good motor may exhibit a LSB1 magnitude of ≤ -60 dB relative to the fundamental (60hz) component. A possible cracked bar will exhibit a LSB1 magnitude of ≤ -54 dB. A LSB1 magnitude of ≤ -50 dB may indicate the existence of a broken bar. In addition, Bellini et al and Benbouzid [2, 29] have presented a relationship that correlates the amplitude of the LSB1 and the severity of the fault with the number of broken bars. If a rotor breakage of n_b contiguous bars occurs, the relationship between the amplitude I_{nb} of the component caused by the electrical asymmetry and the amplitude I_e of the fundamental component is given by

$$\frac{I_{nb}}{I_e} \approx \frac{n_b}{N_r} \approx \frac{\sin \alpha}{2p\,(2\pi - \alpha)} \tag{2.3}$$

$$\alpha = \frac{2\pi\, n_b\, p}{N_r} \tag{2.4}$$

where N_r is the total number of rotor bars or rotor slots.

With stator current analysis it is possible to evaluate the general condition of the rotor cage, but if a noncontiguous number of damaged bars exists in the machine, current analysis may not be sufficient to evaluate the number of broken bars [15].

2.2.2 Load effects

If the load torque varies with rotor position such as with reciprocating compressors, the current spectrum may contain components which coincide with those caused by a faulty rotor. Torque oscillations in the load at multiples of the rotational speed mf_r will produce stator currents at frequencies of [30]

$$f_{load} = f_e \pm m f_r = f_e[1 \pm m\frac{(1-s)}{p}] \tag{2.5}$$

where $m = 1, 2, 3, \ldots$. Any varying-load torque results in stator current components that can obscure and often overwhelm those produced by a fault condition detected at frequencies given by equations 2.1 and 2.2. Therefore, any stator current fault detection scheme must rely on monitoring and identifying those spectral components which are not affected by load torque oscillations such as higher order harmonics not induced by the load [30].

2.2.3 Stator fault detection

Most low-voltage stator winding faults are due to insulation degradation. Winding faults on low-voltage motors cannot be diagnosed via online measurements such as partial discharges which are solely used in HV machines [19]. Early detection of inter-turn faults during motor operation would eliminate subsequent damage to adjacent coils and to the stator core. Penman et al. [18] utilized axial flux sensing as a technique to detect turn-to-turn faults in the stator of a low-voltage induction motor by using a large coil wound concentrically around the shaft of the machine. The location of the fault while the motor is operating was detected by mounting four coils symmetrically placed in the four quadrants of the motor. Ideally, the axial leakage flux is zero, but in practice, asymmetries exist in both the rotor and stator windings due to imperfection in the winding's geometry and manufacturing tolerances. Therefore, a small but measurable axial leakage flux is produced. The frequency components to be detected in the axial flux component are given by

$$f_{tt} = f_e(k \pm \frac{n(1-s)}{p}) \tag{2.6}$$

where p is the number of pole pairs, f_e is the supply frequency, $k = 1, 3$, s is the slip and $n = 1, 2, 3, \ldots, (2p-1)$.

Nandi and Toliyat [16] were able to detect inter-turn faults in the stator winding of induction motors by looking at the frequency components at the terminal line-to-line voltage after switch-off. Those harmonic components are given by

$$f_v = f_{off}[k(\frac{N_r}{p}) \pm 1] \tag{2.7}$$

where f_{off} is the frequency of the decaying stator voltage after switch-off and is proportional to the gradually diminishing speed of the induction motor and $k = 1, 2, 3, \ldots$.

Although axial flux monitoring represents a reliable method to detect inter-turn winding faults, it is not practical to industry since it is highly invasive to existing motors in service. As an alternative, Thomson [19] looked at the frequency components in the current spectra given by equation 2.6. He diagnosed shorted turns in random wound induction motors, based on the fact that these rotating flux waves can induce corresponding current components in the stator winding. As a result, it is stated that low frequency components should not be used as an indicator of shorted turns since they may be confused with inherent asymmetries of the machine, airgap eccentricities, winding geometry, misalignment and voltage unbalances. However, current monitoring has proved to be an instrument capable of localizing the frequency components due to an inter-turn fault for a given set of integers of k and n in equation 2.6 for any load condition.

2.3 Signal Processing Analysis

Signal Processing encompasses the processing, analysis and interpretation of data acquired by the sensor. Different signal processing techniques can be utilized to interpret the information obtained from the machine. Fourier analysis is the approach to signal processing in this thesis.

2.3.1 Signals and time series

Discrete-time signals are often generated through the process of sampling a continuous-time signal. This conversion entails changing a continuous-time signal into a number sequence which retains the essential features of that signal. A sequence that denotes a discrete-time signal can be represented in the following manner:

$$\mathbf{x} = \{x(t_n)\} = \{\ldots, x(t_{-2}), x(t_{-1}), x(t_0), x(t_1), x(t_2), \ldots\} \tag{2.8}$$

Each specific element $x(t_n)$ can be interpreted as the value of the discrete-time

signal $\mathbf{x}$ evaluated at the time instant t_n. The rate of sampling should be made in proportion to the rapidity with which the continuous-time signal varies as a function of time.

2.3.2 Fourier analysis

Fourier analysis is the primary tool to study sampled signals. Using the Fourier transform to convert time domain signals into the frequency domain, the significant characteristics of a signal are more easily recognized. The Fourier transform of a random real continuous-time signal with finite energy, denoted by $s(t)$ is defined as:

$$S(f) = \int_{-\infty}^{\infty} s(t) \exp^{-j\,2\pi ft}\, dt \tag{2.9}$$

and the inverse Fourier transform is specified by

$$s(t) = \frac{1}{2\pi} \int_{-\infty}^{\infty} S(f) \exp^{j\,2\pi ft}\, df \tag{2.10}$$

These two integral transforms allows us to examine a continuous-time signal in either the natural time domain or the auxiliary frequency domain.

2.3.3 Fourier series

Fourier analysis is the most common signal processing technique tool for analyzing a signal in the frequency domain. Spectral analysis is based on the frequency domain approach. Fourier analysis is based on the fact that any periodic function can be broken down into series of sinusoidal and cosinusoidal signals of harmonically related frequencies. The applications of Fourier analysis methods are perhaps the most widely used in the detection and diagnosis of machinery condition [1].

Fourier analysis through the use of the FFT and PSD are the signal processing techniques used in this research. Therefore, a brief overview is given in this section. Full details can be found in [31].

The trigonometric Fourier Series of a periodic continuous time signal $f(t)$ with period $2T$ is given by:

$$F(t) = \frac{1}{2} A_o + \sum_{n=1}^{\infty} (A_n \cos n\omega_o t + B_n \sin n\omega_o t) \tag{2.11}$$

where $\omega_o = \frac{\pi}{T}$ is the fundamental frequency. The Fourier coefficients A_o, A_n and B_n are given by:

$$A_o = \frac{1}{T} \int_{-T}^{T} f(t)\, dt \tag{2.12}$$

$$A_n = \frac{1}{T} \int_{-T}^{T} f(t) \cos n\omega_o t\, dt \quad for\ n = 1, 2, 3, ... \tag{2.13}$$

$$B_n = \frac{1}{T} \int_{-T}^{T} f(t) \sin n\omega_o t\, dt \quad for\ n = 1, 2, 3, ... \tag{2.14}$$

The coefficients A_n and B_n represent the amplitude of the n^{th} harmonic of the Fourier series. We can thus estimate any periodic function $F(t)$ as a collection of sine and cosine functions with the coefficients given above.

2.3.4 The fast Fourier transform

In digital computing applications, the discrete Fourier Transform (DFT) is used to compute the Fourier transform of a function from a given number of sampled values to identify the spectral or frequency content of the measured data. The signal $s(t)$ is first sampled with a sampling frequency f_s to give a sampled signal $s(n)$ with $n = 0, 1, 2, \ldots, N-1$. As it is seen, the signal data is of finite length as it must be in any practical application. Thus, the DFT, $S(\lambda)$, of $s(n)$ is expressed as:

$$S(\lambda) = \sum_{n=0}^{N-1} s(n) \exp^{-j\frac{2\pi}{N} n\lambda} \quad for \lambda = 0, 1, 2, \ldots, N-1 \tag{2.15}$$

Equation 2.15 allows one to compute discrete frequency samples of the truncated Fourier transform. A direct evaluation of the DFT formula requires large computer processing time since it necessitates approximately N^2 complex multiplications and additions. The introduction of the FFT algorithm reduces the computational requirements to $Nlog_2N$ complex multiplications and additions. The FFT is thus an efficient algorithm that greatly reduces both the number of operations needed to calculate the

DFT and the computer processing time [31]. The FFT algorithm development has made the application of a signal processing methodology for finite data analysis and problems solutions feasible. Various software packages and FFT analyzers exist already that make possible the calculation of the FFT in real time.

2.3.5 Power spectrum

Power Spectral Density is often used for investigating signal characteristics when phase information is not required. The power spectrum, $P(f)$ of $s(t)$ is defined as

$$P(f) = E[S(f)S^*(f)] \tag{2.16}$$

$$P(f) = |S(f)|^2 \exp^{(\theta(f)-\theta(f))} = |S(f)^2| \tag{2.17}$$

where E is the mean square value of the the complex conjugate denoted by *. It is clear from equation 2.17 that phase information is suppressed. Thus, the power spectrum shows the power in the signal as the mean squared amplitude at each frequency value but it does not detect the phase relationship between different frequency components as compared with the FFT. The PSD allows the investigation of the dominant frequencies in a signal, as it is the dominant frequencies that are likely to be important for our analysis.

In summary, the FFT and the PSD are powerful tools for analyzing and measuring signals. The PSD specifically is the most commonly applied signal processing technique to convert sampled time signals to the frequency domain. LabVIEW is used in the present research to carry out the FFT analysis and PSD calculations.

2.3.6 Sampling and windowing

There are many delicate issues that must be addressed in order to achieve a successful signal processing application. They are related to the selection of the sampling rate as it associates to the frequency content of the analog signal being sampled and the selection of a proper window to prevent spectral leakage. As an example, a continuous-time sinusoidal signal is expressed as

$$x_a(t) = A\sin(\omega_a t + \theta) \tag{2.18}$$

where ω_a is the analog frequency in radians per second. By uniformly sampling this signal at the sampling rate $f_s = 1/T$ hertz or samples/second, the discrete-time sinusoidal signal arises as

$$x(nT) = A\sin(\omega_a nT + \theta) \tag{2.19}$$

where the sampling instants are spaced uniformly by $\omega_a nT$.

Hence, the process of sampling an analog sinusoidal signal has produced a digital sinusoid. The analog and digital frequencies are related according to

$$\omega_a \ \ rad/sec\ (analog) \ \ -->\ \ \omega = \omega_a T \ \ rad/sample \quad (digital)$$

It is well known that the only case in which information is not lost through the process of sampling occurs when the continuous-time signal is bandlimited. The sampling theorem states that for a bandlimited continuous-time signal with maximum frequency f_{max}, the equally spaced sampling frequency f_s must be at least twice the maximum frequency component f_{max}, i.e., $f_s > 2 * f_{max}$ in order to be able to reconstruct the signal. If this criterion is violated, a phenomenon known as aliasing occurs. That is, frequency components above half the sampling frequency appear as frequency components below half the sampling frequency, resulting in an erroneous representation of the signal. The frequency $2 * f_{max}$ is called the Nyquist sampling rate. Half of this value, f_{max}, is also called the Nyquist frequency.

The use of windows is critical for a proper signal acquisition measurement. A window is a time-domain weighting function applied to the input signal. Windows are commonly utilized to force the amplitude of the sampled signal to be zero at both ends of the time record signal. The selection of a proper window can prevent spectral leakage which is a smearing of energy across the frequency spectrum caused by the transformation of signals that are not periodic or have a non integral number of cycles within the time record [1]. Therefore, if the i^{th} segment of data is multiplied by a proper data window $\omega(n)$, the windowing data is expressed as

$$\omega s_i(n) = \omega(n) s_i(n) \tag{2.20}$$

The application of a suitable data window such as Hanning, Hamming, Flat-top, etc., to the time sample segments improves the subsequent frequency spectrum and minimize the effects of spectral leakage when performing the FFT or PSD over a signal of non-integral number of cycles. The Hanning window is used in the present work.

Chapter 3

Mechanical Irregularities in Induction Motors

Condition monitoring schemes have mainly concentrated on detecting specific failure modes in three induction motor components: the stator, rotor and bearings. Together, these account for approximately 80% of all failures in the induction motor [12, 22]. Within these physical classes, there are a number of different fault categories. This thesis focuses on bearing related faults that correspond to mechanical irregularities in the motor. Abnormal mechanical conditions that can be present in the motor will now be described.

3.1 Rolling Element Bearing Faults

Induction motors can be purchased with two basic types of bearings: antifriction or rolling element bearings and sleeve bearings [32]. Rolling bearings use balls or other rolling elements, located between the bearing rings, to minimize friction. The rolling elements are separated and held in position by the cage or other retaining devices. Depending on the shape of their rolling elements, bearings fall into two main classes: ball bearings and roller bearings. Bearings are further classified by the specific shape of their rolling elements as ball, cylindrical, spherical, tapered. Bearings are also classified by function such as radial, thrust or both, depending on the direction of the applied load [33]. Sleeve bearings operate under the principal of hydrodynamic

lubrication. In this type of bearing, the relative motion between the rotation shaft and stationary bearing bore will generate a film of lubricant (lubricant wedge) between the rotating and stationary elements of the bearing. No rolling element is required. Sleeve bearing are only used in direct-connect applications [32].

The rolling element ball bearing is one of the most critical component in rotating electrical machinery [1]. Over 40% of the electrical machines failures arise from faulty bearings [34]. Bearings along with modern greases have been developed to extend the life expectancy and reduce the incidence of failure. However, despite being a very reliable mechanical piece, failure can occur due to a number of causes, including:

1. External factors such as abnormal loads and speed
2. Low maintenance management
3. Electromagnetic-induced faults such as shorted stator winding turns, asymmetries of magnetic field, broken rotor bars and/or end rings and unbalanced voltage supply conditions [35],
4. High-frequency bearing current effects which are caused by fast-switching inverters and induced shaft voltages produced by stator/rotor magnetic asymmetries in variable speed applications. Induced currents flow axially along the rotor, through the motor bearing and back through the other bearing, generating a voltage differential across the shaft [36].
5. Wrong operation, manufacturing defects or insufficient lubrication.
6. Radial and axial stresses due to improper installation problems when bearings are rudely forced onto the shaft or into the motor bearing housing.
7. Standstill of the motor: shaft and bearing may suffer some kind of deformation if the motor is not in service or stationary for a long period of time.

Any damaged bearing may produce bearing vibrations that in turn generate noise and cause the entire motor system to function incorrectly, leading to unexpected downtime and production losses. Some of the most significant effects caused by a faulted bearing are misalignment and airgap eccentricity.

3.1.1 Bearing schematic

Low voltage induction motors have two bearings that support and allow low-friction motion of the rotating shaft. Ball or roller bearings are the most common types of bearings used for low voltage induction motors in comparison with sleeve bearings. Rolling ball bearings usually consist of four parts: two concentric rings called the inner raceway and the outer raceway, a set of rolling elements or balls that rotates in the ring tracks and the cage or separator. Lubricant or grease inside the bearing is used to reduce friction and dissipate heat generated within. A set of seals at the side are often used to protect the bearing from contaminants such as dust and moisture. A schematic view of a rolling element bearing is depicted in figure 3.1.1.

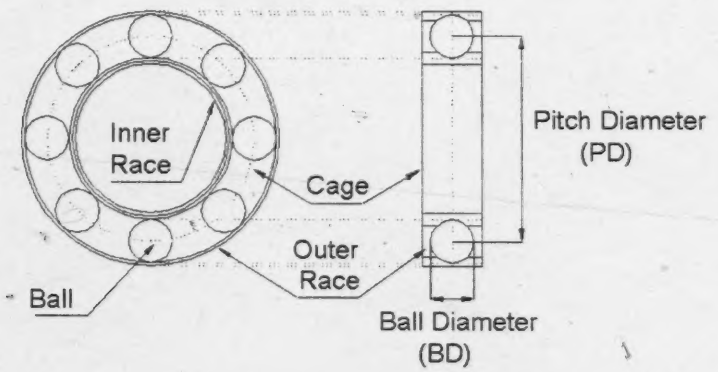

Figure 3.1: Bearing schematic

The bearing's rolling elements run in curvilinear grooves in the rings in order to increase the contact area and permit larger loads to be carried. The separator keeps the balls evenly spaced and prevents them from touching each other on the sides where their relative velocities are the greatest [37].

3.1.2 Characteristic bearing frequencies

Defective rolling element bearings generate mechanical vibrations with characteristic frequencies that are related to the raceways and the number of balls. These frequencies can be calculated from the bearing dimensions and the rotational speed of

the machine. The most prominent of these characteristic bearing frequencies are the outer race element pass frequency, inner race element pass frequency, the ball spin frequency and the fundamental train or cage frequency. These are described in [34] and presented below.

An outer race defect causes impulse when a ball or roller passes the defected area of race. The theoretical frequency is given by

$$f_o = \frac{n}{2} f_r (1 - \frac{BD}{PD} \cos\beta) \tag{3.1}$$

$$f_r = \frac{RPM}{60} \tag{3.2}$$

where n is the number of balls or rollers, f_r is the rotor rotational speed in hertz, BD is the diameter of the ball, PD is the pitch diameter and β is the contact angle of the rolling element as seen in figure 3.1.2.

The ball pass frequency of defect on the inner race is given by

$$f_i = \frac{n}{2} f_r (1 + \frac{BD}{PD} \cos\beta) \tag{3.3}$$

The ball spin frequency is given by

$$f_{sp} = \frac{PD}{2BD} f_r (1 - \left(\frac{BD}{PD}\right)^2 \cos^2\beta) \tag{3.4}$$

and the cage frequency is given by

$$f_c = \frac{1}{2} f_r (1 - \frac{BD}{PD} \cos\beta) \tag{3.5}$$

The relationship of the bearing vibration to the stator current spectra can be determined by considering that any bearing defect will create a radial motion between the rotor and stator of the machine, introducing eccentricity variations and consequent distortion of the airgap flux density. Therefore, these variations generate stator currents at frequencies given by [28, 38]

$$f_{bng} = (f_e \pm m f_{o,i,t}) \tag{3.6}$$

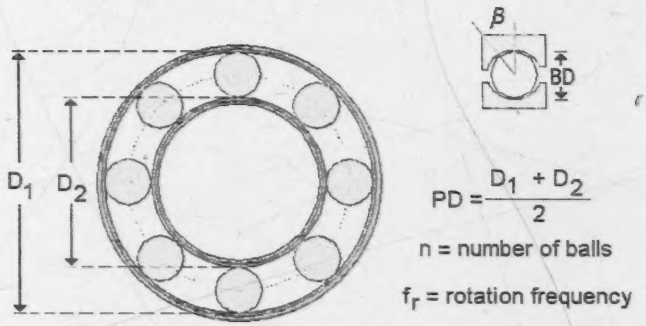

Figure 3.2: Bearing geometry

where $m = 1, 2, 3, \ldots$ and $f_{i,o,t}$ is one of the characteristic vibration frequencies given by equations 3.1, 3.3 and 3.5. As it is seen, the value of the characteristic bearing frequencies depend on the race defect and geometry of the bearing. However, these frequencies can be estimated for most bearings with between six and twelve balls by [38]

$$\begin{cases} f_o = 0.4\, f_r\, n \\ f_i = 0.6\, f_r\, n \\ f_t = 0.4\, f_r \end{cases} \tag{3.7}$$

3.1.3 Misalignment

One of the bearing's most common installation faults is misalignment [23]. Improper installation of the bearing is often caused by forcing the bearing into the shaft or in the housings. As a consequence, severe damage to the raceways can occur which leads to early failure. Common causes of misalignment of the bearing are the motor-load coupling being out of line, shaft deflection and tilted raceways. Figure 3.3 shows four different ways in which misalignment could occur [34].

3.2 Airgap Eccentricity

Rolling element bearings are designed to support the motor rotor. A bearing defect might produce a radial or axial motion between the rotor and the stator. If a cavity

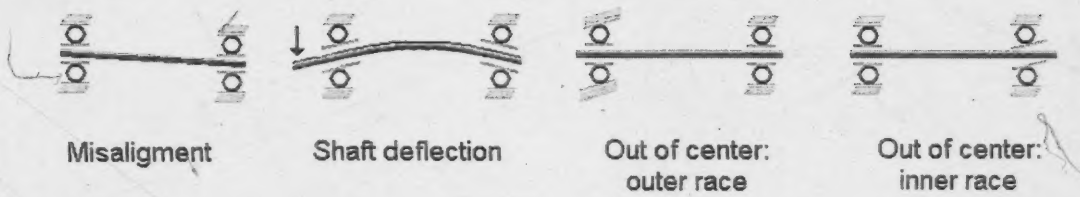

Figure 3.3: Misalignment of the bearing [2]

is found in the outer or inner race, the balls passing through it will fall in and move radially. Thus, the airgap geometry will be slightly disturbed, affecting the airgap permeance function [28].Therefore, any mechanical displacement resulting from damaged bearings causes the motor's airgap to vary in a manner that can be described by a combination of rotating eccentricities between the stator and the rotor [2]. The greatest resistance to the magnetic attraction between the stator and the rotor is the airgap between them. It is important that the clearance be uniform and as small as possible since it effects the amount of induced current in the rotor. When the airgap is not uniform, an eccentric condition appears between them. Although bearing problems may frequently be the cause of airgap eccentricities, rotor design, manufacturing tolerances and operating conditions may create airgap variations that cannot be attributed to bearing failures. Therefore, care should be taken when an eccentricity cause is diagnosed.

There are two types of airgap eccentricity: static and dynamic. In the case of static eccentricity, the airgap is fixed in space and is not a function of the rotor position. The rotor rotates about its center of mass but the center of rotation is not aligned with the centre of the stator. The rotor is turning on its own axis and a uniform airgap pattern is maintained throughout the rotation. Static eccentricity may be caused by the ovality of the stator core, by incorrect positioning of the rotor with respects to the stator or bearing misalignment. A representation of static eccentricity can be seen in figure 3.4.

Dynamic eccentricity is a function of space and time as the rotor rotates. The center of the mass is not the center of rotation and the position of minimum airgap

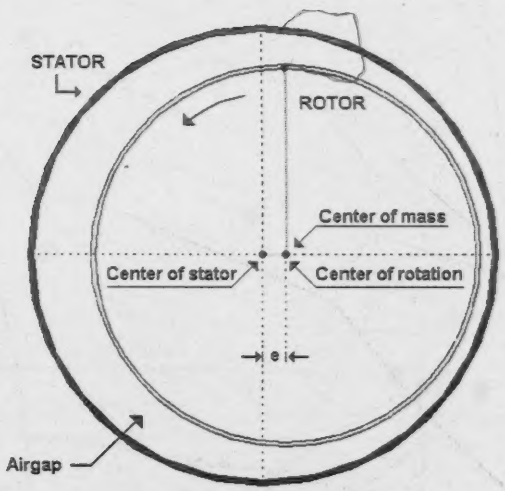

Figure 3.4: Static eccentricity

rotates with the rotor. The rotor rotation center and the geometric center of the stator are the same. Dynamic eccentricity may be caused by a thermally bowed or bent rotor shaft, rotor manufacturing defects, rotor unbalance, bearing wear and/or mechanical resonance [9]. A representation of dynamic eccentricity can be seen in figure 3.5.

In commercially produced three-phase induction motors both static and dynamic eccentricity exist simultaneously producing mixed eccentricity as seen in figure 3.6. The center of rotation, the center of mass and the center of the stator are located in different coordinates causing a major problem. Mixed eccentricity is mainly due to assembly procedures and manufacturing tolerances between the center of the stator core and the bearing centers. Figures 3.4, 3.5, and 3.6 depict exaggerated eccentricity conditions for understanding purposes. In a real machine, airgap variations are relatively small.

Detecting an increase in airgap eccentricity might allow a motor operator to avoid high vibration levels at the bearings and consequent damage. As a general rule, the airgap variation should be less than 10% of the total radial airgap [24, 14]. Thus, when eccentricity becomes large, the resulting unbalanced radial forces acting upon the rotor, known as unbalanced magnetic pull might cause a subsequent rotor rub

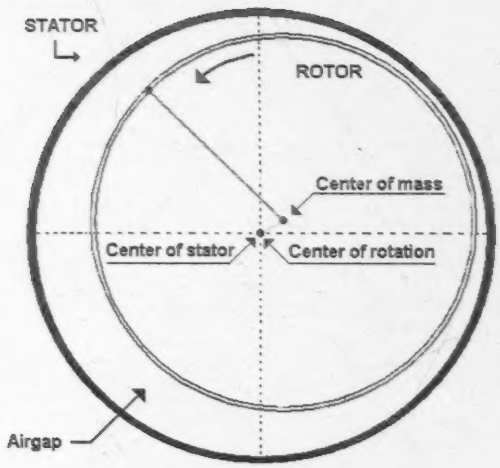

Figure 3.5: Dynamic eccentricity

against the stator due to the force acting at the point of minimun airgap. Hence, a severe break down of the stator core, rotor cage and windings may be produced. This can result in motor failure and expensive repair [9]. Therefore, the on-line diagnosis of rotor eccentricity is highly desirable to prevent serious operational problems.

In summary, bearing related faults along with motor manufacturing defects and operational stresses represent around 40% of all reported problems in the induction motor. Specifically, this failures can be classified as mechanical faults in this machine. Worn bearings due to fatigue, improper installation or ball and race defects along with a bent rotor shaft, rotor unbalance or stator core deformation can be the cause of static, dynamic or mixed eccentricity conditions in the machine. It is important to recognize undesirable percents of eccentricity conditions in the machine in order to avoid any severe damage of the stator core, windings or rotor cage. An unexpected breakdown of the motor may cause expensive repair, upset downtime of a process and heavy financial losses.

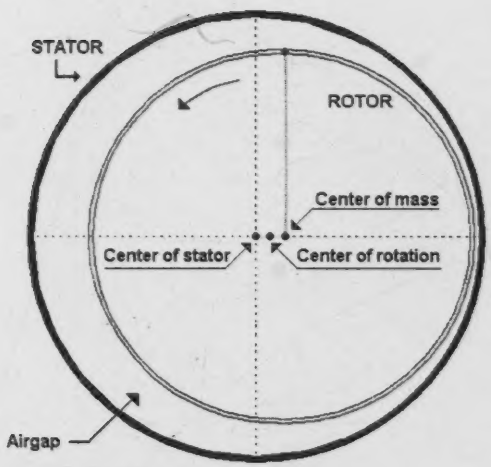

Figure 3.6: Static and dynamic eccentricity

Chapter 4

Motor Theoretical Anaylsis

An overview of the induction motor structure is presented in this chapter. The spatial magnetic field distribution in the machine's airgap and the effects of stator and rotor slotting, skewing of rotor bars and eccentricty conditions are included in the analysis. This provides background knowledge that allows the evaluation of the flux density distribution in the machine's airgap to identify frequency components in the current spectrum that relate to a mechanical asymmetry in the machine.

4.1 The Induction Motor Structure

A three phase induction motor consists of two basic components: the stator and the rotor. This machine is analogous to an ac transformer with a rotating secondary. The stator structure consists of a balanced three-phase winding spaced 120 electrical degrees apart and the core is composed of steel laminations around forming slots where copper wire coils are wound. The rotor or rotating secondary can be of two types: a conventional three-phase winding made of insulated wire, and a squirrel-cage winding. The type of winding gives rise to two main classes of motors: wound-rotor induction motors or a squirrel-cage induction motors. This thesis concentrates on squirrel-cage induction motors.

A squirrel-cage rotor is composed of laminations assembled over a steel shaft which is supported by a pair of bearings. Around the laminations' periphery, the rotor bars are housed. The rotor bars may consist of cast-aluminum or solid copper conductors

shorted at each end by conducting end rings. The arrangement of the rotor bars makes this structure look like a "squirrel cage" which is why this machine is known as the squirrel-cage induction motor. Figure 4.1 depicts the main components of this machine.

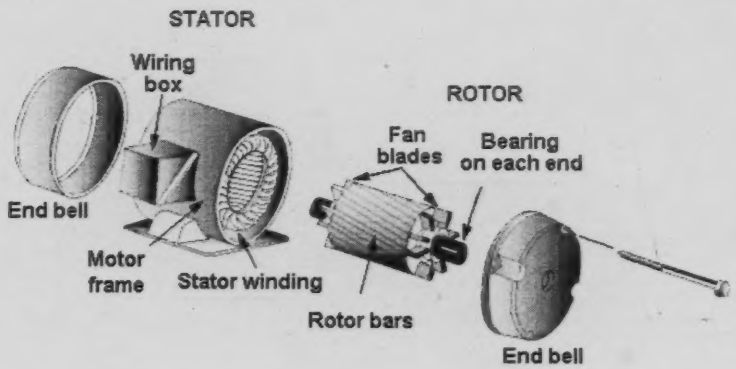

Figure 4.1: Induction motor components

The three phase squirrel-cage induction motor is the most common motor used in industry since it does not require a commutator, brushes or slip rings and has the fewest windings, least insulation in the wires and lowest cost per horsepower when compared to other machines such as ac synchronous motors [26].

In general, the main parts of any squirrel cage Induction Motor are

- The stator slotted magnetic core
- The stator electric winding
- The rotor slotted magnetic core composed of conducting bars and end rings
- The rotor shaft and bearings
- The cooling system
- The electric terminal box

When a balanced set of three-phase sinusoidal voltages are applied to the stator, current is drawn by the motor windings. This establishes a magnetic flux in the

airgap between the stator and the rotor that in turn produces a magnetic field that rotates at a synchronous speed. The flux paths are completed through the stator and rotor iron. Due to this magnetic field, an electro-motive force (EMF) is induced in the rotor producing a set of currents in the rotor bars. Magnetic field poles are thus created on both the stator and the rotor, centered on their respective axis. Motor torque is developed from the interaction of the rotor magnetic field and the stator's rotating magnetic field since both magnetic fields tend to line up their magnetic axes.

4.2 Magnetic Flux Density

When current flows in a coil of N turns, a magnetic field is created around the coil. The production of a magnetic field by a current i follows the definition of Ampere's Law

$$\oint H\delta l = Ni \tag{4.1}$$

The integral of the magnetic field intensity, H, over any closed path around a current-carrying conductor is equal to the value of the total current (Ni) enclosed by the path. The magnetic field created around the airgap of an electric motor is produced by the effective total current Ni, where i is the current and N is the number of turns in a winding per phase. This quantity is referred to as F, the magneto-motive force MMF of an N-turn current-carrying coil. The MMF is derived from 4.1 and is defined as:

$$MMF = Ni = F = H\delta \tag{4.2}$$

where H is the magnetic field intensity and δ is the effective airgap. The magnetic flux density is then related to the magnetic field intensity through a material constant called permeability (μ).

$$B = \mu H \tag{4.3}$$

4.3 Slot Geometry

A slot tooth is the lamination radial sector between two neighboring slots where the coils are embraced. The stator slot geometry depends on the induction motor power level. With low voltage random wound induction motors, round wire coils of multiple turns are inserted into the stator slots, allowing small slot openings. The rotor cage slot geometry depends on the starting torque level of the machine. Rounded semi-closed slots and rounded trapezoidal slots with rectangular teeth are typical rotor slots for medium starting torque in small power induction motors [4]. Figure 4.2 illustrates the airgap and common stator and rotor slot openings for medium size induction motors.

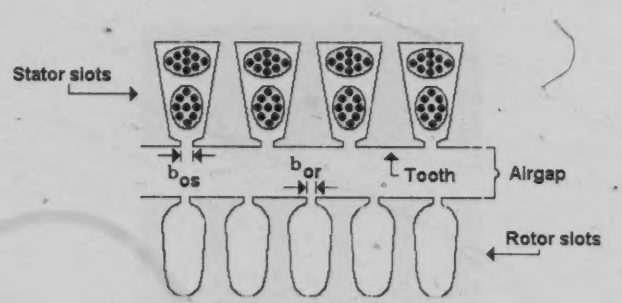

Figure 4.2: Airgap and slot openings

The limit of the airgap δ clearance is determined by mechanical constraints and by the ratio of the stator and slot openings b_{os}, b_{or} respectively. By having a smaller airgap (nonmagnetic crossing), the magnetization MMF, core surface losses and tooth flux pulsations are all reduced.

4.4 Windings

The stator winding coils are placed in the slots either as a single layer or double layer configuration in order to approximate a sinusoidal spatial distribution of the MMF. These configurations will reduce the magnetization current and improve the mechanical rigidity and heat transmission on the stator core, while the winding manufacturing

and placement in slots becomes easier. A machine will be composed of N_s number of slots in the stator and m number of phases. The number of slots per pole per phase q of the machine, is obtained as:

$$q = \frac{N_s}{2pm} \tag{4.4}$$

where p is called the number of pole pairs and it is referred as the number of MMF electrical periods per one revolution around the machine's airgap.

$$p = \frac{\pi D}{2\tau} \tag{4.5}$$

The coil pitch τ is the spatial half-period of the MMF wave, D is the stator bore diameter and $2p = 2, 4, 6, \ldots$. The pole pitch τ_p is the angular distance between two adjacent poles on a machine. The pole pitch in mechanical degrees is:

$$\tau_{pm} = \frac{180}{p} \tag{4.6}$$

It should be observed that regardless of the number of pole pairs on the machine, a pole pitch is always 180 electrical degrees. The electrical angle α_e is p times larger than the mechanical angle p_m. If the coil pitch is the same as the pole pitch, the stator coils are called full-pitch coils. That is, q is an integer value and a complete (pole to pole) symmetry for the winding is obtained. If the coil pitch is less than the pole pitch (≤ 1) the stator coils are called as fractional or chorded-pitch.

A single layer winding construction will always have full-pitch coils and the windings associated with each phase are distributed among several adjacent pairs of slots. A double layer winding consists of identical coils that are placed in the slots either as full-pitch coils or chorded coils. The use of double layer winding with chorded coils is extensive in induction machines since the harmonic content of the MMF may be reduced as well as the copper losses. Also, they are usually easier to manufacture and have simpler end-connections than single-layer winding. Therefore, they are less expensive to build. The motor in this study has a single layer concentric winding.

4.5 MMF Calculation

The concept and calculation of the magnetic field produced by a single coil of N conductors is easier to understand if one considers a coil of 1 conductor placed in a flat air gap δ between the stator and rotor supplied by a no-time variant current i as depicted in figure 4.3.

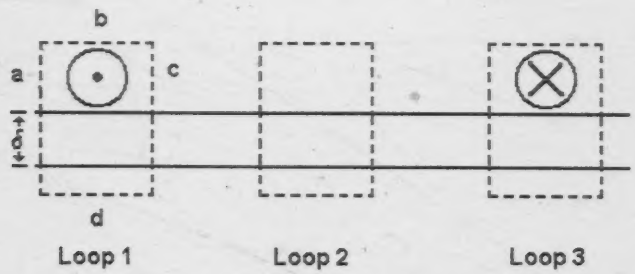

Figure 4.3: Air gap magnetic field of a coil placed in a flat air gap

By applying Ampere's law to each one of the loops shown, we can obtain the magnetic field along the coil pitch. Loop 1 is represented by equation 4.7

$$Loop\ \ 1 : H_{a1}\delta + H_{b1}\delta + H_{c1}\delta + H_{d1}\delta = Ni \tag{4.7}$$

If it is assumed that the iron is infinitely permeable, then:

$$B = \mu H \quad H = \frac{B}{\infty} \mapsto H = 0\ for\ \ H_{b1}\ \ \&\ \ H_{d1} \tag{4.8}$$

Hence,

$$H_{a1}\delta + H_{c1}\delta = Ni \quad H = \frac{Ni}{2\delta} \tag{4.9}$$

$$MMF = H\delta = \frac{Ni}{2} \tag{4.10}$$

Loop 2 is represented by equation 4.11

$$Loop\ \ 2 : H_{a2}\delta + H_{c2}\delta = 0 \quad H_{a2}\delta = -H_{c2}\delta \ \ H = constant \tag{4.11}$$

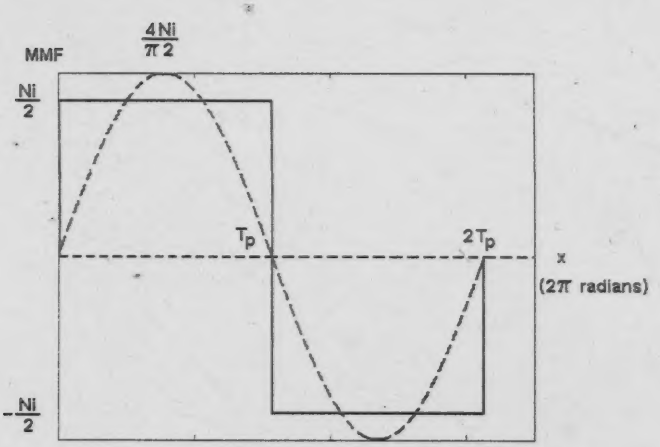

Figure 4.4: Magnetic field intensity variation of a single coil placed along the air gap

Thus, the variation of the MMF along the airgap is represented as in figure 4.4.

It can be seen that a rectangular airgap field spatial distribution is created along the length of the stator bore. The MMF of this arrangement will have a period of $2\tau_p$. Therefore, the magnetic field intensity H is a function of an angular distance x along the bore of the machine and hence H can be resolved into harmonic series by Fourier analysis.

The Fourier coefficients according to equations 2.13 and 2.14 for the rectangular distribution of figure 4.4 are obtained as:

$$\begin{aligned} A_n &= \frac{1}{\tau_p}\int_0^{2\tau_p} \frac{Ni}{2}\cos\frac{n\pi x}{\tau_p}dx \\ &= 0 \end{aligned} \tag{4.12}$$

$$\begin{aligned} B_n &= \frac{1}{\tau_p}\int_0^{\tau_p} \frac{Ni}{2}\sin\frac{n\pi x}{\tau_p}dx + \frac{1}{\tau_p}\int_{\tau_p}^{2\tau_p} \frac{Ni}{2}\sin\frac{n\pi x}{\tau_p}dx \\ &= -\frac{Ni}{2}\cos\frac{n\pi x}{\tau_p}\Big|_0^{\tau_p} + \frac{Ni}{2}\cos\frac{n\pi x}{\tau_p}\Big|_0^{2\tau_p} \\ &= \frac{2Ni}{n\pi} \end{aligned} \tag{4.13}$$

Therefore, the resulting Fourier series which approximates the rectangular MMF distribution is:

$$f(x) = \frac{2}{\pi}WI\left\{\sin\frac{\pi x}{\tau_p} + \frac{1}{3}\sin\frac{3\pi x}{\tau_p} + \frac{1}{5}\sin\frac{5\pi x}{\tau_p} + \ldots\right\} \tag{4.14}$$

where, W = number of turns per phase, I = phase current, τ_p = pole pitch. Due to the symmetry of the function, only odd harmonics are present in the function.

It is shown in figure 4.4 that the amplitude of the fundamental spatial harmonic is $4/\pi$ times greater than the maximum value of the MMF rectangular distribution. The period of the n^{th} spatial harmonic is n times shorter than the period of the fundamental. Therefore, a motor with p pole pairs, the n^{th} spatial harmonic will have np poles pairs instead of p pole pairs.

Now, considering a $m = 3$ phase winding, the corresponding MMF spatial distribution for each phase will take the form

$$f_{A,B,C}(x) = \frac{2}{\pi} W I_{A,B,C} \sum_{k=0}^{\infty} \frac{1}{2k+1} \sin\left((2k+1)(\frac{\pi x}{\tau_p} + \gamma_{A,B,C})\right) \tag{4.15}$$

where $\gamma_{A,B,C}$ is the spatial distribution of the winding around the machine bore. Usually it is considered an angular displacement of $2\pi/m$ between each phase: $\gamma_A = 0$, $\gamma_B = 2\pi/3$, $\gamma_C = 4\pi/3$. Ideally, a sinusoidal airgap MMF spatial distribution should be produced by the windings of each of the stator phases. However, due to the placement of the windings in slots the sinusoidal distribution of MMFs along the periphery of the machine is diminished, giving rise to the already mentioned space harmonics.

4.5.1 The rotating magnetic field

The operation of the induction motor is attributed to the MMF produced by the stator windings when 3 phase electrical power is applied, giving rise to a rotating magnetic field. To understand the principle of generating a rotating magnetic field, a basic primitive 3 phase machine with a single layer winding is considered and illustrated as in figure 4.5 a).

This figure depicts three diametrically wound N-turn coils $(a - a', b - b', c - c')$ displaced by $2\pi/m$ radians from each other with each coil having a pitch of half the periphery of the stator. In this case, the stator contains three windings (one for each phase) embedded in slots cut lengthwise on the inside of the stator. At any instant of time, each phase winding produces a MMF in the airgap in the form of equation 4.14 which can be represented by a space vector along the magnetic axis of that phase.

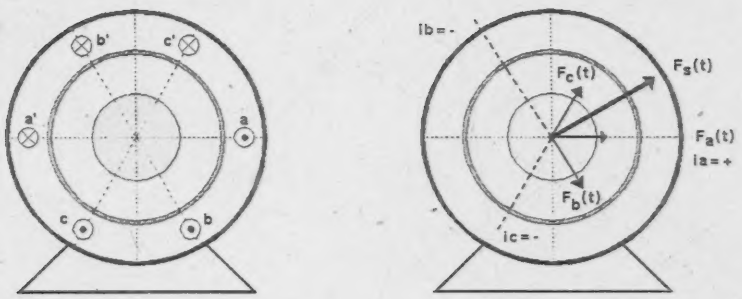

Figure 4.5: Single layer 3 phase primitive machine and resultant MMF

If one considers only the fundamental space vector component of equation 4.14, the MMF space vectors for each phase are $Fa(t)$, $Fb(t)$ and $Fc(t)$ as shown in figure 4.5 b). Assuming no magnetic saturation in the iron core, the resultant MMF distribution in the airgap due to all three phases at one instant of time can be represented using vector addition. The resultant space vector $Fs(t)$ is also shown in figure 4.5 b).

If the machine is supplied with a set of time-variant currents of the general form

$$I_{A,B,C}(t) = \sum_{n=1}^{\infty} I_{n,A,B,C} \sin\left(n(\omega t + \theta_{A,B,C})\right) \tag{4.16}$$

where $\theta_{A,B,C}$ is the angular displacement between phases: $0, \frac{2\pi}{3}, \frac{4\pi}{3}$, then the total MMF obtained by superposition will be

$$F(x) = F_A(x,t) + F_B(x,t) + F_C(x,t) \tag{4.17}$$

$$\begin{aligned} f(x,t) = \frac{2}{\pi} W \sum_{n=1}^{\infty} \sum_{k=0}^{\infty} \frac{I_{An}}{v} \sin(n\omega t) \sin(v(\frac{\pi x}{\tau_p} + \gamma_A) + \\ + \frac{I_{Bn}}{v} \sin(n(\omega t + \theta_B)) \sin(v(\frac{\pi x}{\tau_p} + \gamma_B) + \\ + \frac{I_{Cn}}{v} \sin(n(\omega t + \theta_C)) \sin(v(\frac{\pi x}{\tau_p} + \gamma_C)) \end{aligned} \tag{4.18}$$

where $v = (2k+1)$ since only odd spatial harmonics are considered. By applying the following trigonometric identity

$$\sin A \sin B = \frac{1}{2}[\cos(A-B) - \cos(A+B)] \tag{4.19}$$

the MMF takes the form

$$\begin{aligned} f(x,t) = \frac{W}{\pi} \sum_{n=1}^{\infty} \sum_{k=0}^{\infty} \frac{I_{An}}{v} [\cos(n\omega t - v\beta - v\gamma_A) - \cos(n\omega t + v\beta + v\gamma_A)] + \\ + \frac{I_{Bn}}{v} [\cos(n(\omega t + \theta_B) - v\beta - v\gamma_B) - \cos(n(\omega t + \theta_B) + v\beta + v\gamma_B)] + \\ + \frac{I_{Cn}}{v} [\cos(n(\omega t + \theta_C) - v\beta - v\gamma_C) - \cos(n(\omega t + \theta_C) + v\beta + v\gamma_C)] \end{aligned} \tag{4.20}$$

where $\beta = \frac{\pi x}{\tau_p}$. It is shown that the MMF distribution travels in both space and time. It can be seen that the n^{th} harmonic of the current produces an infinite number of spatial harmonics for each phase. The spatial distribution of the waveform will always contain $2(2k+1)$ poles at a particular instant of time. Also, the spatial electrical angle between the axes of adjacent poles in a symmetrical machine is equal to $\frac{2\pi}{m}$. The phase shift between the currents in adjacent phases is also $\frac{2\pi}{m}$. Therefore, the electrical angle between the spatial axes of the first and the i^{th} phase, as well as the phase shift between the current in the first and the i^{th} phases is equal to $\frac{2\pi(i-1)}{m}$.

The k^{th} spatial harmonic of the n^{th} current harmonic for the first phase can be defined as:

$$F_{1,n,k}(x,t) = \frac{W I_{1,n}}{v\pi} [\cos(n(\omega t + \theta_1) - v\beta - v\gamma_1) - \cos(n(\omega t + \theta_1) + v\beta + v\gamma_1)] \tag{4.21}$$

In the same manner, the k^{th} spatial harmonic of the n^{th} current harmonic for the i^{th} phase can be defined as:

$$F_{i,n,k}(x,t) = \frac{W I_{i,n}}{v\pi} [\cos(n(\omega t + \theta_i) - v\beta - v\gamma_1) - \cos(n(\omega t + \theta_i) + v\beta + v\gamma_i)] \tag{4.22}$$

and after rearrangement

$$\begin{aligned} F_{i,n,k}(x,t) = \hat{F} \Big[\cos(n(\omega t + (i-1)\frac{2\pi}{m}) - v(\beta + (i-1)\frac{2\pi}{m})) - \\ - \cos(n(\omega t + (i-1)\frac{2\pi}{m}) + v(\beta + (i-1)\frac{2\pi}{m})) \Big] \end{aligned} \tag{4.23}$$

$$F_{i,n,k}(x,t) = \hat{F}\left[\cos\left(n\omega t - v\beta - (i-1)\frac{(n-v)}{m}2\pi\right) - \right.$$
$$\left. - \cos\left(n\omega t + v\beta - (i-1)\frac{(n+v)}{m}2\pi\right)\right] \qquad (4.24)$$

where

$$\hat{F} = \frac{WI_{i,n}}{v\pi} \qquad i = 1,2,3,\ldots,m$$
$$v = (2k+1) = 1,3,5,\ldots \qquad \theta_i = \gamma_i = \tfrac{(i-1)}{m}2\pi$$
$$m = 1,2,3,\ldots \qquad \beta = \tfrac{\pi}{\tau_p}x$$

Considering the fundamental spatial and time harmonic, i.e. $k = n = 1$, the MMF created by the current in the i^{th} phase is:

$$F_{i,1,1}(x,t) = \hat{F}\left(\cos(\omega t - \frac{\pi}{\tau_p}x) - \cos(\omega t + \frac{\pi}{\tau_p}x - (i-1)\frac{4\pi}{m})\right) \qquad (4.25)$$

It can be seen that the MMF distribution contains a positive and a negative sequence component. Assuming that the currents in all phases are identical, the amplitudes of the MMF in the phases of a symmetrical machine will be equal. By adding the positive and negative sequence of all phases, the total MMF produce by all m phases is obtained. For the positive sequence

$$F_{pos}(x,t) = \sum_{i=1}^{m} \hat{F}\cos\left(\omega t - \frac{\pi}{\tau_p}x\right) = m\hat{F}\cos\left(\omega t - \frac{\pi}{\tau_p}x\right) \qquad (4.26)$$

The amplitude of the positive sequence is m times greater than the amplitude of the MMF created by one phase. For the negative sequence

$$F_{neg}(x,t) = \sum_{i=1}^{m} \hat{F}\cos\left(\omega t + \frac{\pi}{\tau_p}x - (i-1)\frac{4\pi}{m}\right)$$

$$F_{neg}(x,t) = \hat{F}\cos(\omega t + \beta) + \hat{F}\cos(\omega t + \beta - \frac{4\pi}{m} + \hat{F}\cos(\omega t + \beta - \frac{8\pi}{m}) = 0 \qquad (4.27)$$

Therefore, for a 3 phase machine if the positive or negative sequence component in all phases of the n^{th} time and k^{th} spatial harmonics are in phase, the resultant MMF

is 3 times greater than the amplitude of the n^{th} time and k^{th} spatial harmonic in each phase. Otherwise, the resultant MMF is zero. According to equation 4.24, in order to have the time and spatial harmonics in phase, the factors $\frac{(n-v)}{m}2\pi$ and $\frac{(n+v)}{m}2\pi$ for the positive and negative sequence respectively must be equal to an integer number.

For all other combinations of k, m and n, the negative sequence component of the MMF vanishes. Thus, for a given number of phases only certain combinations of the spatial and time harmonics generate either the positive, negative or both components of the MMF. This is illustrated in table 4.1 created for a 3 phase machine. It should be noted that the above analysis assumes equal magnitude current harmonics in each phase, i.e. a perfectly balanced machine. A real machine will not be perfectly balanced and there will be some difference between the magnitudes of harmonics from phase to phase, affecting the resultant MMF distribution.

Table 4.1: MMF spatial and time harmonics combinations

	v	space						
n		1	3	5	7	9	11	13
	1	$+1\omega_{1,1}$	0	$-5\omega_{1,1}$	$+7\omega_{1,1}$	0	$-11\omega_{1,1}$	$+13\omega_{1,1}$
t	3	0	$\pm1\omega_{1,1}$	0	0	$\pm3\omega_{1,1}$	0	0
i	5	$-\frac{1}{5}\omega_{1,1}$	0	$+1\omega_{1,1}$	$-\frac{7}{5}\omega_{1,1}$	0	$+\frac{11}{5}\omega_{1,1}$	$-\frac{13}{5}\omega_{1,1}$
m	7	$+\frac{1}{7}\omega_{1,1}$	0	$-\frac{5}{7}\omega_{1,1}$	$+1\omega_{1,1}$	0	$-\frac{11}{7}\omega_{1,1}$	$+\frac{13}{7}\omega_{1,1}$
e	9	0	$\pm\frac{1}{3}\omega_{1,1}$	0	0	$\pm1\omega_{1,1}$	0	0
	11	$-\frac{1}{11}\omega_{1,1}$	0	$+\frac{5}{11}\omega_{1,1}$	$-\frac{7}{11}\omega_{1,1}$	0	$+1\omega_{1,1}$	$-\frac{13}{11}\omega_{1,1}$
	13	$+\frac{1}{13}\omega_{1,1}$	0	$-\frac{5}{13}\omega_{1,1}$	$+\frac{7}{13}\omega_{1,1}$	0	$-\frac{11}{13}\omega_{1,1}$	$+1\omega_{1,1}$

In conclusion, the first terms of the MMF distribution when a symmetrical and balanced current is supplied to the machine (only fundamental current component considered $n = 1$) follow from the positive or negative sequence as shown in table 4.1

$$F(x,t) = \frac{3WI}{\pi}\left(cos(\omega t - \frac{\pi}{\tau_p}x) - \frac{1}{5}cos(\omega t + \frac{5\pi}{\tau_p}x) + \right.$$
$$\left. + \frac{1}{7}cos(\omega t - \frac{7\pi}{\tau_p}x) - \frac{1}{11}cos(\omega t + \frac{11\pi}{\tau_p}x) + \ldots\right) \qquad (4.28)$$

One term of equation 4.28 describes a MMF distribution which varies sinusoidally in both space and time. Due to full symmetry of the coils with q as an integer and the combination of the phase sequence, forward-revolving field frequencies at harmonics of v_f and backward-revolving fields at harmonics of v_b are present. That is $v = v_{f,b} = (1 \pm 6k)$ and $k = 0, 1, 2, 3, \ldots$. As seen, the MMF spatial distribution is not sinusoidal and the harmonic components of equation 4.28 may be recognized in the current spectrum. Each space harmonic interacts with the supply time-harmonics and the combination of both may be also identifiable in the stator current spectrum. Hence, it is important to recognize the harmonic components that describes the spatial MMF distribution around the airgap of the machine since each of them interacts with the permeance function of the airgap flux density. Similarly, equation 4.28 will be used in chapter 5 to calculate and simulate the stator MMF.

The rotational mechanical frequency of the positive sequence component of the fundamental time and spatial harmonic, $\omega_{1,1}$ follows from

$$\omega_{v,n} = +\frac{(1 \pm 6k)\omega}{np} \quad for \;\; v = 1 \;\&\; n = 1 \tag{4.29}$$

which is the synchronous rotating magnetic field of the motor. If the order of the time and spatial harmonic are equal, i.e., $k = n$, then the time and spatial harmonic of the same order will travel at speed $\omega_{1,1}$.

$$\omega_{k,k} = \omega_{n,n} = +\frac{\omega}{p} \tag{4.30}$$

4.6 Winding Factors

A primitive 3 phase machine represents poor utilization of the space available along the air gap of the machine. It is usual to spread out the winding along the periphery of the stator. Therefore, by distributing the turns of each phase into q adjacent slots, a phase band is created. A 3 phase machine will be composed of $C = m * p$ phase bands, where m is the number of phases and p the number of pole pairs. Each phase band will consist of q slots per phase per pole. The number of turns per coil is given by

$$W_c = \frac{W}{q} \tag{4.31}$$

where W is the total number of turns in a winding. Each slot of the phase band coil is separated by α_{el} radians. that is

$$\alpha_{el} = \frac{2\pi}{N_s} \quad N_s = Number\ \ of\ \ stator\ \ slots. \tag{4.32}$$

The MMF wave produced by a single coil of N turns is represented by equation 4.28. The k^{th} spatial MMF harmonic component of this series is of the form:

$$F_k(x,t) = \frac{3WI}{k\pi}\cos(\omega t + k\frac{\pi x}{\tau_p}) \tag{4.33}$$

This analysis is carried out considering a symmetrical machine where each phase is carrying a current with equal amplitude and frequency. Only the fundamental component ($n = 1$) of the current waveform is taken into account. Each coil in a phase band will produce a MMF wave similar to equation 4.33. By adding the MMF of each coil per phase band, separated by an angle α_{el}, one obtains:

$$F_k(x,t) = \frac{3WI}{qk\pi}\sum_{a=0}^{q-1}\cos(\omega t + k\frac{\pi x}{\tau_p} + ka\alpha_{el}) \tag{4.34}$$

This summation can be accomplished by making using of the following trigonometric identity:

$$\sum_{j=0}^{q-1}\cos(A + jB) = \cos(A + \frac{(q-1)}{2}B)\cdot\frac{\sin\frac{qB}{2}}{\sin\frac{B}{2}} \tag{4.35}$$

Then, the MMF distribution can be written as

$$F_k(x,t) = \frac{3WI}{k\pi}\cdot\frac{\sin\frac{qk\alpha_{el}}{2}}{q\sin\frac{\alpha_{el}}{2}}\cos(\omega t + k\frac{\pi x}{\tau_p} + \frac{(q-1)}{2}k\alpha_{el}) \tag{4.36}$$

It should be noted that the effect of distributing the winding along the periphery of the stator, modifies the MMF by a factor known as distribution factor or spread factor K_{dn}.

$$K_{dn} = \frac{\sin\frac{qkp\alpha_{el}}{2}}{q\sin k\frac{p\alpha_{el}}{2}} \tag{4.37}$$

In general, according to equation 4.37, for machines with p pole pairs and $N_{s,r}$ slots, the order of the harmonics of a distributed 3 phase winding which retain their effect to the same extent as the fundamental are defined by

$$2mkq \pm 1 = 6kq \pm 1 \tag{4.38}$$

where $k = 1, 2, 3, \ldots$. These particular harmonics are called the step harmonics of the stator magnetic field. It is observed that the step harmonics have a distribution factor equal to the fundamental distribution factor and the step harmonics may be recognized in the current spectrum.

As previously stated, a single layer winding is always full pitched. In the same manner, a double layer winding can be full pitched or short pitched.

The difference between a full pitched winding and a chord pitched winding is that they are displaced from each other by an angle θ between slots. The angle θ must be an integral multiple of the slot pitch angle α_{el}.

The pitch factor due to chording coils is defined as:

$$K_{pn} = \sin(\frac{np\pi y}{2\tau_p}) \tag{4.39}$$

Where y is the angular displacement of slots that the coil has been chorded. For a full pitched winding, $K_{pn} = 1$.

The product $K_{dn}K_{pn}$ is usually called the winding factor K_{wn}. The winding factor allows for the calculation of the relative magnitudes of the various MMF space harmonics produced by a short-pitched distributed three-phase winding.

4.7 The MMF of a 3-Phase Winding

A general expression for the MMF produced by a three phase winding is derived from equation 4.28 along with the integration of the winding factors. It should be noted that for a symmetrical three phase winding having equal phase bands, p pole pairs and an integral number of slots per pole per phase, q, the harmonic components that describes the MMF spatial distribution are obtained with:

$$v = p(6k \pm 1) \tag{4.40}$$

Therefore, the MMF for full pitch ($K_{pn} = 1$) or chorded-pitch winding ($K_{pn} \neq 1$) becomes:

$$F(x,t) = \frac{3WI}{\pi} \sum_{k=0}^{\infty} \frac{1}{p(6k \mp 1)} K_{dn} K_{pn} \cos(\omega t \pm p(6k \mp 1)\frac{\pi x}{\tau_p}) \tag{4.41}$$

Hence, at an arbitrary point along the airgap (corresponding to the angle α measured from a stationary reference frame in the stator), the magnetic field intensity distribution, according to equation 4.41, is sinusoidally changing in time. Similarly, at an instant of time t, the magnetic field intensity of each harmonic component has also a sinusoidal space distribution along the machine bore periphery.

Figure 4.6 depicts the traveling space wave along the airgap of a machine with 48 stator slots, $p = 2$ and $K_{pn} = 1$. Various instants of time are plotted according to equation 4.41 when a balanced 60 Hz sinusoidal current is supplied. The matlab program described in appendix A is used to depict such variations. Figure 4.7 shows the same traveling wave in both space and time.

It should be noted that the waveform is composed of 48 discrete steps that are distributed along the airgap of the machine due to the placement of the windings in slots. In the same manner, one can consider the physical arrangement of the windings in a 4 pole, 3-phase machine with 48 slots, 48 concentric coils and each phase with $q = 4$ coils per pole per phase. Each coil will create the rectangular spatial distribution of the MMF along the machine as seen in figure 4.3. By adding the MMF distribution of each phase, the total generated MMF waveform is illustrated in figure 4.8 corroborating the validation of equation 4.28.

4.8 Airgap Field Flux Density

As presented in section 4.2, equation 4.3 represents the magnetic flux density which is related to the magnetic field intensity through a material constant called permeability (μ). The magnetic permeability (μ) is defined as the product of the relative magnetic permeability μ_r and the magnetic permeability of free space μ_o

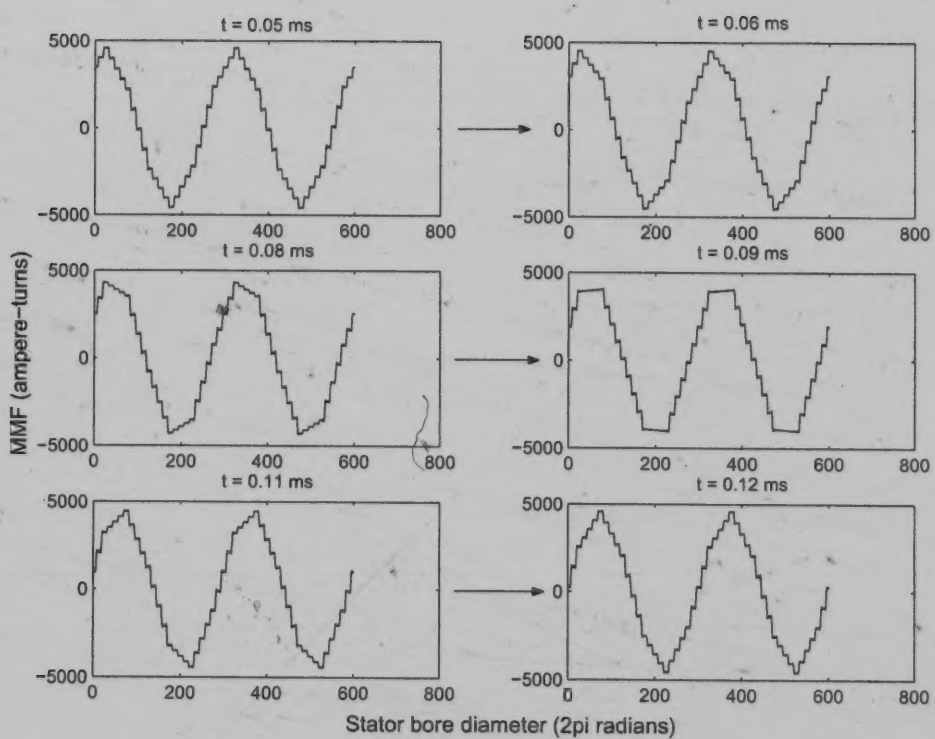

Figure 4.6: MMF space traveling wave along the airgap

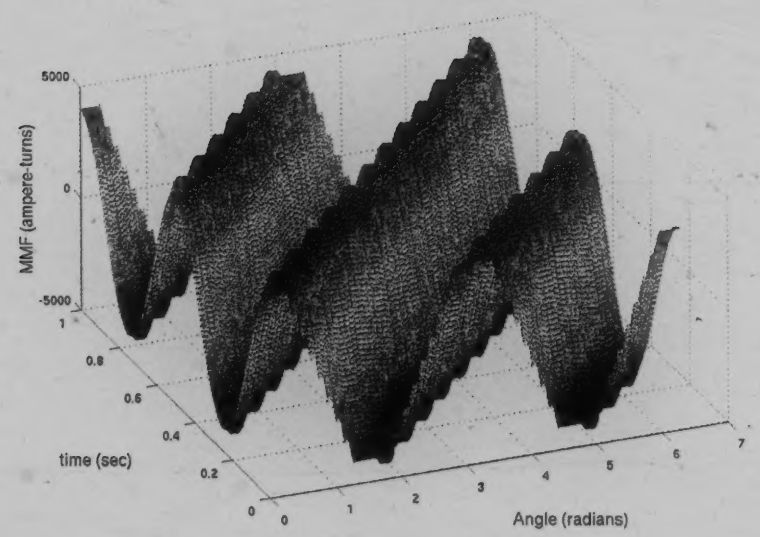

Figure 4.7: MMF traveling wave in space and time

$$\mu = \mu_r \mu_o \tag{4.42}$$

If the windings of the machine are carrying a sinusoidal m-phase current of amplitude $I\sqrt{2}$ and assuming infinite permeability ($\mu = \infty$) of iron, a magnetic field intensity will appear in the air gap. Assuming the relative permeability of air to be $\mu_r = 1$, the magnetic air gap field distribution will be:

$$B(\alpha) = \mu_o H(\alpha) \tag{4.43}$$

where $\mu_o = 4\pi \cdot 10^{-7}[Hm^{-1}]$ is the permeability of vacuum or free space in Henry per meter. Recalling that the distribution waveform of the magnetomotive force MMF is defined by the relation

$$F(\alpha) = \delta H \tag{4.44}$$

where δ = airgap and H = magnetic field intensity

Hence, the stator airgap field distribution is in the form of

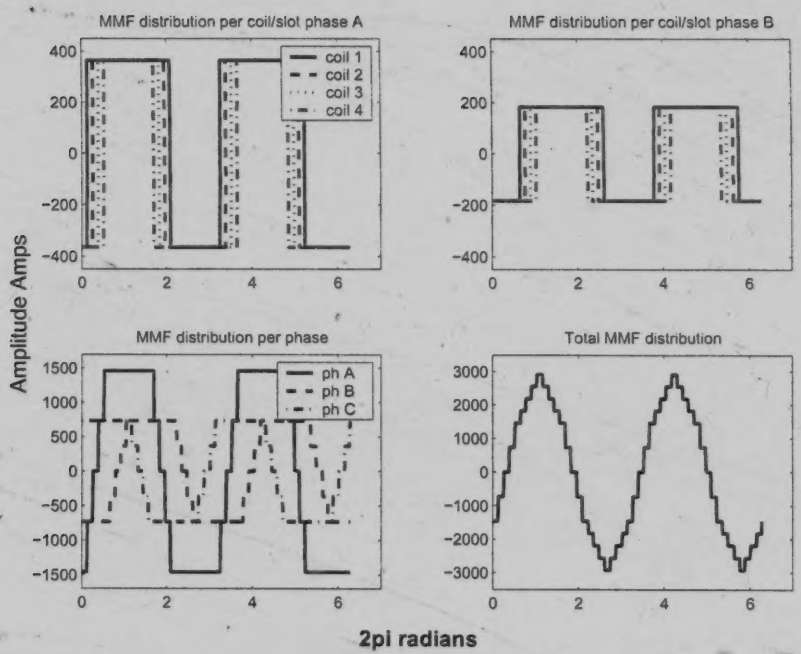

Figure 4.8: MMF space traveling wave along the airgap (physical arrangement)

$$B(\alpha) = \mu_o \frac{F(\alpha)}{\delta} = P(\alpha)F(\alpha) \quad and \quad P(\alpha) = \frac{\mu_o}{\delta} \tag{4.45}$$

where P is defined as the permeance function. It is also referred as the inverse airgap function for the distribution of the magnetic conductance, $\lambda_{s,r}$, of the flux density function.

Considering a traveling stator MMF from equation 4.33 with an open rotor winding, a constant airgap (slot opening effects are neglected) and infinite permeability in the stator and iron core, an ideal no load flux density will be produced in the airgap defined as

$$B_k(\alpha, t) = \frac{\mu \hat{F}(\alpha)}{\delta} \cos(\omega t + \frac{k\pi}{\tau_p} x) \tag{4.46}$$

This flux density will self-induce sinusoidal EMFs and currents in the stator windings. In turn, these harmonic components can be identified in the stator current spectrum.

Now, by considering the presence of slots along the air gap of the machine, the magnetic flux B will face a drop to a value B_{min} which is a function of the slot opening o as seen in figure 4.9. The air gap is much wider under the slot than under the teeth, hence large differences in the values of the flux around the periphery of the machine are to be expected. Figure 4.9 represents the flux density variation from a value B_{max} to a value B_{min} in accordance with the slot opening. An average value B_s is defined and the following relation is obtained [39]:

$$K_c = \frac{B_{max}}{B_s} = \frac{t_d}{t_d - 1.8\beta o} \tag{4.47}$$

The ratio between the maximum and the average flux density under one slot pitch is called the Carter factor, K_c. Thus, in equation 4.47, t_d is the slot pitch, o is the slot opening and β is a function of the ratio o/δ and the corresponding curve is found in [39].

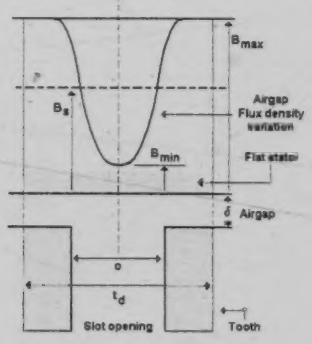

Figure 4.9: Variation of air gap flux density due to slotting in one side of the air gap.

The Carter factor defined in equation 4.47 describes the increase of the air gap if there are slots only in one side of the gap. If both stator and rotor have slots, the resultant Carter factor is equal to the product of the Carter factor for the stator slots and the Carter factor for the rotor slots.

$$K_{c12} = K_{c1} \cdot K_{c2} \tag{4.48}$$

Hence, if the effective air gap width around the periphery of the machine is known

and the presence of slots in the stator are considered through the use of the Carter Factor, the air gap flux distribution in equation 4.45 becomes

$$B(x,t) = \frac{3\mu W I\sqrt{2}}{\pi\delta K_c}\sum_{k=0}^{\infty}\frac{1}{p(6k\mp 1)}K_{wk}cos\left(\omega t \pm p(6k\mp 1)\frac{\pi}{\tau_p}x\right) \tag{4.49}$$

Equation 4.49 represent the traveling flux density distribution around airgap of the machine. The information related to slotting the stator and the rotor along with the effect of airgap eccentricity conditions can be included in this function when defining the permeance function. Hence, the flux density will induce current components of the same order in the stator windings that in turn can be identifiable in the current spectrum. By recognizing these components due to slotting and eccentricity in the machine, one can relate any mechanical fault in the motor to the current spectra. The permeance function includes the effects of slotting and airgap eccentricity. This is described as follows.

4.8.1 Airgap slot harmonics

The slot's openings introduce a continuous variation of the airgap $\delta(\alpha)$ and consequently to the permeance function. The permeance function, defined as the inverse of the air gap is:

$$f(\alpha) = \frac{1}{\delta(\alpha)} \tag{4.50}$$

Due to the slotting, the airgap difference for every slot around the machine $\Delta(\alpha)$ is [39]

$$\Delta(\alpha) = \frac{1}{f(\alpha)} - \delta \tag{4.51}$$

If both the stator and the rotor are slotted, the resultant air gap at the point α is given by the relation

$$\delta(\alpha) = \delta + \Delta_1(\alpha) + \Delta_2(\alpha - \alpha_r) = \frac{1}{f_1(\alpha)} + \frac{1}{f_2(\alpha - \alpha_r)} - \delta \tag{4.52}$$

where α_r is the angular displacement of the origin of the rotor slotting with respect to the origin of the stator slotting. The functions $f_1(\alpha)$ and $f_2(\alpha - \alpha_r)$ are periodic

functions with a period of one stator or rotor slot pitch. Both functions are defined as the stator and rotor slotting harmonics and can be broken down into harmonics as [39]:

$$f_1(\alpha) = a_0 - \sum_{v=1}^{\infty} a_v \cos vN_s\alpha \tag{4.53}$$

$$f_2(\alpha - \alpha_r) = b_0 - \sum_{v=1}^{\infty} b_v \cos vN_r(\alpha - \alpha_r) \tag{4.54}$$

$$a_0 = \frac{1}{K_{c1}\delta}, \quad b_0 = \frac{1}{K_{c2}\delta}, \quad a_v, b_v = \frac{\beta}{\delta} F_v\left(\frac{o_{s,r}}{t_{d(s,r)}}\right) \tag{4.55}$$

$$F_v(\frac{o_{s,r}}{t_{d(s,r)}}) = \frac{4}{v\pi}\left(0.5 + \frac{(\frac{vo_{s,r}}{t_{d(s,r)}})^2}{0.78 - 2(\frac{vo_{s,r}}{t_{d(s,r)}})^2}\right)\sin(1.6\frac{\pi v o_{s,r}}{t_{d(s,r)}}) \tag{4.56}$$

During operation, the rotor and stator slot MMF harmonics, given by the combination of the MMF and the permeance function, will interact with the fundamental component of the air gap flux density. Hence, the flux density carries out information related to the slotting harmonics that in turn are induced in the stator windings and they should be identifiable in the current spectrum.

For the induction motor used in this research, the slot opening parameters are given in table 4.2. Figure 4.10 depicts the calculated stator and rotor slots harmonic function $f_{1,2}(\alpha)$ for $v = 0, 1, 2, 3, 4, 5$ according to equations 4.53 and 4.54. The value of the coefficients a, b_v are listed in table 4.3.

Table 4.2: Stator and rotor slots parameters

Constant	*value*		
δ	0.92 mm		
β_s	0.23	β_r	0.048
o_s	2.735 mm	o_r	1 mm
t_{ds}	11.304 mm	t_{dr}	13.420 mm

Consequently, the permeance function (P) of the flux density takes the form

Table 4.3: Stator and rotor slots harmonic coefficients for $v = 0, 1, 2, \ldots, 14, 15$

$a_{(0,1,2,3,4,5)}$	990.181	175.605	129.695	73.400	28.064	2.327
$a_{(6,7,8,9,10)}$		-5.113	-2.829	0.692	1.583	0.448
$a_{(11,12,13,14,15)}$		-0.611	-0.578	0.051	0.387	0.185
$b_{(0,1,2,3,4,5)}$	1080.7	12.327	11.992	11.450	10.725	9.847
$b_{(6,7,8,9,10)}$		8.855	7.793	6.762	5.477	4.452
$b_{(11,12,13,14,15)}$		3.466	2.573	1.795	1.142	0.620

$$P = \frac{1}{\delta(\alpha, \alpha_r)} = \lambda_{s,r} \quad and \quad B = \mu \cdot MMF \cdot P \tag{4.57}$$

The airgap flux density is defined as the product of the airgap MMF and the airgap permeance. Anomalies in either the permeance or the MMF will produce sinusoidal variations in the airgap flux density.

Therefore, the expression for the magnetic conductance according to equation 4.52 due to the effect of the stator and rotor slotting can be approximated as [39]

$$\lambda_{s,r} = \frac{1}{\delta(\alpha, \alpha_r)} = \frac{1}{\frac{1}{f_1(\alpha)} + \frac{1}{f_2(\alpha)} - \delta} \approx \delta f_1(\alpha) f_2(\alpha - \alpha_r) \tag{4.58}$$

After substituting the first 2 terms of the fourier series of equations 4.53 and 4.54 we obtain the expression

$$\lambda_{s,r} = \delta(a_0 - \sum a_v \cos vN_s\alpha)(b_0 - \sum b_v \cos vN_r(\alpha - \alpha_r)$$

$$= \delta(a_0 - [a_1 \cos N_s\alpha + a_2 \cos 2N_s\alpha])(b_0 - [b_1 \cos N_r(\alpha - \alpha_r) + b_2 \cos 2N_r(\alpha - \alpha_r)])$$

$$= \delta[a_0 b_0 - a_0 b_1 \cos N_r(\alpha - \alpha_r) - a_0 b_2 \cos 2N_r(\alpha - \alpha_r) - a_1 b_0 \cos N_s\alpha +$$

$$+ a_1 b_1 \cos N_s\alpha \cos N_r(\alpha - \alpha_r) + a_1 b_2 \cos N_s\alpha \cos 2N_r(\alpha - \alpha_r) - a_2 b_0 \cos 2N_s\alpha +$$

$$+ a_2 b_1 \cos 2N_s\alpha \cos N_r(\alpha - \alpha_r) + a_2 b_2 \cos 2N_s\alpha \cos 2N_r(\alpha - \alpha_r)] \tag{4.59}$$

and after rearrangement and applying the following trigonometric identity

$$\cos A \cos B = \frac{1}{2}[\cos(A - B) + \cos(A + B)] \tag{4.60}$$

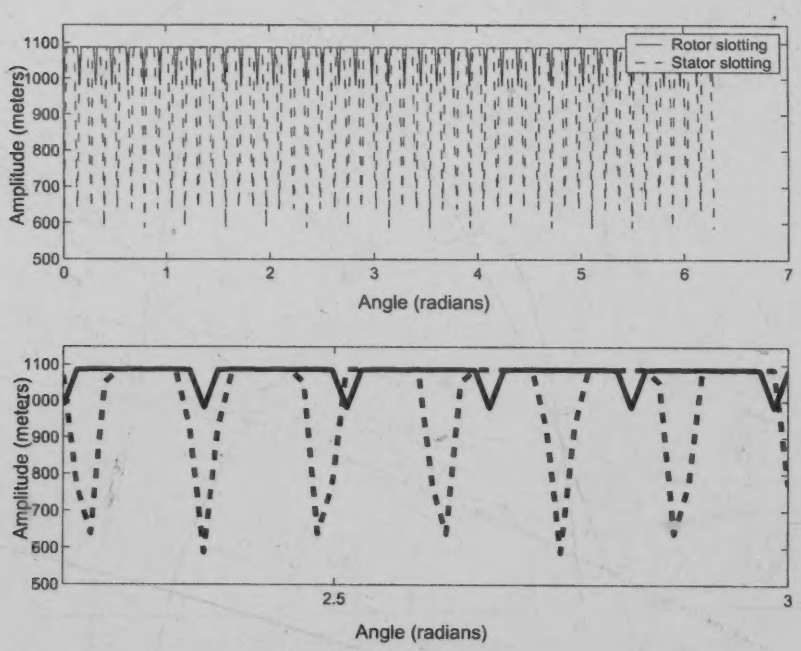

Figure 4.10: Stator and rotor slots harmonics as function of $f_{1,2}(\alpha)$

equation 4.59 takes the form:

$$\lambda_{s,r} = \frac{1}{\delta}\left\{\frac{1}{K_{c1}K_{c2}} - \frac{a_1}{K_{c2}}\cos N_s\alpha - \frac{b_1}{K_{c1}}\cos N_r(\alpha-\alpha_r)+\right.$$

$$+\frac{a_1b_1}{2}[\cos((N_s-N_r)\alpha+N_r\alpha_r)+\cos((N_s+N_r)\alpha-N_r\alpha_r)]-$$

$$-\frac{a_2}{K_{c2}}\cos 2N_s\alpha - \frac{b_2}{K_{c1}}\cos 2N_r(\alpha-\alpha_r)+$$

$$+\frac{a_1b_2}{2}[\cos((N_s-2N_r)\alpha+2N_r\alpha_r)+\cos((N_s+2N_r)\alpha-2N_r\alpha_r)]+$$

$$+\frac{a_2b_1}{2}[\cos((2N_s-N_r)\alpha+N_r\alpha_r)+\cos((2N_s+N_r)\alpha-N_r\alpha_r)]+$$

$$\left.+\frac{a_2b_2}{2}[\cos((2N_s-2N_r)\alpha+2N_r\alpha_r)+\cos((2N_s+2N_r)\alpha-2N_r\alpha_r)]+\ldots\right\} \quad (4.61)$$

In this case, the resultant magnetic conductance of the airgap includes harmonics of the order N_s and N_r corresponding to the stator and rotor slotting. Hence, the airgap flux density from equation 4.49 takes the form:

$$B(x,t) = MMF(x,t) \cdot \lambda_{s,r}(x,t) \tag{4.62}$$

$$B(x,t) = \lambda_{s,r} \cdot \hat{F} \sum_{k=0}^{\infty} \frac{1}{p(6k \mp 1)} K_{wk} cos\left(\omega t \pm p(6k \mp 1)\frac{\pi}{\tau_p} x\right) \tag{4.63}$$

where $\hat{F} = \frac{3\mu W I \sqrt{2}}{\pi}$.

Figure 4.11 depicts the airgap flux density waveform obtained from equation 4.63. In this case, the permeance function includes the stator and rotor slot harmonics for a 2 pair pole machine with 48 stator slots and 40 rotor slots.

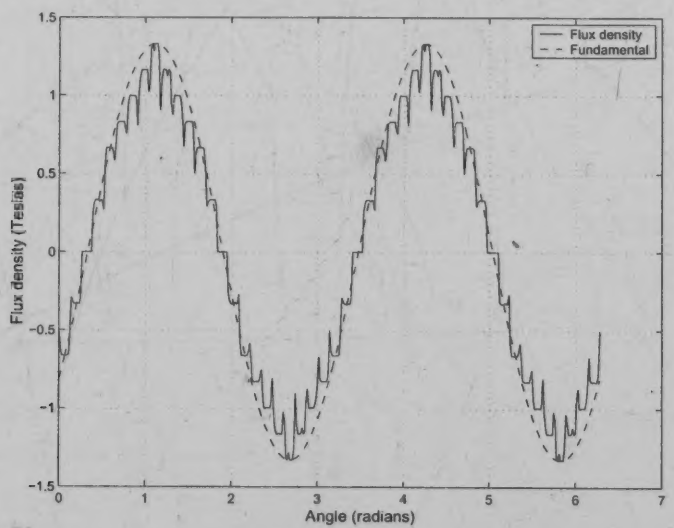

Figure 4.11: Airgap flux density

Situated in the stator reference frame, one can consider the v^{th} space harmonic with the fundamental $n = 1$ time harmonic of equation 4.63 for a slotted N_s stator and N_r rotor. Hence, the rotor slot harmonic frequencies seen in the current spectra can be obtained as

$$B_v(\alpha,t) = \hat{F}\cos(\omega t + vp\alpha) \cdot \lambda_{s,r} \tag{4.64}$$

$$B_v(\alpha,t) = \frac{\hat{F}}{\delta}\cos(\omega t + vp\alpha)\{a_0' - a_1' \cos N_s\alpha - b_1' \cos N_r(\alpha - \alpha_r) +$$

$$+\frac{a_1 b_1}{2}[\cos((N_s - N_r)\alpha + N_r\alpha_r) + \cos((N_s + N_r)\alpha - N_r\alpha_r)] - \ldots\Big\} \qquad (4.65)$$

and after rearrangement and by applying the trigonometric identity of equation 4.60

$$B_v(\alpha, t) = \frac{\hat{F}}{\delta}\{a_0' \cos(\omega t + vp\alpha) + \ldots -$$

$$-\frac{b_1'}{2}[\cos(\omega t + (vp - N_r)\alpha + N_r\alpha_r) + \cos(\omega t + (vp + N_r)\alpha - N_r\alpha_r)] +$$

$$+\frac{a_1 b_1}{4}\{[\cos(\omega t + (vp - N_s + N_r)\alpha - N_r\alpha_r) + \cos(\omega t + (vp + N_s - N_r)\alpha + N_r\alpha_r)] + \ldots +\} -$$

$$-\frac{b_2'}{2}[\cos(\omega t + (vp - 2N_r)\alpha + 2N_r\alpha_r) + \cos(\omega t + (vp + 2N_r)\alpha - 2N_r\alpha_r)] + \ldots +$$

$$+\frac{a_1 b_2}{4}\{[\cos(\omega t + (vp - N_s + 2N_r)\alpha - 2N_r\alpha_r) +$$

$$+\cos(\omega t + (vp + N_s - 2N_r)\alpha + 2N_r\alpha_r)] + \ldots +\} + \ldots +\} \qquad (4.66)$$

$$B_v(\alpha, t) = \frac{\hat{F}}{\delta} \cdot \hat{M}_{ak,bk} \cos(\omega t + (vp \pm k(N_s + N_r)\alpha \pm kN_r\alpha_r) \qquad (4.67)$$

where $\hat{M}_{ak,bk}$ is the magnitude of each harmonic, $k = 0, 1, 2, 3, \ldots$ and α_r is the periphery coordinate along the machine bore referred to the stator when the rotor is rotating at an angular velocity ω_r.

$$\omega_r = \frac{(1 - s)}{p}\omega \qquad (4.68)$$

Consequently, the harmonic series of the airgap flux density distribution of equation 4.67 due to stator and rotor slotting will induce current harmonics of the same order in the stator winding. Thus, these components can be seen in the current spectrum by looking at the frequencies given by

$$f_{rsh} = f_e \pm kN_r\frac{(1 - s)}{p}f_1 \qquad (4.69)$$

where f_{rsh} is defined as the rotor slot harmonics, s is the slip, f_e is the main supply frequency and f_1 is the fundamental component of the supply frequency ($f_e = f_1$). Equation 4.69 is of great importance to identify the rotor slots harmonic in the current spectrum. These frequency components are affected by the airgap variation in

case of any eccentricity condition in the motor and their change in magnitude can be utilized to recognized such irregularities. Equation 4.69 is used extensively during the experimental testing as described in chapter 7.

In summary, during operation, the rotor slot MMF harmonics will interact with the fundamental component of the air gap flux because of the rotor currents. Therefore, the air gap flux will be modulated by the passing rotor slots, producing rotor slot harmonics (RSH). Hence, the slot harmonics arise from the discrete distribution of the rotor current in a finite number of slots (MMF harmonics) and the permeance variations in the airgap associated with the slot openings.

The mechanical speed information of an induction machine is embedded in the stator currents and the extraction of the rotor speed is possible by looking at the fundamental RSH given by equation 4.69. Hence, the presence of rotor slot harmonics in the frequency spectrum are often utilized in sensorless speed estimation as a medium to control the speed of induction motor drives [40]. Thus, the motor speed in RPM can be calculated using the principal RSH at any slip condition from the following expression:

$$RPM = \frac{60}{N_r}(f_{rsh} \pm f_1) \tag{4.70}$$

where N_r is the number of rotor slots. The rotor slot harmonics are related to the rotor currents, so their magnitude is reduced when decreasing the load, making it sometimes difficult to detect RSH at low load levels [40].

4.9 Rotor Eccentricity

The rotor in an induction motor is ideally supported in its bearing eccentrically with respect to the stator. Due to stator and rotor manufacturing tolerances and defects, the roundness and eccentric conditions are not accurate. Therefore, a one-side magnetic force, known as unbalanced magnetic pull will be developed that tends to increase the eccentricity and the critical rotor speed of the machine producing considerable vibrations and noise. Figure 4.12 represents an exaggerated condition

of an eccentric rotor. The off center of the rotor is displaced by a distance e_s against the stator, so the air gap function $\delta(\alpha)$ under static eccentricity condition in this case is modeled as

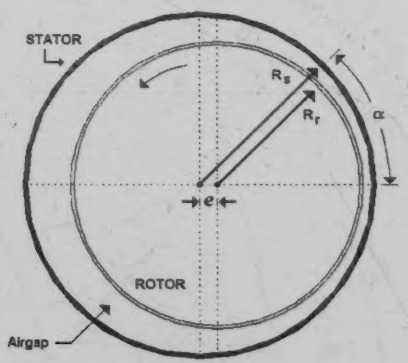

Figure 4.12: Rotor eccentricity

$$\delta_{ecc}(\alpha) = R_s - R_r - e_s \cos\alpha = \delta_m - e_s \cos\alpha \tag{4.71}$$

where R_s is the stator radius, R_r is the rotor radius and $\delta_m = R_s - R_r$ is the mean airgap of the machine. Consequently, the airgap function that includes the static and dynamic eccentricities in the machine is defined as:

$$\delta_{ecc}(\alpha, t) = \delta_m(1 - \epsilon_s \cos\alpha - \epsilon_d \cos(\alpha - \omega_r t)) \tag{4.72}$$

where $\epsilon_{s,d}$ is the degree of static or dynamic eccentricity

$$\epsilon_{s,d} = \frac{e_{s,d}}{\delta_m} \tag{4.73}$$

It is seen from equation 4.72 that the eccentricity is static if the angle (α) is a constant. The rotor rotates around its axis, but it is shifted with respect to the stator axis by e_s. Similarly, the eccentricity is dynamic if the angle α is dependent on the rotor motion. The axis of rotor revolution may coincide with the stator axis, but the rotor axis of symmetry is shifted by e_d.

Inversion of equation 4.72 leads to the magnetic conductance or permeance function of the airgap $\lambda_{ecc}(\alpha, t)$

$$\lambda_{ecc}(\alpha,t) = \frac{1}{\delta_{ecc}(\alpha,t)} = \frac{1}{\delta_m(1-\epsilon_s\cos\alpha - \epsilon_d\cos(\alpha-\omega_r t))} \tag{4.74}$$

If equation 4.74 is expressed as a Fourier series, then equation 4.74 may be expressed as

$$\lambda_{ecc}(\alpha,t) = \frac{1}{\delta_m}\{\lambda_0 + \lambda_1[\cos\alpha + \cos(\alpha-\omega_r t)] + ...\} \tag{4.75}$$

where in the range $\epsilon < 0.7$ it holds approximately that [39]:

$$\lambda_0 \approx \frac{1}{1-\frac{\epsilon^2}{2}} \tag{4.76}$$

$$\lambda_1 \approx \frac{\epsilon}{1-\frac{\epsilon^2}{2}} \tag{4.77}$$

It is observed that the magnitudes of equations 4.76 and 4.77 will increase as the level of eccentricity increases. Therefore, the flux density distribution of equation 4.49 with the integration of static and dynamic eccentricities in the machine is of the form

$$B(x,t) = MMF(x,t)\cdot\lambda_{ecc(s,d)}(\alpha,t) \tag{4.78}$$

$$B(x,t) = \lambda_{ecc(s,d)}\cdot\hat{F}\sum_{k=0}^{\infty}\frac{1}{p(6k\mp 1)}K_{wk}cos\left(\omega t \pm p(6k\mp 1)\frac{\pi}{\tau_p}x\right) \tag{4.79}$$

The flux density distribution when static or dynamic eccentricity is presented in the machine can be calculated from equation 4.79. Situated in the stator reference frame and considering the v^{th} space harmonic with the fundamental ($n = 1$) time harmonic, the frequency components that are seen in the current spectra may be obtained as

$$B_v(\alpha,t) = \frac{\hat{F}}{\delta}\cos(\omega t + vp\alpha)\cdot\lambda_{ecc(s,d)} \tag{4.80}$$

$$B_v(\alpha,t) = \frac{\hat{F}}{\delta}\cos(\omega t + vp\alpha)\{\lambda_0 + \lambda_1[\cos\alpha + \cos(\alpha-\omega_r t)] + ...\} \tag{4.81}$$

$$B_v(\alpha,t) = \frac{\hat{F}}{\delta}\{\lambda_0\cos(\omega t + vp\alpha) + \\ +\lambda_1\cos(\omega t + vp\alpha)\cos\alpha + \lambda_1\cos(\omega t + vp\alpha)\cos(\alpha - \omega_r t + \ldots\} \quad (4.82)$$

and after rearrangement and by applying the trigonometric identity of equation 4.60

$$B_v(\alpha,t) = \frac{\hat{F}}{\delta}\{\lambda_0\cos(\omega t + vp\alpha) + \\ +\frac{\lambda_1}{2}[\cos(\omega t + (vp-1)\alpha) + \cos(\omega t + (vp+1)\alpha)] + \\ \frac{\lambda_1}{2}[\cos(\omega t + (vp-1)\alpha + \omega_r t) + \cos(\omega t + (vp+1)\alpha - \omega_r t)] + \ldots\Big\} \quad (4.83)$$

From equation 4.83 it is seen that the rotor eccentricity causes additional fields of $(vp+1)$ pole pairs. Furthermore, the presence of dynamic eccentricity in the motor should produce harmonic components in the stator currents that can be identifiable by looking at frequencies given by

$$f_{ecc} = n\omega \pm \omega_r \quad (4.84)$$

$$f_{ecc} = f_e(n \pm \frac{(1-s)}{p}) \quad (4.85)$$

where $n = 1, 2, 3, \ldots$ is the time harmonic order. It is observed from equation 4.85 that the presence of sidebands at $\pm\omega_r$ around the fundamental component (60Hz) in the current spectrum are indicative of dynamic eccentricity in the motor. Ideally, the magnitude of these sidebands should be zero for a healthy machine, but due to inherent levels of mixed eccentricity in the motor, the presence of these sidebands should be observed in the spectrum. Furthermore, any change in magnitude of these components should indicate that the eccentricity condition is increasing. Simulation results and experimental testing present the apparition of these sidebands as discussed in chapters 5 and 7.

4.10 Flux Density Harmonics

In the previous sections, it is discussed that several factors affect the sinusoidal variation of the airgap flux density. The effect of stator and rotor slotting, rotor eccentricity, winding space and time harmonics give rise to multiple airgap flux density harmonic components. These harmonics are sampled by the stator winding and are present in the stator current spectrum. Thus, a general expression of the permeance function in the airgap can be defined as a combination of the slotting and eccentricity functions:

$$P(\alpha,t) = \lambda_{slots(s,r)}(\alpha,t) + \lambda_{ecc(s,d)}(\alpha,t) \tag{4.86}$$

and in a general form

$$P = P_0 + \sum_{k=1}^{\infty} P_{ssk}\cos(kN_s\alpha + \phi_{ssk}) + \sum_{k=1}^{\infty} P_{rsk}\cos(kN_r(\alpha - \omega_r t) + \phi_{rsk}) + \\ + P_{se}\cos(\alpha + \phi_{se}) + P_{de}\cos(\alpha - \omega_r t + \phi_{de}) \tag{4.87}$$

where: P_0 = average airgap $(1/g_0)$, P_{ss} = permeance function for N_s stator slots, P_{rs} = permeance function for N_r rotor slots, P_{se} = permeance function for static eccentricity, P_{de} = permeance function for dynamic eccentricity, ω_r = rotor rotational speed and ϕ = a phase angle.

Each one of the terms of equation 4.87 interacts with the MMF spatial distribution that contributes to the apparition of frequency components in the airgap flux density. Equation 4.87 presents the effects related to slotting and eccentricity conditions and it is used in chapter 5 to calculate and simulate the airgap flux density. Furthermore, the integration of more components that affect the airgap flux density can be included in the permeance function of equation 4.87. As an example, saturation effects can be included in the analysis, however this is not included in this work.

4.11 The Reference Frame

According to the analysis of sections 4.8.1 and 4.9, information related to stator slotting and static eccentricity is not readily available neither in the stator reference

frame nor in the stator current spectrum. However, the flux density in the airgap induces rotor currents, which in turn produces airgap flux harmonics that include the effects of stator slotting and static eccentricity. Thus, these components should be identifiable in the stator current spectrum. The rotor reference frame is then utilized by using the following transformation:

$$\alpha = \varphi + \omega_r t \tag{4.88}$$

where φ is an angular distance around the rotor circumference which is stationary with respect to the rotor reference frame and $\omega_r t$ is the angular displacement of the rotor with respect to the stator reference frame. This is illustrated in figure 4.13.

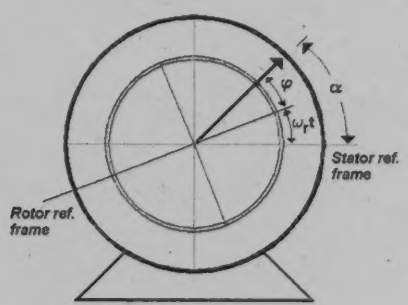

Figure 4.13: Reference frame

Hence, a new set of frequencies can be found in the rotor reference frame that include the stator slot harmonics and static eccentricity. Table 4.4 presents the frequencies that are found by using the MMF expression of equation 4.49 with the permeance function of equation 4.87 and the reference frame transformation of equation 4.88.

The speed of rotation of the rotor magnetic field in the stator reference frame is given by equation 4.89

$$\omega_s = \omega_r \pm f_{rotor} \tag{4.89}$$

Therefore, the induced rotor currents at frequencies given in table 4.4 produce airgap flux density harmonics in the stator reference frame at the following frequencies:

Table 4.4: Airgap flux density components in the rotor reference frame

Source	*Frequencies*
$(MMF \cdot P_{se})\|_r$	$f_e \pm (vp \pm 1)\frac{(1-s)}{p} f_1$
$(MMF \cdot P_{de})\|_r$	$f_e \pm (1-s) f_1$
$(MMF \cdot P_{ss})\|_r$	$f_e \pm (vp \pm kN_s)\frac{(1-s)}{p} f_1$
$(MMF \cdot P_{rs})\|_r$	$f_e \pm (1-s) f_1$

$$(MMF \cdot P_{se})|_s \longmapsto \quad (1-s)f_1 \pm f_e \pm (vp \pm 1)\frac{(1-s)}{p} f_1 \tag{4.90}$$

$$(MMF \cdot P_{ss})|_s \longmapsto \quad (1-s)f_1 \pm f_e \pm (vp \pm kN_s)\frac{(1-s)}{p} f_1 \tag{4.91}$$

Frequency components related to static eccentricity and stator slot harmonics and given by equations 4.90 and 4.91 respectively, should be identified in the stator current spectrum.

4.11.1 The MMF of squirrel cage rotor

A squirrel-cage rotor winding with N_r slots and a machine with $p-$pole-pairs may be replaced by a winding with m phases and $q = 1$ slot per pole per phase [39], where

$$m = \frac{N_r}{p} \tag{4.92}$$

$$q_r = \frac{N_r}{p * m} = 1 \tag{4.93}$$

The MMF generated by this winding carrying the current I is obtained by following the same procedure as in section 4.5.1. Considering a machine with 40 rotor slots and 2 pole pairs, then $m = 20$ per pole pair and $q = 1$ slot per pole per phase. By adding the positive and negative sequences of equation 4.24, certain combinations of the spatial and time harmonics are generated. This is illustrated in table 4.5 created for a cage winding with $m = 20$ phases.

Table 4.5: MMF spatial and time harmonics combinations for a squirrel-cage rotor winding

	v	space								
n		1	3	5	15	17	19	21	23	25
	1	$+1\omega$	0	0	0	0	-19ω	$+21\omega$	0	0
	3	0	$+3\omega$	0	0	-17ω	0	0	$+23\omega$	0
	5	0	0	$+5\omega$	-15ω	0	0	0	0	$+25\omega$

Therefore, the first terms of the rotor MMF spatial distribution when a symmetrical and balance current is supplied to the machine (only fundamental current component considered $n = 1$) follows from the positive or negative sequence as shown in table 4.5

$$F(x,t) = \frac{N_r I K_{dn(r)}}{p\pi}\left(cos(\omega t - p\alpha) - \frac{1}{19}cos(\omega t + p\alpha) + \frac{1}{21}cos(\omega t - p\alpha) - \right.$$
$$\left. - \frac{1}{39}cos(\omega t + p\alpha) + \frac{1}{41}cos(\omega t - p\alpha) - \ldots\right) \quad (4.94)$$

and in a general form

$$MMF_r(x,t) = \frac{N_r I K_{dn(r)}\sqrt{2}}{p\pi\delta} \sum_{v=k\frac{N_r}{p}\pm 1}^{\infty} \frac{1}{p(k\frac{N_r}{p} \pm 1)} \cos(\omega t \pm p(k\frac{N_r}{p} \pm 1)\alpha) \quad (4.95)$$

The distribution factor for $q = 1$ will be, according to equation 4.37

$$K_{dn(r)} = 1 \quad (4.96)$$

One term of equation 4.95 describes a MMF distribution which varies sinusoidally in both space and time. Due to full symmetry of the cage with q as an integer, a distribution factor $K_{dn(r)} = 1$ and the combination of the phase sequence, the forward-revolving field frequencies at harmonics of v_f and the backward-revolving fields at harmonics of v_b will describe the rotor MMF. That is

$$v = v_{f,b} = (k\frac{N_r}{p} \pm 1) \quad (4.97)$$

where, $k = 0, 1, 2, 3, \ldots$. These harmonics are referred as the step harmonics of the rotor magnetic field.

Figure 4.14 depicts the traveling rotor MMF wave in space along the airgap of a machine with 40 rotor slots, $p = 2$ and $K_{dn(r)} = 1$ for various instants of time according to equation 4.95 when a balanced 60 Hz sinusoidal current is supplied.

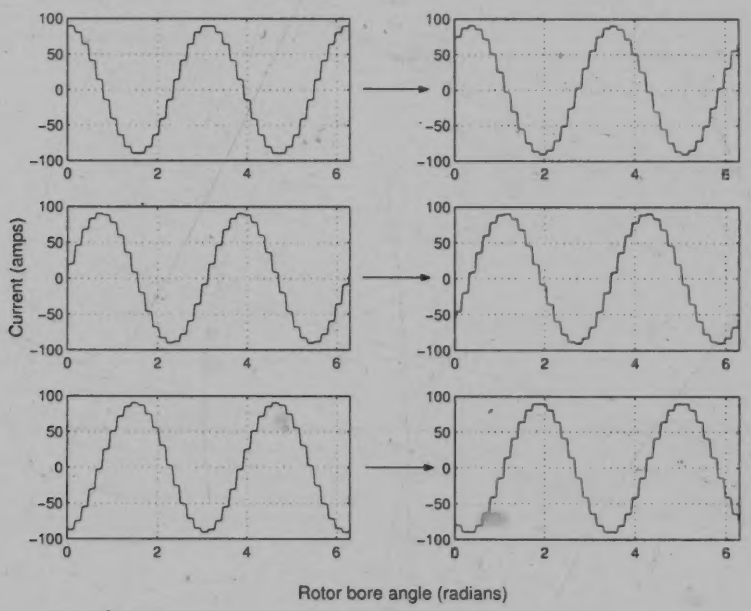

Figure 4.14: Rotor MMF space traveling wave along the airgap

The resultant MMF in the airgap of the machine is the sum of stator and rotor MMFs. The total MMF is found by using equations 4.28 and 4.95.

$$MMF_t(\alpha, t) = MMF_s(\alpha, t) + MMF_r(\alpha, t) \cdot Sk_f \tag{4.98}$$

Equation 4.98 is used in the matlab program to calculate the total MMF in the airgap of the machine. Hence, equations 4.87 and 4.98 are used in chapter 5 to calculate the flux density distribution in the airgap of the machine using the matlab program of appendix A. The application of the FFT to the waveform obtained present the frequency components due to stator and rotor slotting and eccentricity conditions in the motor.

4.12 The Skewed Rotor

The die-cast rotors of medium size induction motors are commonly skewed by one rotor bar pitch to reduce torque ripple effects and acoustic noise that can arise from slotting effects. In a skewed rotor, the phase of the rotor MMF with respect to the stator MMF will change along the length of the machine, producing an axial variation in the airgap flux density [41].

The skew of the slots is generally accomplished by spiraling the rotor slots in the manner indicated in figure 4.15. The effect of skewing is to introduce an angle ψ in the rotor bars with respect to the axial length of the machine, so the resultant voltage induced in the skewed bar will be reduced in comparison with the unskewed bar by a ratio that is called the skew factor. In this way, the first rotor slotting harmonic is reduced considerably. The skew factor (Sk_f) may be obtained by integrating the flux linking a closed loop formed by two adjacent bars and it is given by

$$Sk_f = \frac{\frac{\sin vpl\psi}{2R}}{\frac{vp\psi l}{2R}} \tag{4.99}$$

where l is the axial length of the rotor cage, R is the radius of the machine bore and v is the harmonic flux order [39].

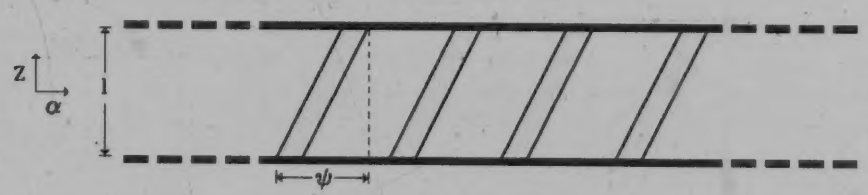

Figure 4.15: Skewing of rotor slots

4.13 Summary

The theoretical analysis presented in this chapter illustrates a variety of equations which are used to predict a set of frequencies and that can be identified in the current spectrum. These frequencies are used to determined the step harmonics, motor speed,

slot harmonics and the presence of airgap eccentricities in the motor. Tables 4.6 and 4.7 summarizes the equations to calculate these set of frequencies.

Table 4.6: Summary of equations to determined the set of frequencies identifiable in the current spectrum: slotting and airgap eccentricities

$MMF_{s,r}$	Permeance	Frequency	Ref. frame
$\hat{F}_s \cos(\omega t \pm vp\alpha)$	P_o	ω	stator
$\hat{F}_r \cos(s\omega t \pm vp\varphi)$	P_o	$s\omega$	rotor
$\hat{F}_s \cos(\omega t \pm vp\alpha)$	$\sum P_{rsk} \cos(kN_r(\alpha - \omega_r t))$	$f_e \pm kN_r \frac{(1-s)}{p} f_1$	stator
$\hat{F}_r \cos(s\omega t \pm vp\varphi)$	$\sum P_{ssk} \cos(kN_s\alpha)$	$f_e \pm (vp \pm kN_s)\frac{(1-s)}{p} f_1$	rotor
$\hat{F}_s \cos(\omega t \pm vp\alpha)$	$P_{se} \cos(\alpha + \phi_{se})$	$f_e(n \pm \frac{(1-s)}{p})$	stator
$\hat{F}_r \cos(s\omega t \pm vp\varphi)$	$P_{de} \cos(\alpha - \omega_r t + \phi_{de})$	$f_e \pm (vp \pm 1)\frac{(1-s)}{p} f_1$	rotor

Table 4.7: Summary of equations to determined the set of frequencies identifiable in the current spectrum: step harmonics and rotor speed

Information	Frequency
Stator step harmonics	$v = 2mkq \pm 1$
Rotor step harmonics	$v = (k\frac{N_r}{p} \pm 1)$
Rotor speed	$f_{rsh} \mapsto RPM = \frac{60}{N_r}(f_{rsh} \pm f_1)$

Chapter 5

Simulations

The flux density traveling wave given by equation 5.1 is evaluated in order to investigate and recognize the effects of slotting the stator and rotor, skewing the rotor bars and introducing static eccentricity during normal operation of the motor. The permeance function presented in equation 4.87 along with the total MMF due to the stator and rotor magnetic fields given by equation 4.98 are used to calculate the flux density distribution in the motor. The frequency components that describe these conditions are found after applying the FFT to the waveform obtained. Results are presented and discussed.

$$B(\alpha, t) = (MMF_s + MMF_r) \cdot P(\alpha, t) \tag{5.1}$$

5.1 Permeance Model Calculation and Skew Effect

The model described by equation 5.1 is evaluated with a program created in Matlab (described in appendix A). The model is based directly on the geometry of the induction machine and the physical layout of all the windings. Initially, the following assumptions were made:

1. Magnetic saturation of the machine is neglected. It is assumed that the iron is infinitely permeable.

2. Eddy current, friction and windage losses are neglected. The supply current is assumed of constant magnitude, varying sinusoidally in time.

3. Rotor bars' inductances are neglected in order to calculate numerically the value of the total current in the rotor bars.

The motor parameters used in this model are illustrated in table 5.1

Table 5.1: Motor data

	Stator	*Rotor*
Slots	48	40
$\alpha_{el(s,r)}$	$\frac{\pi}{24}$	$\frac{\pi}{20}$
$\beta_{s,r}$	0.23	0.048
$o_{s,r}$	2.735 mm	1 mm
$t_{d(s,r)}$	11.304 mm	13.420 mm
q	4	1
p pole pairs	2	
Full load speed	1740 rpm	
Stator & rotor length	161 mm	
Supply frequency	60 Hz	
Airgap (δ)	0.92 mm	

The algorithm that describes the calculations is as follows

1. The stator MMF is calculated according to equation 4.28.

2. The permeance function of the airgap is obtained by adding the effects of stator and rotor slotting and static and dynamic eccentricity calculated with equation 4.87. The effect of skewing the bars is taken into account by dividing the axial length of the rotor bars into m unskewed segments. (m is chosen to be 5 in the simulations). The permeance function is then calculated for each fragment since the value of the slotting and eccentricities functions vary with the position of the rotor bar with respect to a fixed point in the stator frame. Figure 5.1 illustrates the rotor bar segmentation.

   The current path that flows in each of the loops formed with adjacent bars of the rotor cage is illustrated in figure 5.1. The rotor bars are shorted together

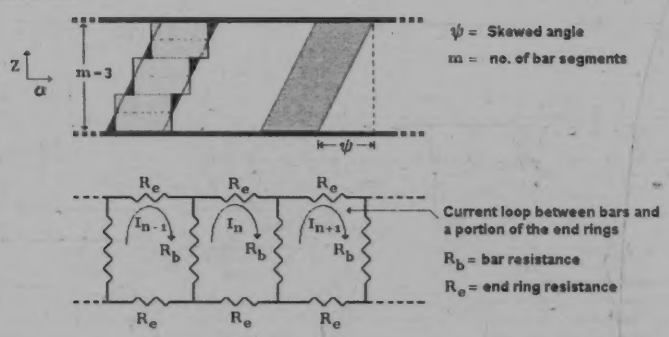

Figure 5.1: Skewing of rotor slots and fragmentation

by end rings. Therefore bar and end ring voltages are dropped across bar and end ring resistances generating currents in the loops. The current induced in each loop is obtained by calculating the voltage induced in the cage due to the flux linkage of the stator flux density and then applying ohm's law to the circuit (bar inductance is neglected). Hence,

(a) The airgap flux density due to the stator windings is obtained with

$$B_s(\alpha, t) = MMF_s(\alpha, t) \cdot P(\alpha, t) \tag{5.2}$$

(b) The voltage induced per loop and per segment of the rotor cage is

$$e(\alpha, t) = -\frac{\delta \lambda_r}{\delta t}\left(\int_{\alpha_{bar(n)}+\omega_r t}^{\alpha_{bar(n+1)}+\omega_r t} B(\alpha, t)\delta\alpha\right) \quad for\ unskewed\ rotor \tag{5.3}$$

$$e(\alpha, t) = -\frac{\delta \lambda_r}{\delta t}\left(\int_0^L \int_{\alpha_{bar(n)}+\omega_r t}^{\alpha_{bar(n+1)}+\omega_r t} B(\alpha, t, z)\delta\alpha\delta z\right) \quad for\ skewed\ rotor \tag{5.4}$$

(c) The current in each bar is considered as an independent variable with just the real component. The rotor cage is composed of n identical and equally spaced rotor loops and i_{lrk} is the current in the k_{ht} loop, where k is any arbitrarily chosen integer ($1 \leq k \leq n$). The first current loop may consist

of the currents passing through the first and the second rotor bars and the connecting portions of the end rings between them. The second current loop consist of the currents passing through the second and the third rotor bars and the connecting portions of the end rings between them. The k_{th} current loop consists of the currents passing through the k_{th} and the first rotor bars and the connecting portions of the end rings between them. Hence, the voltage equations for the rotor loops are

$$V_r = R_r I_r + \frac{d\lambda_r}{dt} + L\frac{dI_r}{dt} \tag{5.5}$$

where,

$$V_r = [V_{1r} V_{2r} V_{3r} \dots V_{nr}]^t \tag{5.6}$$

$$I_r = [I_{1r} I_{2r} I_{3r} \dots I_{nr}]^t \tag{5.7}$$

In the case of a cage rotor, the rotor loop voltages are zero. That is, $V_{kr} = 0$ for $k = 1, 2, 3, \dots n$. Therefore, the current distribution can be specified in terms of n independent rotor loop currents. Neglecting the inductance term, the voltage equations for the rotor loops in vector matrix form can be written as:

$$\begin{aligned} 1^{st}\ loop &: V_r = 2(R_b + R_e) i_{lr1} - R_b i_{lrk} - R_b i_{lr2} \\ 2^{nd}\ loop &: V_r = 2(R_b + R_e) i_{lr2} - R_b i_{lr1} - R_b i_{lr3} \\ &\vdots \\ k^{th}\ loop &: V_r = 2(R_b + R_e) i_{lrk} - R_b i_{lrk-1} - R_b i_{lr1} \end{aligned} \tag{5.8}$$

where, V_r is the rotor loop voltage, R_b is the rotor bar resistance, R_e is the end ring resistance and i_{lrk} is the current in the k^{th} loop. From equation 5.8, a $n * n$ symmetric matrix of the rotor bars and end ring resistance R_r can be formed:

$$\begin{pmatrix} 2(R_b+R_e) & -R_b & 0 & \dots & 0 & -R_b \\ -R_b & 2(R_b+R_e) & -R_b & \dots & 0 & 0 \\ \vdots & \vdots & \vdots & \vdots & \vdots & \vdots \\ 0 & 0 & 0 & \dots & 2(R_b+R_e) & -R_b \\ -R_b & 0 & 0 & \dots & -R_b & 2(R_b+R_e) \end{pmatrix}$$

At each time step, the magnitude of the total rotor bars' current along the cage is calculated by equation 5.9. Therefore, the rotor MMF may be obtained as the product iN.

$$i(\alpha,t) = R_r^{-1} e(\alpha,t) \tag{5.9}$$

3. The rotor MMF is calculated according to equation 4.95 with the magnitude of the rotor current found in step 2.

4. Stator MMF and rotor MMF are added together to obtain the total MMF in the airgap.

5. The airgap flux density is then obtained by averaging the flux density calculated for each segment of the rotor bar. Then, $B_{airgap}(\alpha,t) = MMF_T(\alpha,t) \cdot P(\alpha,t)$.

6. The FFT is applied to $B(\alpha,t)$ to obtain the flux density spectrum. Figure 5.2 a) illustrates the spectrum of a simulated healthy motor. The fundamental supply frequency (60Hz) and the rotor slot harmonics are observed.

The previous analysis is carried out using the stator reference frame. However, the effects due to stator slotting and airgap static eccentricity seen from the rotor have to be taken into account. This can be achieved by following the above procedure but this time situated in the rotor reference frame. Hence, a different set of frequencies can be found and added to the frequency spectrum. The flux density spectrum for this case is depicted in 5.2 b). The fundamental supply frequency (60Hz) and the stator slot harmonics are observed.

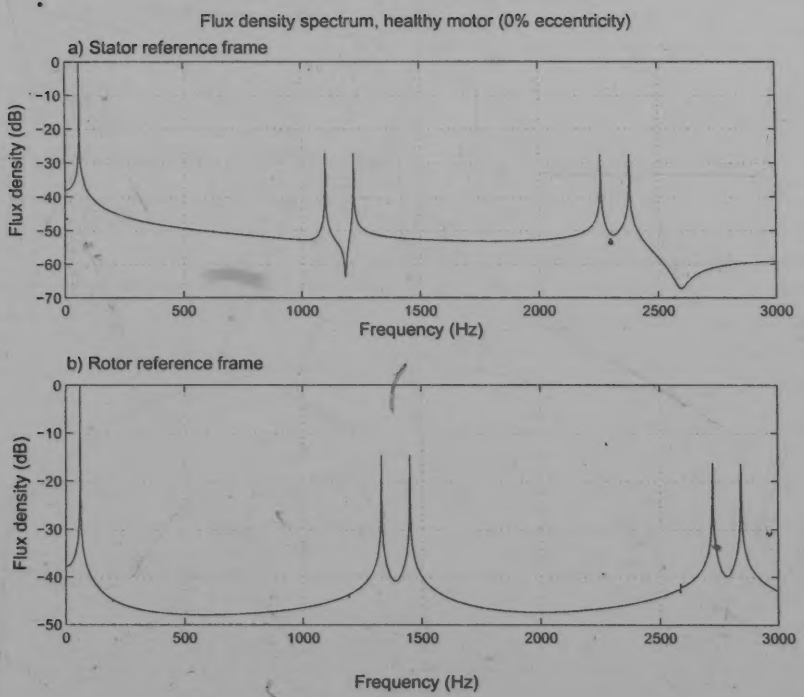

Figure 5.2: Simulated airgap flux density FFT spectrum with 0% eccentricity

5.2 Simulation Results

The program is capable of simulating both a skewed and an unskewed rotor cage. Different degrees of static and dynamic eccentricty can be introduced in the model. Hence, a comparison of the flux density spectrum with different degrees of eccentricity along with the effect of stator and rotor slotting for both skewed and unskewed rotors are considered in the simulations.

1) Eccentricity

Figure 5.3 illustrates the apparition of the low frequency sidebands due to the introduction of a nominal 5% dynamic eccentricity with 0%, 30% and 60% static eccentricity for both a skewed and unskewed rotor. These sidebands at $(\omega \pm \omega_r)$ were predicted according to the analysis represented by equation 4.85. It should be noted

that even the smallest deviation of an uniform airgap as in the case of 1% dynamic eccentricity, will distort the airgap uniformity, affecting the airgap permeance and the apparition of the sidebands around the fundamental is expected. Similarly, according to equation 4.90 and situated in the rotor reference frame, sidebands at $\pm\omega_r$ around the fundamental are present. Furthermore, the apparition of flux density components at frequencies of $\omega \pm k\omega_r$ for $k = 2, 3, 4, 5$ can be seen. The magnitude of these frequencies with different degrees of static eccentricities is illustrated in figure 5.4. Table 5.2 summarizes these frequencies.

Table 5.2: Low frequency harmonics seen in the spectrum

Low Frequency harmonics (Hz)			
	k	-	+
	1	31	89
$f_e(1 \pm k\frac{(1-s)}{p})$	2	2	118
$p = 2$	3	-27	147
$rpm = 1760$	4	-56	176
	5	-85	205

b) Stator and rotor slotting

It is presented in chapter 4 that the rotor and stator slot harmonics can be calculated according to equations 4.69 and 4.91 respectively. These harmonics are listed in table 5.3. Figure 5.2 illustrates the apparition of the first and second stator and rotor slot harmonic components for a healthy motor. It is demonstrated in figure 5.5 that indeed the effect of skewing the rotor bars considerably reduces the magnitude of the rotor slot harmonics. Figure 5.7 compares the effect of introducing a nominal 5% dynamic eccentricity along with different percentages of static eccentricity observed in the slotting harmonics for both rotor cases. An increase of magnitude of these components is seen when the eccentricity is higher. Furthermore, the apparition of sidebands at $\pm\omega_r$ around the slotting harmonics also occurs. The same effect arises when situated in the rotor reference frame as illustrated in figure 5.7

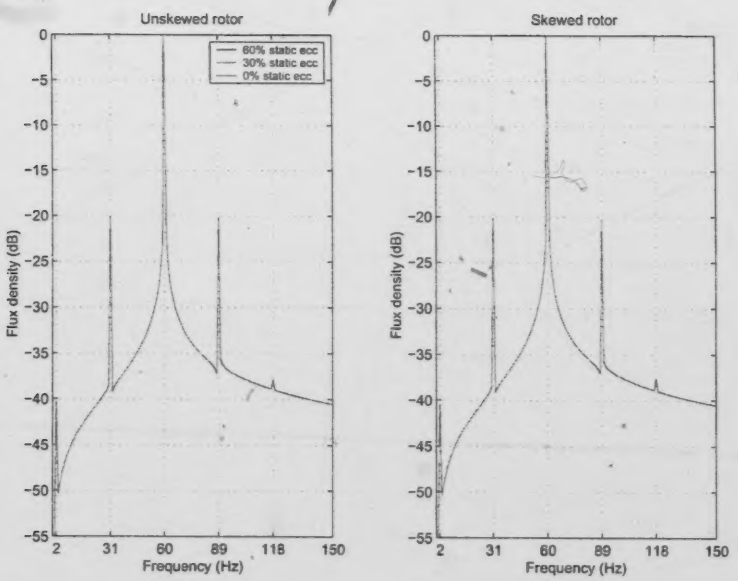

Figure 5.3: Low frequencies of the flux density FFT spectrum seen from the stator reference frame for both a skewed and an unskewed rotor

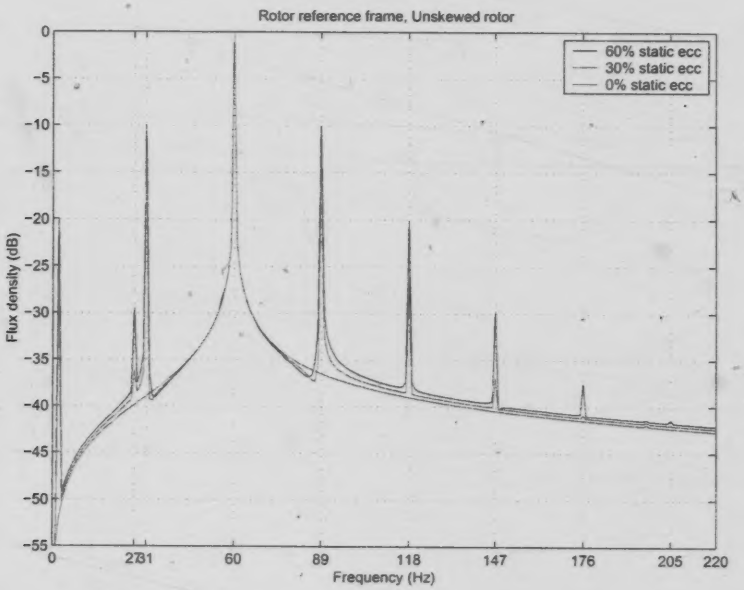

Figure 5.4: Low frequencies of the flux density FFT spectrum seen from the rotor reference frame for an unskewed rotor

Table 5.3: Rotor and stator slot harmonics

Slotting harmonics (Hz)					
		Rotor		*Stator*	
$f_{sh} = f_e \pm kN_{r,s}\frac{(1-s)}{p}f_1$	k	-	+	-	+
$p = 2$	1	1100	1220	1332	1452
$rpm = 1760$	2	2260	2380	2724	2844

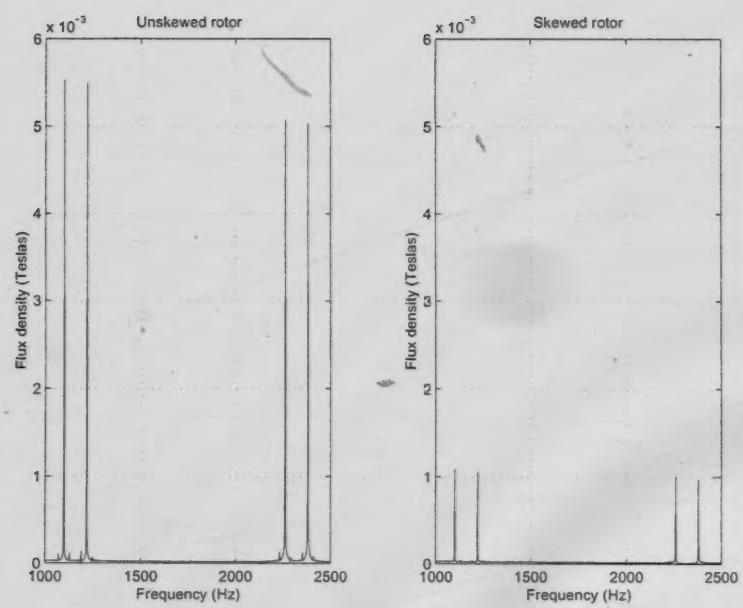

Figure 5.5: Effect of skewing the rotor bars in the rotor slot harmonics of the flux density spectrum

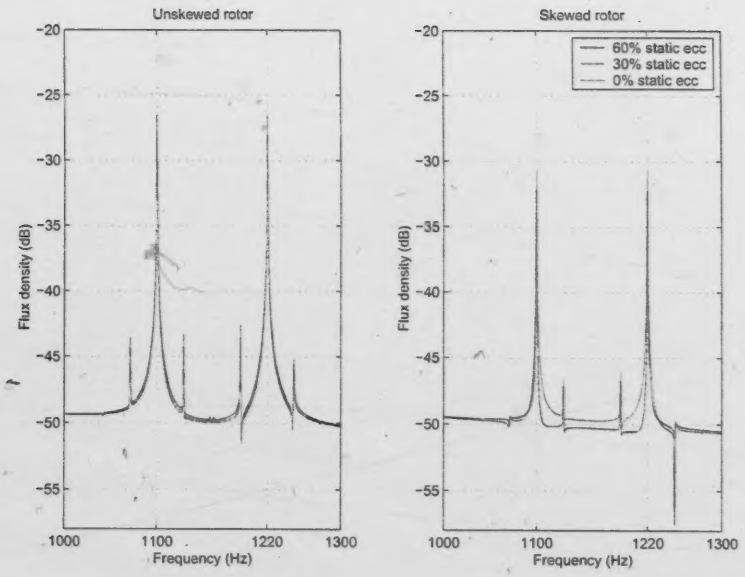

Figure 5.6: Comparison of the rotor slotting harmonics when different percentages of static eccentricity are introduced in the motor seen in the stator reference frame

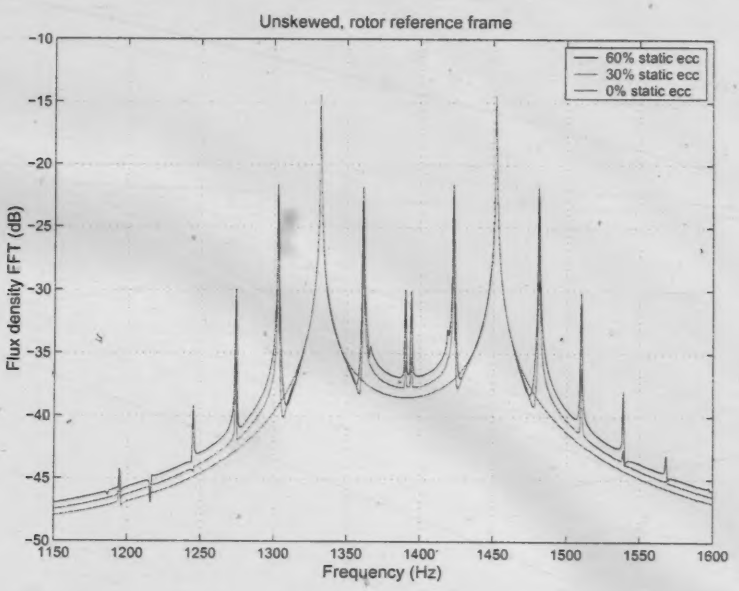

Figure 5.7: Comparison of the stator slotting harmonics when different percentages of static eccentricity are introduced in the motor seen in the rotor reference frame

5.3 Summary

The following results are observed:

1. Frequency components due to stator and rotor slotting are present in the airgap flux density of the machine. Due to the interaction of both the stator and rotor magnetic fields, currents are induced in the stator windings and the airgap flux harmonic components should be observed in the current spectrum.

2. One of the effects of skewing the rotor bars is to reduced the magnitude of the rotor slotting harmonics. However, the magnitude of the low frequency sidebands around the fundamental 60 Hz component due to eccentricity are unchanged.

3. A minimal percentage of dynamic eccentricity and the introduction of different degrees of static eccentricity, considerably affect the permeance function of the airgap and hence the flux density distribution. The presence of the frequency components (sidebands at $\pm\omega_r$) around the fundamental are indicative of dynamic eccentricity in the motor. Frequency components that are related to airgap static eccentricity can be recognized when situated in the rotor reference frame. The sidebands at $\pm\omega_r$ around the fundamental and harmonic components at multiples of the rotational speed are also affected and they appear when static eccentricity is introduced.

4. The apparition of sidebands at $(\pm\omega_r)$ around the slotting harmonics also indicates the presence of an eccentric condition in the motor. At different percentages of static eccentricity the magnitude of those sidebands increased.

Chapter 6

Experimental Test Rig

The focus of this thesis is to identify mechanical irregularities of an induction motor such as bearing faults and airgap eccentricity by means of stator current spectrum analysis. The validation and usefulness of this technique for medium size induction motors is best evaluated by practical experiments. Therefore, a motor test rig was designed and specified for the purpose of measurement and analysis of different levels of static eccentricity and bearing damage. A brief description of this test rig is given next.

6.1 Experimental Setup

The experimental apparatus consists of a three-phase, 30-Hp, 230V, 76.6A, 60-Hz, 4-pole, Δ-connected, skewed squirrel-cage induction motor, fixed to a 208V supply. The induction motor is driven from a three-phase supply grid and it drives a 50 kW DC generator via a flexible coupling which feeds variable resistors to dissipate the load. The loading of the induction motor is controlled through the excitation of the DC field of the generator. The entire test rig was mounted on a metal-frame bed resting on a concrete floor. Figure 6.1 and figure 6.2 show a basic representation of the test rig used for the experiments.

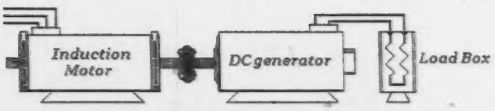

Figure 6.1: Test rig basic representation

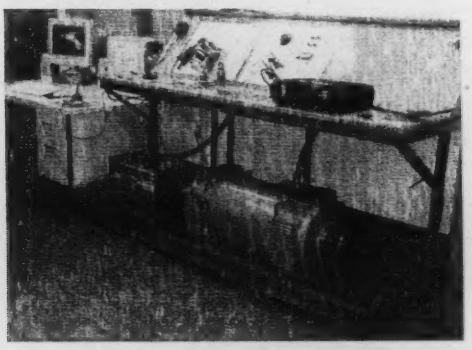

Figure 6.2: Experimental test rig

6.2 Induction Motor Characteristics

The induction motor has $p = 2$ pairs of poles and runs at 1800 rpm when supplied by a 60 Hz network at no-load. The stator core has $Z_1 = 48$ slots where 48 coils are embedded to form a 1 layer concentric winding configuration. Each coil is formed of 18 turns with a wire size no. 17 AWG. The rotor is a squirrel cage composed of $Z_2 = 40$ aluminum-cast bars. The stator core length is 161 mm and the stator bore radius is 86 mm. Table 6.1 summarizes the characteristics of the motor.

The induction motor has a pair of shielded single row deep groove ball bearings of type NSK 6310z. Each bearing has 8 balls.

Figure 6.3 illustrates the arrangement of the 3-phase concentric winding in the machine. The 48 slots are depicted and each phase is composed of $q = 4$ slots per pole per phase. Thus, there are 4 coils per phase and each coil has 18 turns.

The above parameters are related to each other by the following relationship:

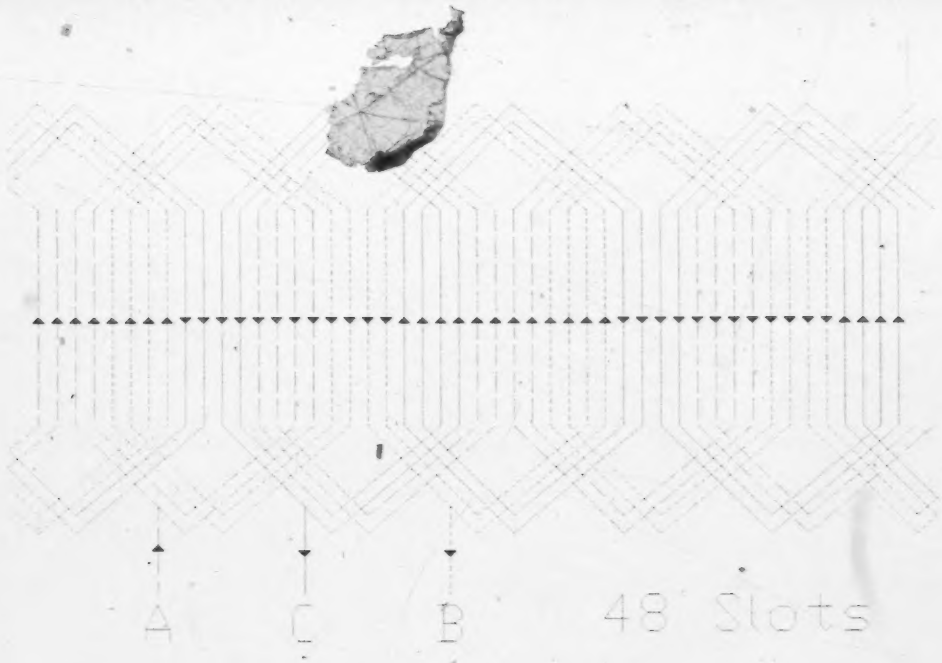

Figure 6.3: Stator winding configuration

$$N_s = m2pq \tag{6.1}$$

where N_s = number of stator slots, m = number of phases, $p = 2$ number of pair poles, $q = 4$ number of slot/pole/phase.

6.2.1 New housing bearings

In an attempt to investigate the effects of static eccentricity in the motor's airgap, both end plates of the machine were removed and new stainless steel bearing housings were designed, manufactured and installed in the machine. Figure 6.4 is a drawing of the new bearing housing. The complete design of the bearing housing is found in appendix B.

The new bearing housings allow a vertical displacement of the rotor center at each end of the machine, facilitating the introduction of a known percentage level of static eccentricity in the system. The vertical movement of the bearing housing is accomplished by means of a threaded bolt at the top of the frame. Once the desired position is reached, the side pieces will securely clamp the bearing housing, avoiding

Table 6.1: Motor data

30 Hp, 230 V, IM.	
Voltage	230/460 V
Current	76.6/30.8 A
Number of coils	48
Number of turns/coil	18
Wire size	# 17 AWG
Coil pitch	1 - 11
Coil grouping	4
Connection	4 Δ
Stator core length	160 mm
Stator core radius	80 mm

any movement during operation. The variation of the bearing housing is measured to an accuracy of 0.01 mm with the aid of a digital dial indicator. The airgap of the motor and the center of the rotation for 0% static eccentricity (ideally aligned with the stator centre) were found by moving the rotor all the way up and all the way down reaching the stator slots and then averaging the differences read with the dial indicator. The airgap was measured to be 0.92 mm, so the maximum airgap variation allowance was set up to 0.50 mm (54% static eccentricity). A pair of bolts located at the top and bottom of the frame restricted any further displacement in order to avoid any stator to rotor rub in case of any unexpected bearing breakdown. Figures 6.5 and 6.6 show one complete new bearing housing and its components.

6.3 Data Acquisition

The data acquisition and measurement was accomplished with a National Instruments data acquisition DAQ-PCI 6024E card in a PC with LabVIEW software. This graphical programming system has been chosen for the control of data acquisition and for signal processing since it provides a powerful but simple way to interface personal

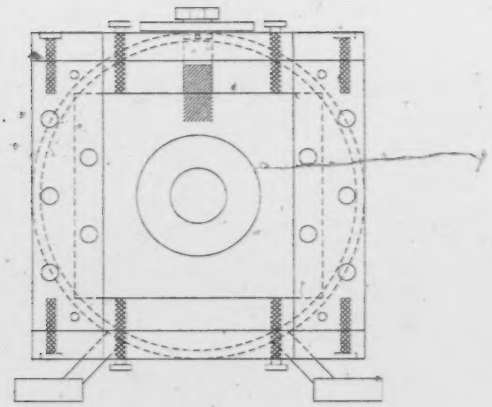

Figure 6.4: AutoCAD design of the bearing housing

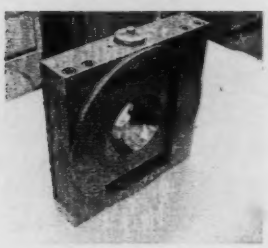

Figure 6.5: New bearing housing

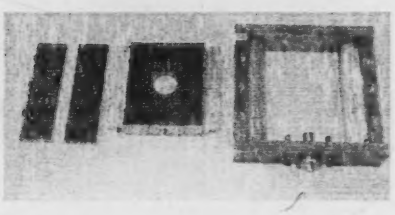

Figure 6.6: Bearing housing components

computer and measurement hardware.

Real test data were obtained with a pair of clamp-on current sensors that were placed in one of the supply cables of the three phase induction motor to measure the stator current time varying signal. The signatures of particular interest are the current signals when the motor is running at steady state under no load, half load and full load conditions. According to the acquisition arrangement scheme shown in figure 6.7, current monitoring is carried out using a fluke 80i-110s clamp on current probe for no-load and half load readings and a fluke 80i-500s clamp on current probe for full load readings. The probes are connected to the NI DAQ card and the signals were sampled and stored via Labview. The necessary signal processing approach is obtained by the required A/D conversion and the transformation of the signal to the frequency spectra which was obtained by means of the FFT and PSD. The results were saved and inspected more clearly using a separate computer program such as Matlab [42].

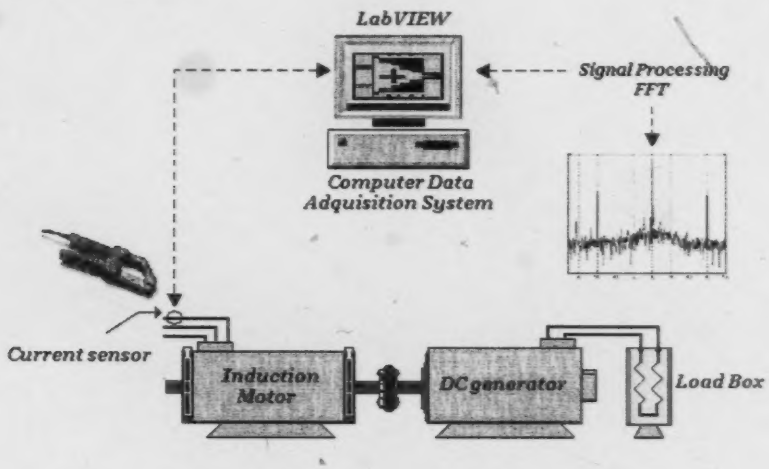

Figure 6.7: Current monitoring scheme

All measured signals were sampled at 15 KHz. The frequency range or bandwidth (f_{ran}) and the resolution (Δf) of the frequency spectrum plot depend on the sampling rate and the number of points acquired (N was chosen to be 150,000). The sampling frequency determines the frequency range. The resolution frequency is determined by the number of points acquired in the time-domain signal record. Thus, the resolution

Δf is obtained according to

$$\Delta f = \frac{f_s}{N}$$

Then, our frequency range and resolution is

$$f = \frac{f_s}{2} = 7500\ Hz \quad \Delta f = \frac{f_s}{N} = \frac{15000}{150000} = 0.1Hz$$

6.4 Labview: Monitoring Graphic Interface

Labview is a software package widely used for test, measurement and control. It has a powerful graphical development environment that allows the creation of intuitive block diagrams and front panels for signal acquisition, measurement analysis and data presentation. It provides fast development programming tools and libraries to customize any application easily.

A graphical interface for the data acquisition and measurement analysis was created in Labview for the condition monitoring of the induction machine. The graphical interface contains three screens that basically presents the real-time phase stator current waveform, supply voltage waveform, search coil induced voltage waveform and the correspondent FFT signal processing graphs. These screens are described as follows:

a) Data measurement and waveform screen

Figure 6.8 depicts the screen developed to measure the phase stator current and supply voltage signal. It displays the correspondent waveform graphs, the DC and RMS waveform values, the THD (Total Harmonic Distortion) and the high and low state amplitude levels of the signals. The user can read the magnitude of the different harmonic components of the current signal.

b) FFT signal processing screen

Figure 6.9 depicts the screen developed to visualize the stator current and supply voltage FFT frequency spectrum. The acquisition sampling frequency and the desired number of points to acquire are introduced in this screen. Also it allows the user to select a window such as Hanning, Hamming or Blackman to perform the FFT and the PSD. Furthermore, a digital filter such as Butterworth, Low-pass or High-pass

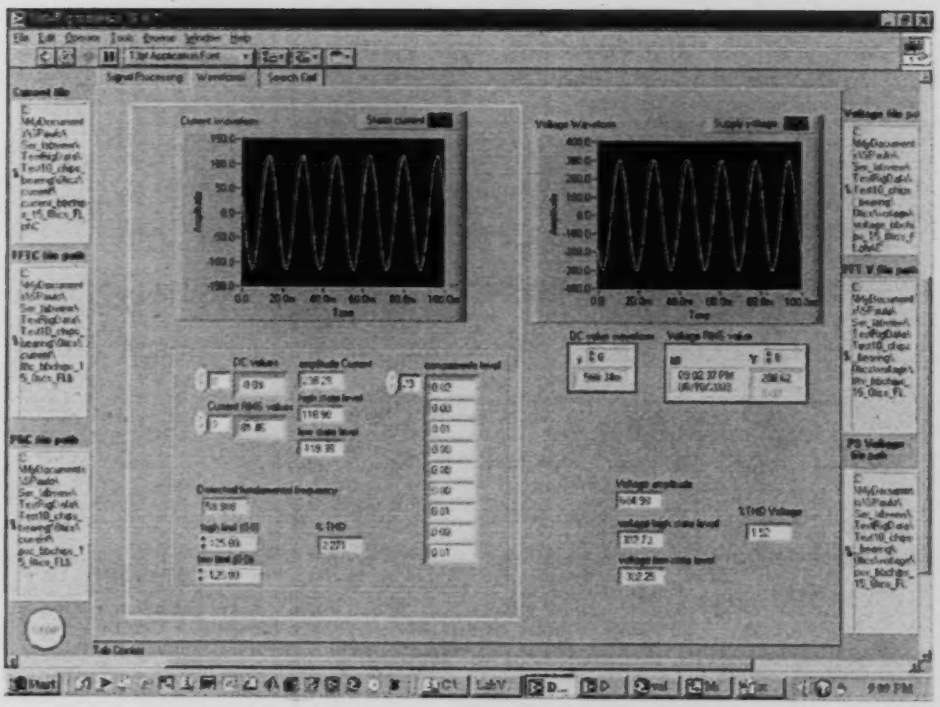

Figure 6.8: Data measurement and waveform screen

can be applied to the already transformed signal. The user may enable the averaging parameters box in order to reduce the noise content in the signal and obtain a better measurement. All data from both the current and voltage waveforms, FFT and PSD are saved in the PC as indicated in the file path box.

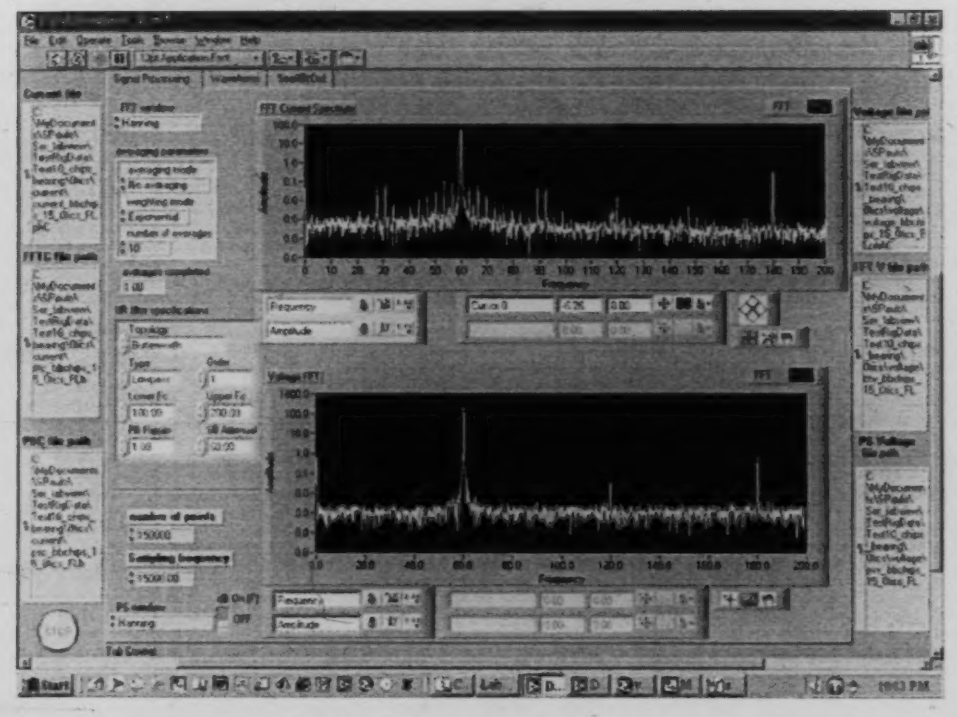

Figure 6.9: FFT signal processing screen

c) Search coil screen

A search coil screen is included in this application as shown in figure 6.10. It displays the RMS value of the induced EMF at the terminals of the search coil placed around one stator slot with a single turn. This EMF represents the airgap flux density. The high and low amplitude level of the waveform are indicated as well. The correspondent FFT signal processing graph of this waveform is presented after applying any chosen window for the FFT and the PSD calculation. In the same manner, the data from the flux waveform, FFT and PSD are saved in the PC for further analysis via the file path box.

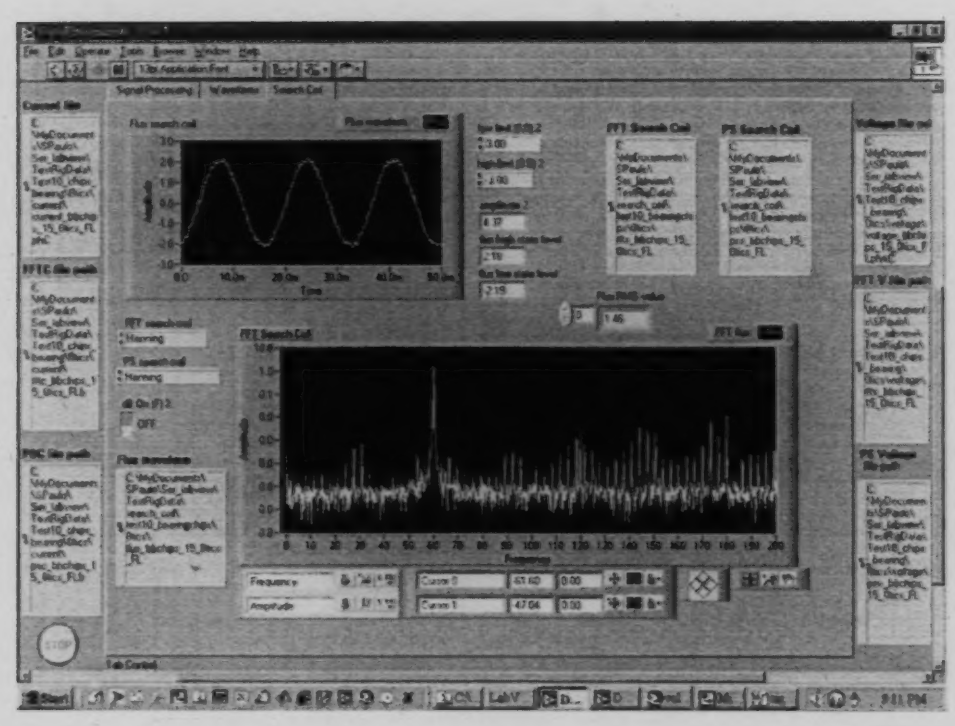

Figure 6.10: Search coil screen and signal processing

Chapter 7

Experiment Results

This chapter examines the use of stator motor current sensing for the diagnosis of static airgap eccentricity and bearing condition under no-load, half load and full-load operation conditions. The introduction of a known level of static eccentricity in the machine is done by the movable bearing housings described in chapter 6. Comparison of PSD current spectrums for a healthy motor and a motor with various levels of static eccentricity and a damaged bearing are presented. Furthermore, the frequency components that recognize this failure are shown.

7.1 Experiments Classification

The experimental data set consists of stator current signals measured from the induction motor according to three different situations: the motor in a normal-healthy operation condition, the motor with different degrees of static eccentricity and the motor with bearing damage along with various degrees of static eccentricity. All data sets contained measurements of the motor running at three different loading levels: No load, Half load and Full load. Hence, the slip (s) is a variable and the supply frequency f_e may not be necessarily exactly 60 hz. Variation on these two variables influence the value of the set of frequencies encountered in the current spectrum. The stator current waveform for each case was recorded and the FFT and PSD calculations were done by LabVIEW and stored in the PC for further analysis on Matlab. For a reliable diagnosis of the motor's condition, several sections of the current spectrum

should be observed (zoomed in) and analyzed in order to recognize a fault.

7.2 Experiments and Evaluation

In the measurements, except for a damaged bearing, all conditions were kept as constant as possible. That is, load target at half load and full load conditions were 12.5 Kw and 25 Kw respectively. Unless specified, all spectra presented are calculated and evaluated using the PSD function in LabVIEW. The amplitude of the power spectra in most of the figures are shown in the logarithmic unit decibels (dB) as defined in equation 7.1. Using this unit of measure, it is easy to view wide dynamic ranges. That is, small signal components are clearly identifiable in the presence of large ones. The decibel is a unit of ratio and is computed as follows:

$$dB = 10 \log_{10} \frac{P_m}{P_r} \tag{7.1}$$

where P_m is the measured power (PSD) and P_r is the reference power (maximum value of the PSD current spectrum). In addition, some figures show the amplitude of PSD current spectrum as the the square magnitude of motor's supply current, which follows the definition of the PSD given in chapter 2.

The parameters and conditions of the induction motor used for the experiments are presented in table 7.1

7.2.1 Healthy motor

The theoretical analysis of chapter 4 illustrates that each phase current creates air-gap flux frequencies that encompass several harmonics components in addition to the line fundamental frequency. These harmonic fluxes move relative to the stator and they should induce corresponding current harmonics in the stationary stator winding. Hence, all these frequencies should be possible to identify in the stator current spectrum.

The first experimental work was carried out running the machine with a healthy bearing and operating at no load, half load and full load conditions with ideally 0% of both static and dynamic eccentricities. A complete PSD spectrum of the healthy

Table 7.1: Motor paramenters and conditions

Condition	*Static Eccentricity (%)*	*Slip (s)*	ω_r *(Hz)*	*Rotor Slot harmonics (Hz)*		*Rotor speed (RPM)*
No Load $f_e \approx 60$ Hz	0	0.0015	29.95	1138.2	1258.2	1797.3
	22	0.001167	29.96	1138.6	1258.6	1797.9
	36	0.00133	29.96	1138.4	1258.4	1797.6
	54	0.00133	29.96	1138.4	1258.4	1797.6
Half Load $f_e \approx 60$ Hz	0	0.011083	29.67	1126.7	1246.7	1780
	22	0.012167	29.64	1125.4	1245.4	1778.1
	36	0.01175	29.65	1125.9	1245.9	1778.85
	54	0.013167	29.6	1124.2	1244.2	1776.3
Full Load $f_e \approx 60$ Hz	0	0.02683	29.2	1107.8	1227.8	1751.7
	22	0.02867	29.14	1105.6	1225.6	1748.4
	36	0.028583	29.14	1105.7	1225.7	1748.55
	54	0.03033	29.09	1103.6	1223.6	1745.4

motor running under these conditions is illustrated in figure 7.1. The PSD current spectrum is zoomed in at different frequency ranges in order to identify the frequency components of interest. Figure 7.2 demonstrates the stator current PSD spectrum in the range of low frequency components and rotor slot harmonics for no load, half load and full load conditions.

Sideband frequencies around the fundamental component are observed even with a healthy motor. Essentially they are present due to the combined effects of inherent (nominally zero) levels of static and dynamic eccentricity. These sidebands are predicted by equation 4.85. The principal or first rotor slot harmonics (RSH) are also shown and they are calculated according to equation 4.69. Similarly, the principal stator slot harmonics are depicted in figure 7.3. All these sets of frequencies are presented in table 7.2. The grid in the plots follow the frequency values presented in this table. In the spectrum, it is noted that the shift in frequency is due to the loading of the motor and the variation of the slip factor. Also, it is interesting to see that the magnitude of the sidebands decrease with loading. The reason is not clear but it may be attributed to saturation effects in the iron core. In contrast, the magnitude of the rotor slot harmonics tend to increase with load despite of having a skewed rotor in the machine. As the load increases, the current in the rotor bars increases, affecting the magnitude of these components. Hence, the magnitude of the RSH harmonic components are a function of the load.

7.2.2 Step harmonics

Another set of frequencies that should be taken into account and seen in the spectrum are the so called stator and rotor step harmonics. They are due to the traveling stator and the induced rotor magnetic field and are given by equations 4.38 and 4.97. Table 7.3 presents these frequencies. It is obvious that these components are at the same frequency for all load levels since the distribution of the MMF around the machine does not change with load. Figures 7.4 and 7.5 demonstrate the presence of both stator and rotor step harmonic components in the PSD current spectrum when operating the machine at no load, half load and full load.

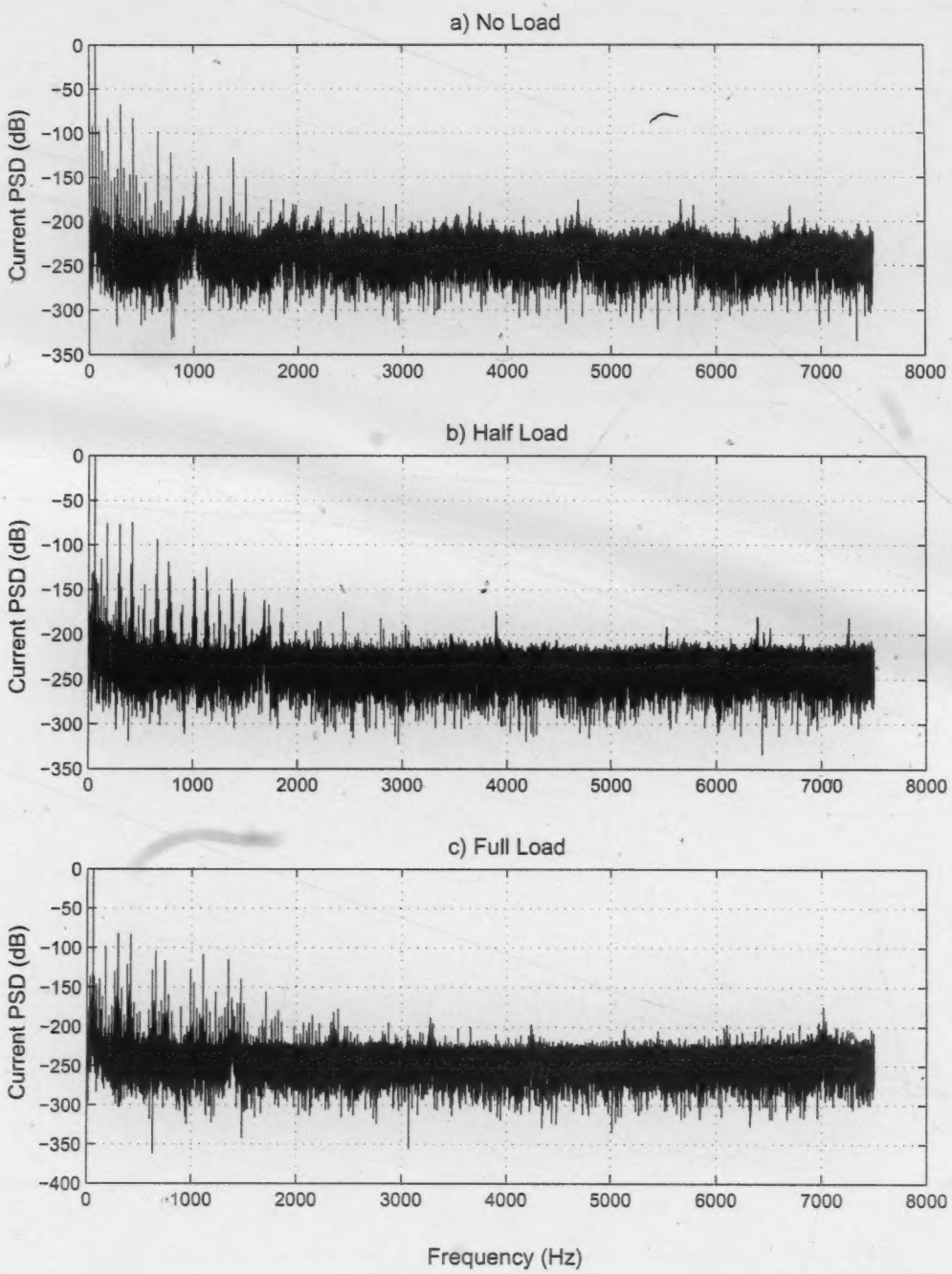

Figure 7.1: PSD current spectrum for healthy motor at different load levels

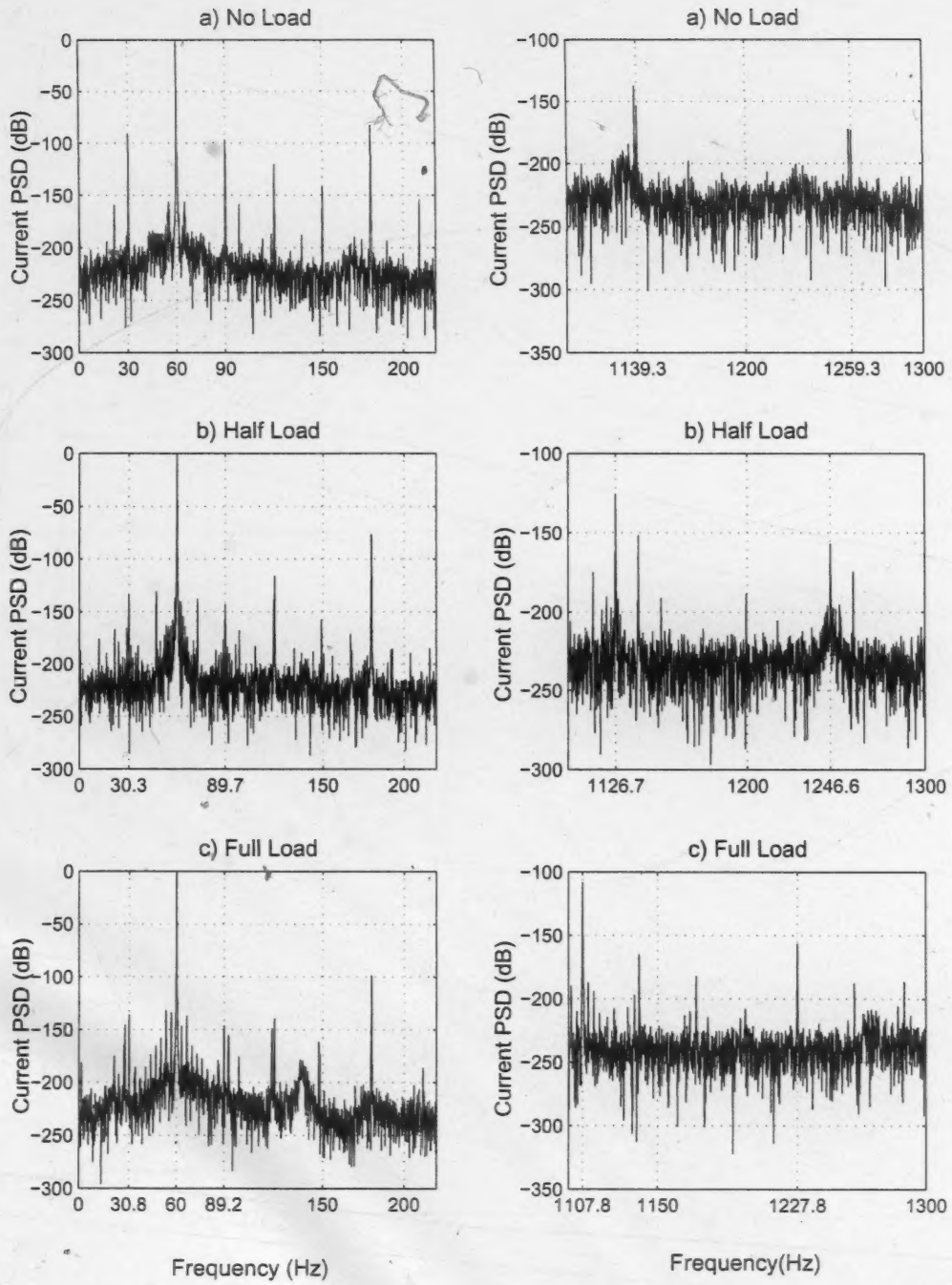

Figure 7.2: PSD Current spectrum for healthy motor at different load levels. Left, low frequency sidebands around the fundamental at $\pm\omega_r$ ($\approx$ 30 & 90 Hz). Right, rotor slot harmonics. The frequency value is indicated by the grid of the plot

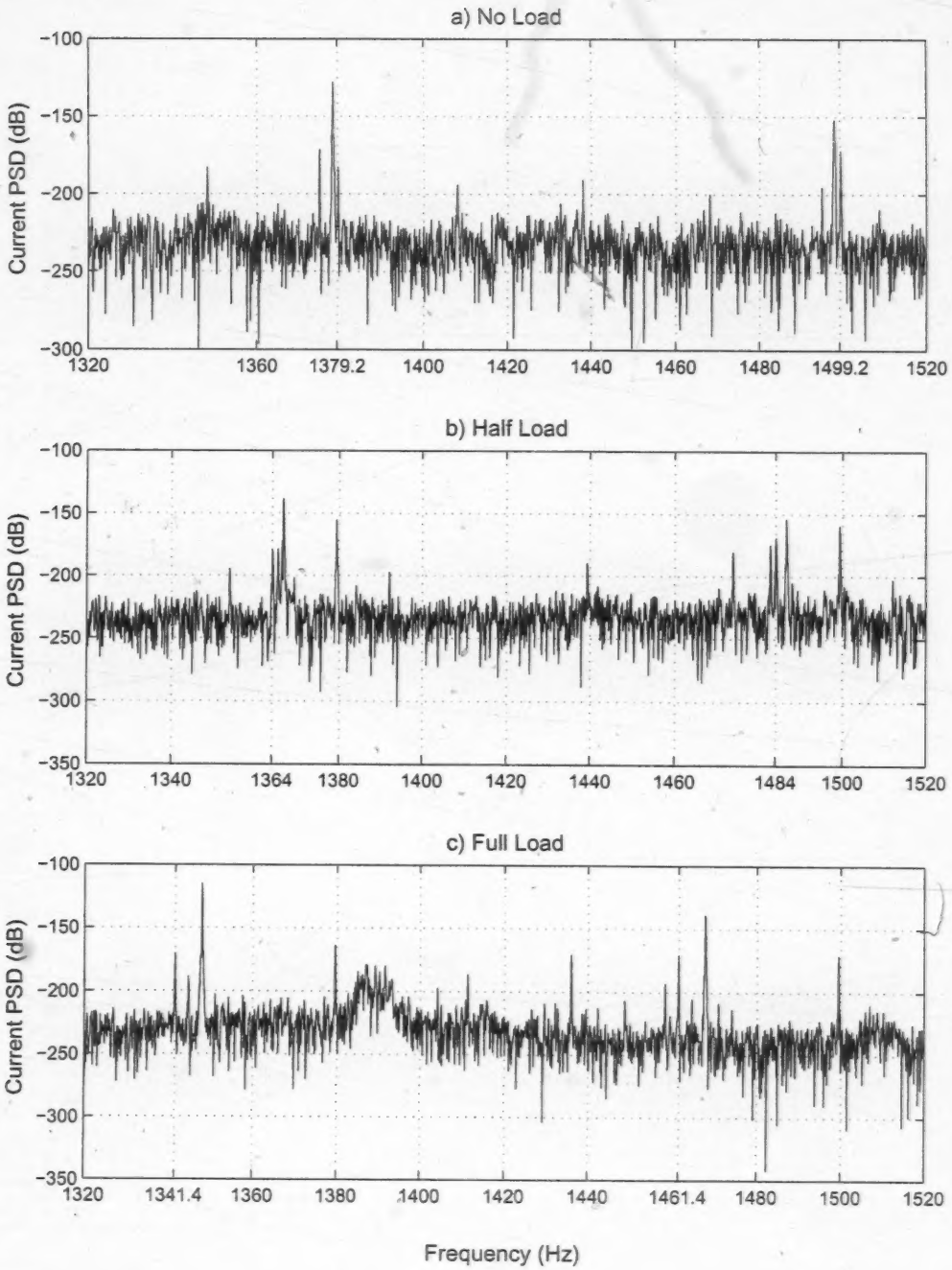

Figure 7.3: PSD Current spectrum for healthy motor at different load levels. Stator slot harmonics

Table 7.2: Frequency values for a healthy motor

Condition	*Equation* $v = 1 \quad p = 2$	*Frequencies*	
No Load	$f_{de} = f_e(1 \pm \frac{(1-s)}{p})$	30.02	89.98
RPM=1799	$f_{se} = (1-s)f_1 \pm f_e - (vp+1)\frac{(1-s)}{p}f_1$	30.02	89.98
s=0.00005	$f_{rsh} = f_e \pm kN_r\frac{(1-s)}{p}f_1$	1139.3	1259.3
	$f_{ssh} = (1-s)f_1 - f_e + (vp \pm kN_s)\frac{(1-s)}{p}f_1$	1379.2	1499.2
Half Load	$f_{de} = f_e(1 \pm \frac{(1-s)}{p})$	30.33	89.66
RPM=1780	$f_{se} = (1-s)f_1 \pm f_e - (vp+1)\frac{(1-s)}{p}f_1$	30.33	89.66
s=0.01111	$f_{rsh} = f_e \pm kN_r\frac{(1-s)}{p}f_1$	1126.6	1246.6
	$f_{ssh} = (1-s)f_1 - f_e + (vp \pm kN_s)\frac{(1-s)}{p}f_1$	1384	1484
Full Load	$f_{de} = f_e(1 \pm \frac{(1-s)}{p})$	30.80	89.20
RPM=1751.7	$f_{se} = (1-s)f_1 \pm f_e - (vp+1)\frac{(1-s)}{p}f_1$	30.80	89.20
s=0.02683	$f_{rsh} = f_e \pm kN_r\frac{(1-s)}{p}f_1$	1107.8	1227.8
	$f_{ssh} = (1-s)f_1 - f_e + (vp \pm kN_s)\frac{(1-s)}{p}f_1$	1341.4	1461.4

Table 7.3: Step harmonics frequencies (Hz)

Magnetic field	*Equation*	*Sign*	$k=1$	$k=2$	$k=3$
Stator	$f_{steph(s)} = f_1 * (6kq \pm 1)$	-	1380	2820	4260
	$q = \frac{N_s}{6p} = 4$	+	1500	2940	4380
Rotor	$f_{steph(r)} = f_1 * (kN_r \pm 1)$	-	1140	2340	3540
	$q = 1$	+	1260	2460	3660

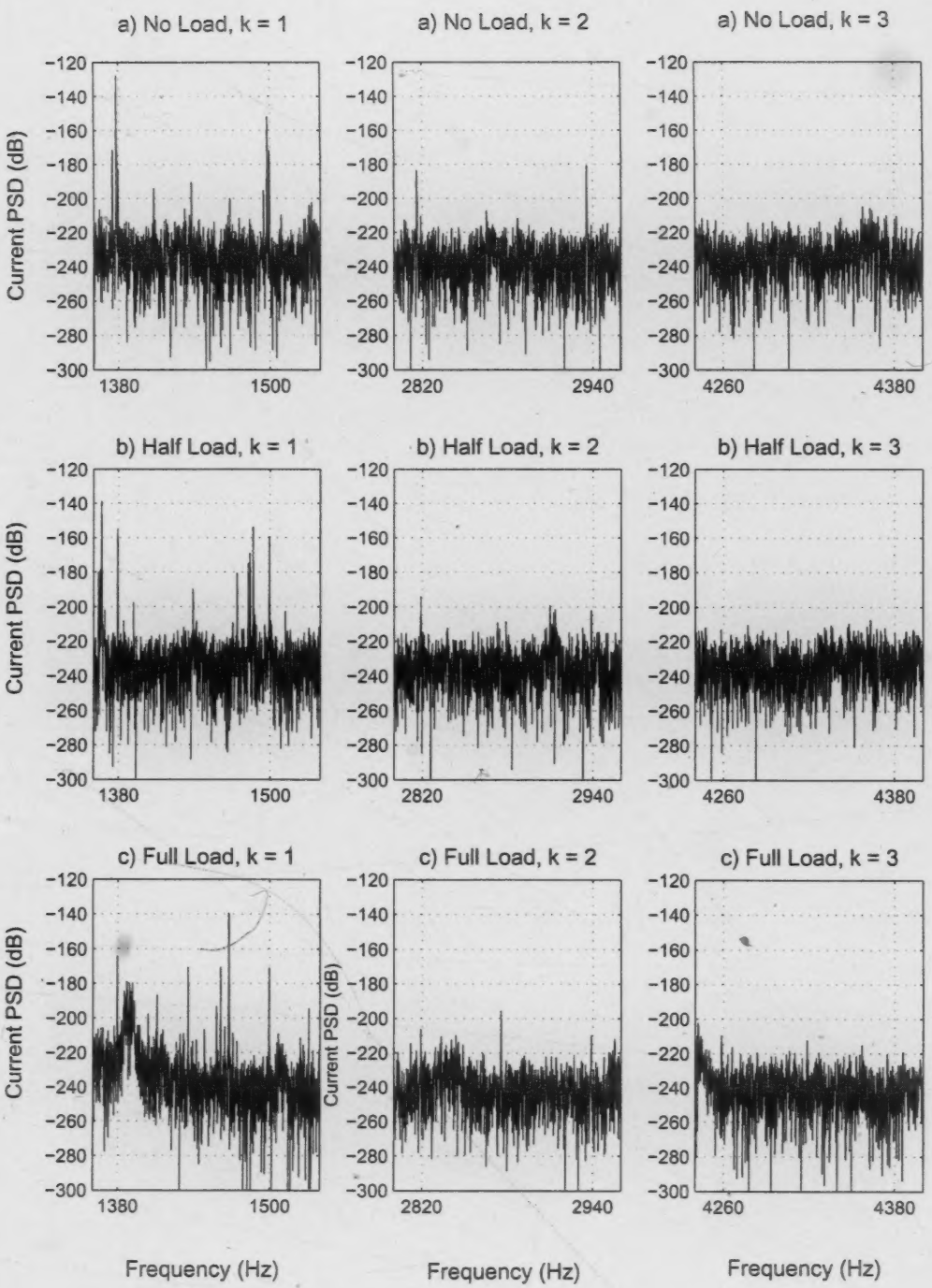

Figure 7.4: Current spectrum for healthy motor: Stator step harmonics

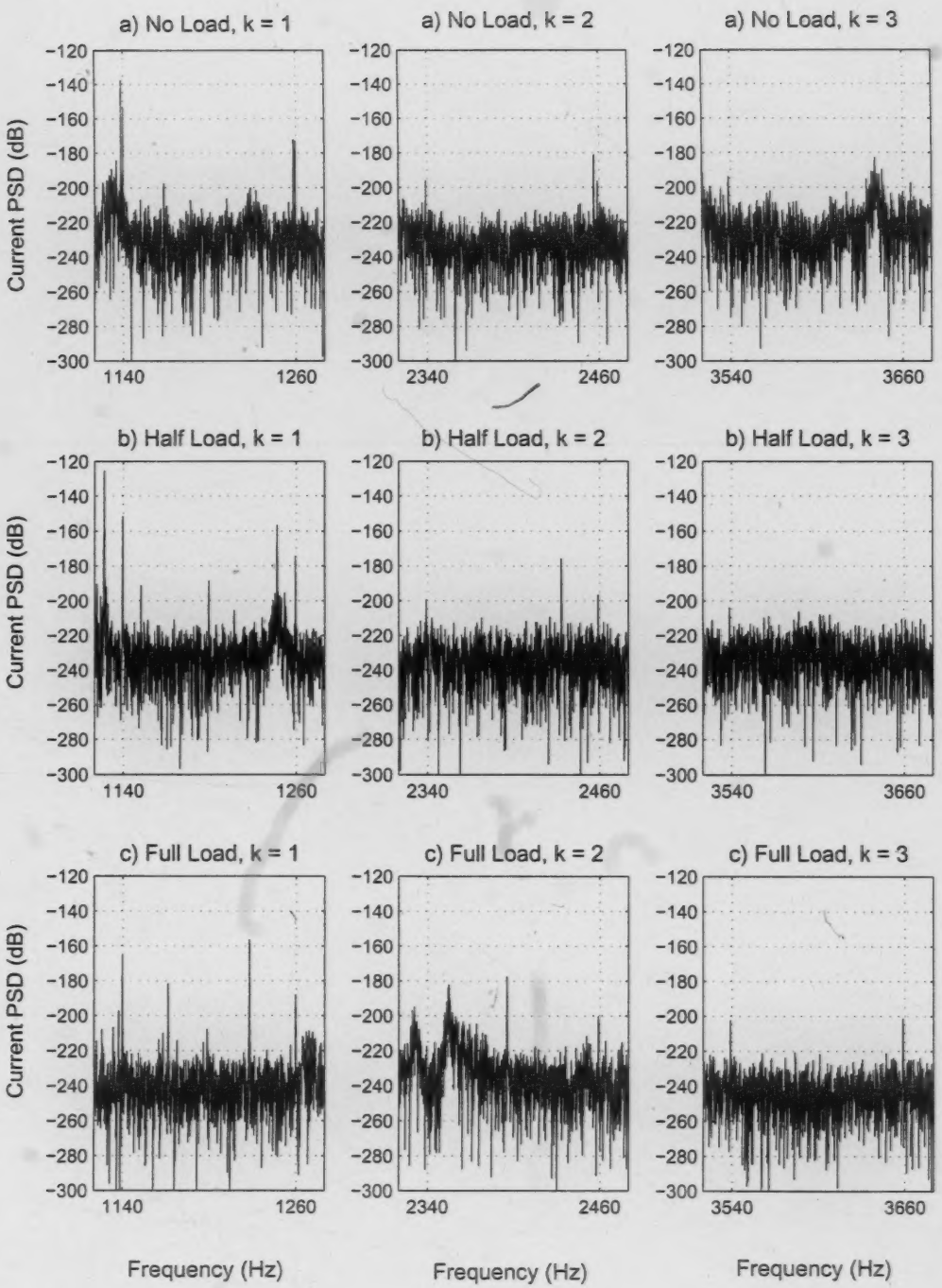

Figure 7.5: Current spectrum for healthy motor: Rotor step harmonics

7.2.3 Load effects and rotor asymmetries

Load torque variations may produce stator current components at frequencies given by equation 2.5. These components may coincide, and often overwhelm, those produced by rotor asymmetries such as broken bars or eccentricity. In the experiments, various low frequency components around the fundamental can be easily distinguished when the motor is running at full load. This is observed in figure 7.6.

Table 7.4 presents these frequency components obtained from equations 2.1, 2.2 and 2.5 that may indicate rotor broken bars and load variation effects respectively. Figure 7.6 a) and b) illustrates the apparition of these components in the PSD current spectrum of the healthy motor running at full load. It is interesting to note that multiples of these frequencies will also appear around the 300 Hz component and 420 Hz component as it is shown in figure 7.6 c).

However, it is known by visual inspection that the motor does not have any severe damage in the rotor. Hence, the presence of these components may be due to either inherent levels of dynamic and static eccentricity or small load oscillations and their magnitudes does not change when different degrees of eccentricity is introduced in the motor (except for those affected by static or dynamic eccentricity). Furthermore, although the frequencies given by equation 2.2 may indicate the presence of broken bars, one can determine from section 2.2.1 that no broken bars exist in the rotor since the magnitude of the LSB1 (k=1) component is $\leq$ 60 dB relative to the fundamental.

Table 7.4: Rotor asymmetries and load effect harmonics

k	$F_{rotor\ asymmetry}$				$F_{load\ effects}$	
	$f_k = f_e(\frac{k}{p}(1-s) \pm s)$		$f_b = f_e(1 \pm 2ks)$		$f_{load} = f_e[1 \pm k\frac{(1-s)}{p}]$	
1	30.80	27.58	63.22	56.78	89.19	30.80
2	60.00	56.78	66.44	53.56	118.39	1.61
3	89.19	85.97	69.66	50.34	147.58	-27.58
4	118.39	115.17	72.88	47.12	176.78	-56.78
5	147.58	144.36	76.10	43.90	205.97	-85.97

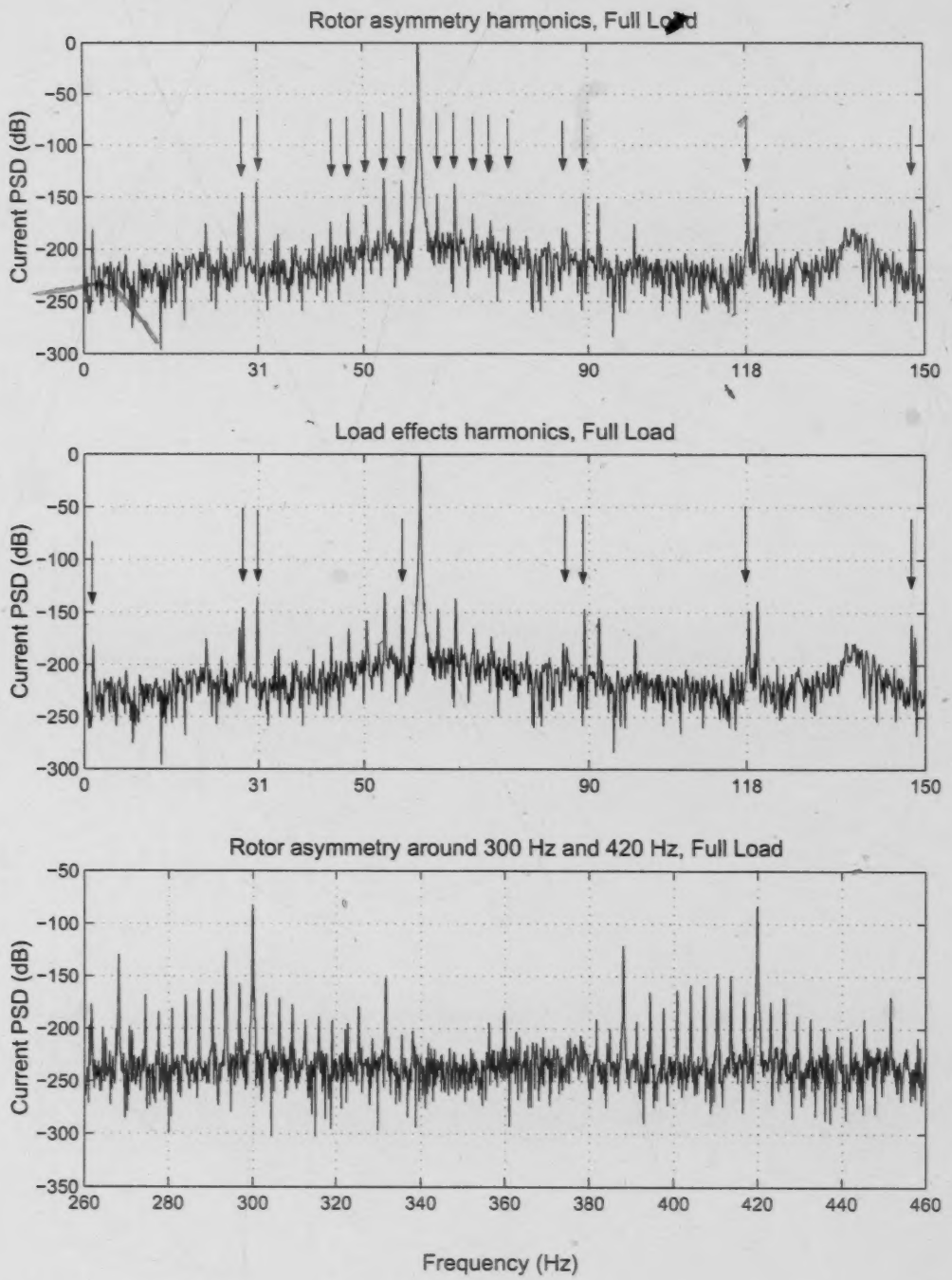

Figure 7.6: PSD current spectrum for a healthy motor: Rotor asymmetry and load effects harmonics

7.2.4 Rotor slot harmonics (RSH)

As illustrated in figure 7.1, the current spectrum of the motor will contain a great variety of different set of frequencies of interest. One of the most prominent frequencies identifiable in the spectrum are the rotor slot harmonics. Equation 7.2 is utilized to determined the set of frequencies due to the rotor slot harmonics.

$$f_{rsh} = 60(n_t \pm kN_r\frac{(1-s)}{p}) \tag{7.2}$$

where $n_t = 1, 3, 5, \ldots$ is the time harmonic order and $k = 1, 2, 3, \ldots$ is an integer value. Table 7.5 summarizes some of the rotor slot harmonics obtained from equation 7.2 and figures 7.7, 7.8 and 7.9 indicate the presence of them in the PSD current spectrum. It is observed that for each time harmonic order, a set of frequencies for each integer k are generated. The presence of the RSH in the current spectrum and their change in magnitude are utilized to diagnose, identify and determined a static eccentricity condition in the motor. The stator slot harmonics, however, do not present components of interest with other combinations of n and k and only the fundamental component is identified in the current spectrum as already shown in figure 7.3.

7.3 Faulty Motor

The current condition monitoring scheme used in the experimental testing aim to recognize the fault introduced in the motor by looking at the variations in magnitude of the harmonics given by low frequency components of equation 4.85 and rotor slot harmonics from equation 7.2 when different degrees of static eccentricity are introduced. The following results are obtained with the machine running at no load, half load and full load conditions and different degrees of static eccentricity.

7.3.1 Airgap eccentricity

When the airgap of the machine is eccentric due to static, dynamic or mixed eccentricity, the airgap flux density becomes non-uniform and a unidirectional force acts between the stator and rotor, increasing eccentricity. As discussed in section 3.2 both

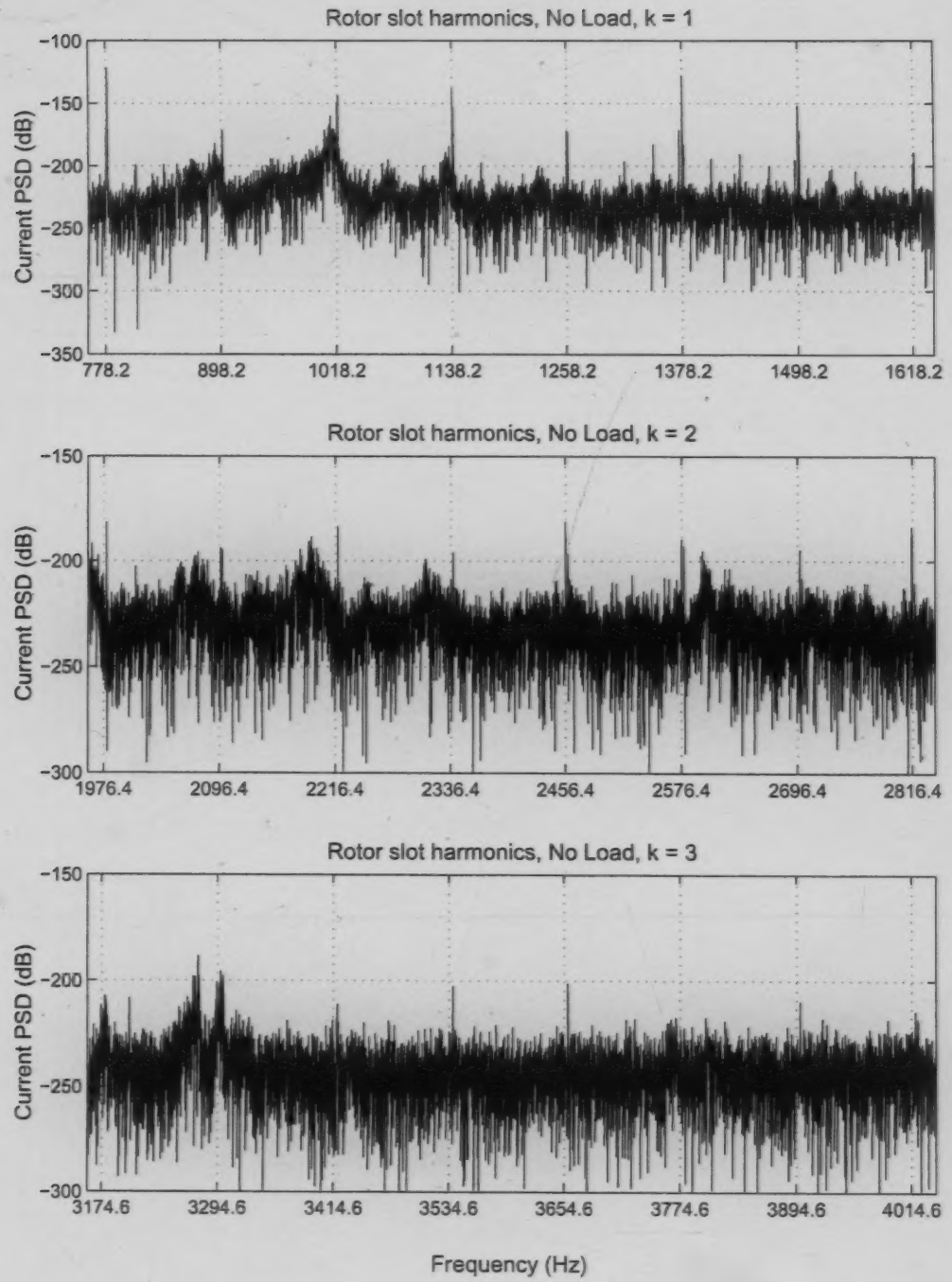

Figure 7.7: Rotor slot frequency components in the PSD current spectrum at No Load

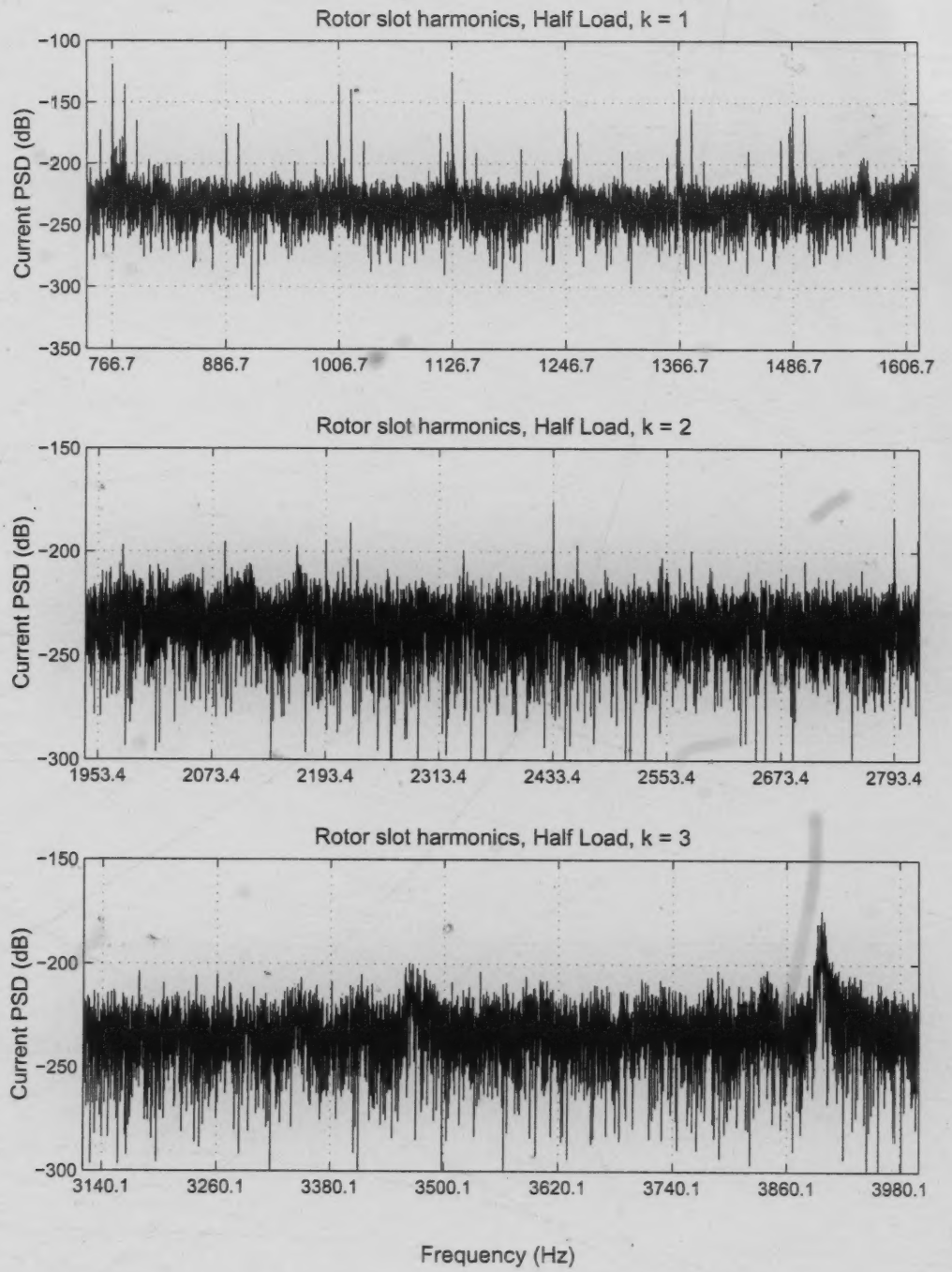

Figure 7.8: Rotor slot frequency components in the current spectrum at Half Load

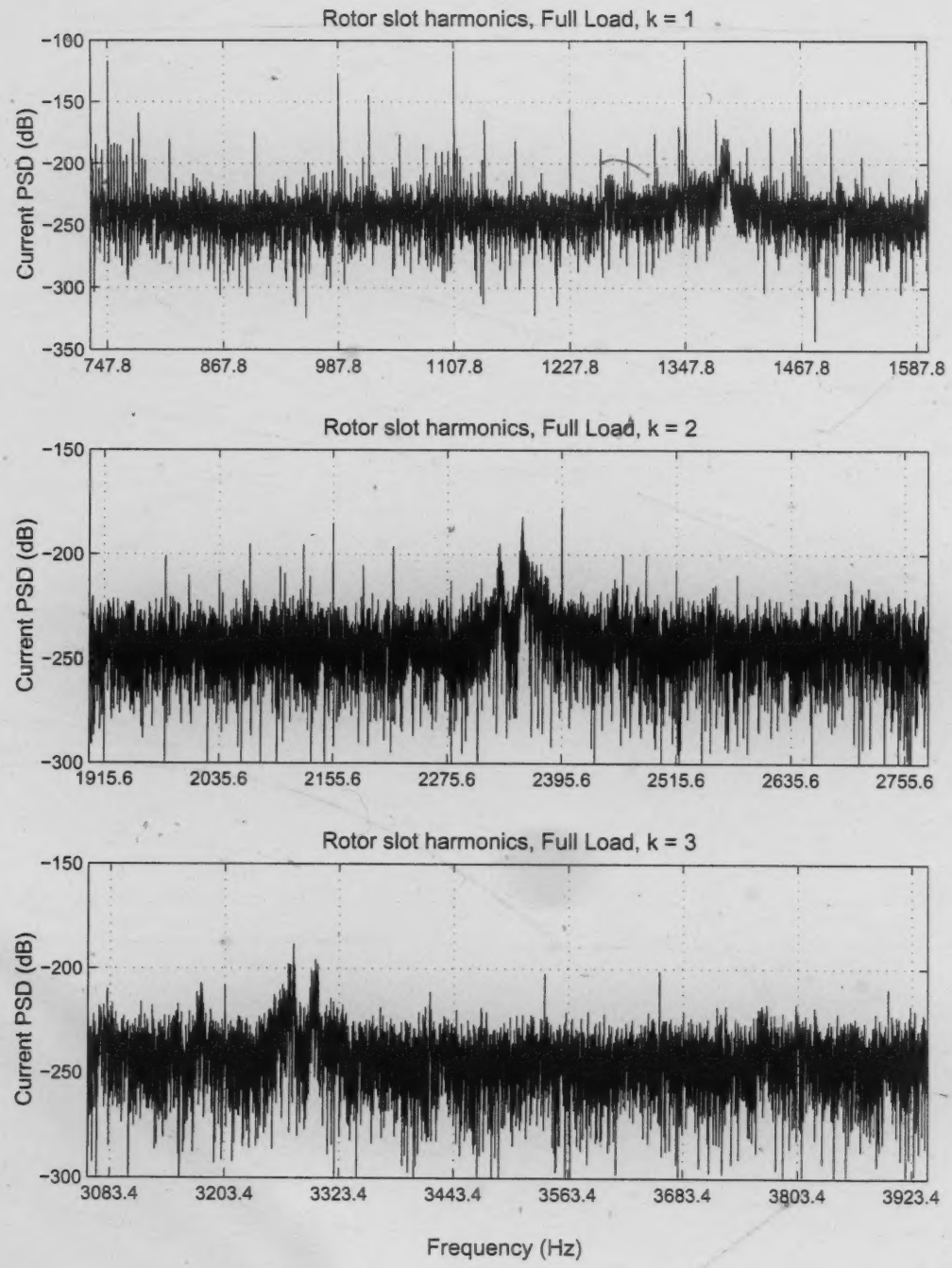

Figure 7.9: Rotor slot frequency components in the current spectrum at Full Load

Table 7.5: Rotor slot harmonic frequencies

		$f_{rsh} = 60(n_t \pm kN_r\frac{(1-s)}{p})$							
Condition	k	time = 1		3		5		7	
		-	+	-	+	-	+	-	+
No Load	1	-1138.2	1258.2	-1018.2	1378.2	-898.2	1498.2	-778.2	1618.2
	2	-2336.4	2456.4	-2216.4	2576.4	-2096.4	2696.4	-1976.4	2816.4
	3	-3534.6	3654.6	-3414.6	3774.6	-3294.6	3894.6	-3174.6	4014.6
Half Load	1	-1126.7	1246.7	-1006.7	1366.7	-886.7	1486.7	-766.7	1606.7
	2	-2313.4	2433.4	-2193.4	2553.4	-2073.4	2673.4	-1953.4	2793.4
	3	-3500.1	3620.1	-3380.1	3740.1	-3260.1	3860.1	-3140.1	3980.1
Full Load	1	-1107.8	1227.8	-987.8	1347.8	-867.8	1467.8	-747.8	1587.8
	2	-2275.6	2395.6	-2155.6	2515.6	-2035.6	2635.6	-1915.6	2755.6
	3	-3443.4	3563.4	-3323.4	3683.4	-3203.4	3803.4	-3083.4	3923.4

types of eccentricity cause excessive stress on the machine and greatly increase bearing wear. Also, if not detected on time, a potential rotor to stator rub may occur with consequential damage to the core, windings and rotor cage, leading to insulation failure of the stator winding or breaking of the rotor squirrel-cage bars or end rings.

7.3.2 Introduction of static eccentricity by rotor radial movement

Thomson [8] and Toliyat [43] have shown that the presence of any eccentricity on the machine can be identified by looking at the change of magnitude of the sidebands around the fundamental time-current component (60 hz) given by equation 4.85. Certainly, these components are seen in the current spectrum for a healthy motor (figure 7.6) with inherent levels of eccentricity. The problem is to differentiate which one is most prominent and when they are highly excessive. Therefore, low frequency components given by the sidebands at $\pm\omega_r$ around the fundamental and high frequency components given by the rotor slot harmonics provide an opportunity to analyze,

recognize and detect any eccentric abnormality.

A low inherent level of dynamic eccentricity such as 5% is assumed in the rotor since the motor has a record of few hours of operation, performing a stressless task. Static eccentricity is introduced in the system by means of the movable bearing housings. Different levels of static eccentricity can be reached, but the experiments concentrated in introducing mainly four percentage levels of static eccentricity: 0%, 22%, 36%, and 54%.

In condition monitoring of motors, the relative changes in the measurement results are used to indicate the progression of any failure. The healthy current spectrum of the motor is utilized as the reference point and indicator of any developing failure. Therefore, it could be stated that any change in magnitude of the harmonic components of interest from the base-reference, either an increase or decrease, might indicate the advance of the failure.

7.3.3 Low frequency harmonics

Thomson [25] and Toliyat [43] have shown that in the presence of any mixed form of eccentricity, certain low frequency components given by equation 7.3 will also be present in the stator current spectrum of a three phase induction motor.

$$f_{lf} = n\omega \pm k\omega_r \tag{7.3}$$

where ω_r = rotor angular speed, n = time harmonic order $(1, 3, 5, \ldots)$ and $k = 1, 2, 3, \ldots$. In chapter 6, simulations have shown that static eccentricity can be identified by looking at the frequency components given by equation 7.3. The most dominant of these frequency components are the sidebands given by equation 7.3 with $n = 1$ and $k = 1$. However, low-frequency components for $k > 1$ and $n > 1$ can also be identified in the current spectrum and are indicative of an increase of static eccentricity. Table 7.6 present the frequency components that are found in the current spectrum with the machine running at no-load, half load and full load and at 54% static eccentricity. The frequency components at 0, 22% and 36% are not displayed in the table since they are distinguished in the PSD current spectrum relative to the ones at 54% static eccentricity. Figures 7.10, 7.11, 7.12 compare the magnitude of

these frequency components when the machine is running at no load, half load and full load and with 0%, 22%, 36% and 54% static eccentricity for $n = 1$ and different values of k.

Table 7.6: Frequencies components at $n\omega \pm k\omega_r$

Condition	k	time = 1		3	
		-	+	-	+
No Load	1	30.04	89.96	150.04	209.96
	2	0.08	119.92	120.08	239.92
	3	-29.88	149.88	90.12	269.88
	4	-59.84	179.84	60.16	299.84
	5	-89.8	209.8	30.2	329.8
Half Load	1	30.395	89.605	150.395	209.605
	2	0.79	119.21	120.79	239.21
	3	-28.815	148.815	91.185	268.815
	4	-58.42	178.42	61.58	298.42
	5	-88.025	208.025	31.975	328.025
Full Load	1	30.91	89.09	150.91	209.09
	2	1.82	118.18	121.82	238.18
	3	-27.27	147.27	92.73	267.27
	4	-56.36	176.36	63.64	296.36
	5	-85.45	205.45	34.55	325.45

It is observed that the presence of static eccentricity in the motor affects the magnitude of some of the components presented in table 7.6. Congruent with Dorrell et al [44], most of the magnitudes of these harmonics increase with an increase in eccentricity, but some of them decrease as seen when the machine is running at no load. A decrease in magnitude of the low frequency sidebands can be observed when there is nominal zero static eccentricity at no load conditions. However, at full load conditions and with some levels of static eccentricity, these components have increased in magnitude compared to a normal healthy condition. Clearly, the sidebands given

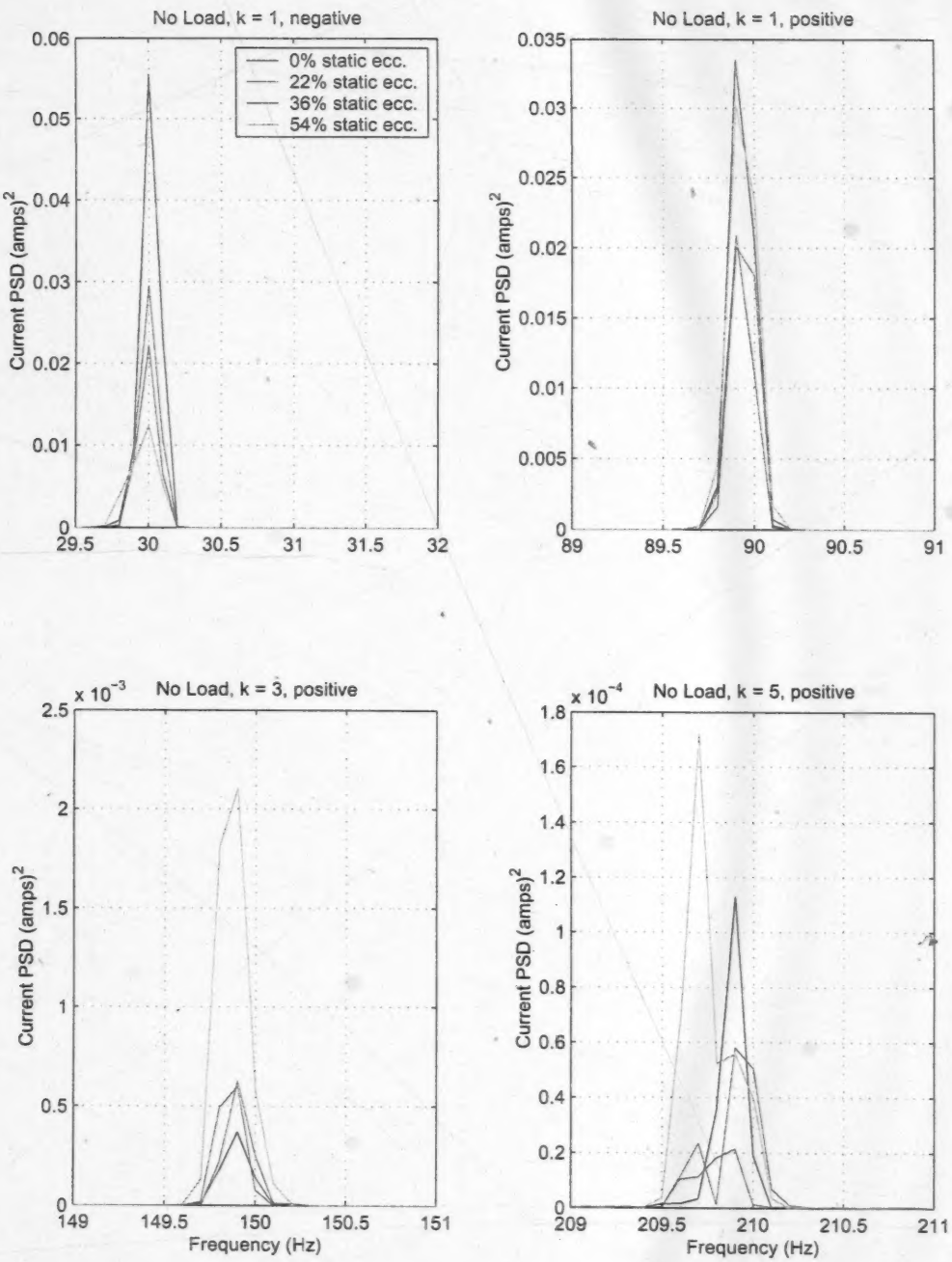

Figure 7.10: Low frequency components at 0%, 22%, 36% and 54% static eccentricity. No load with $n = 1$ and $k = 1, 3, 5$

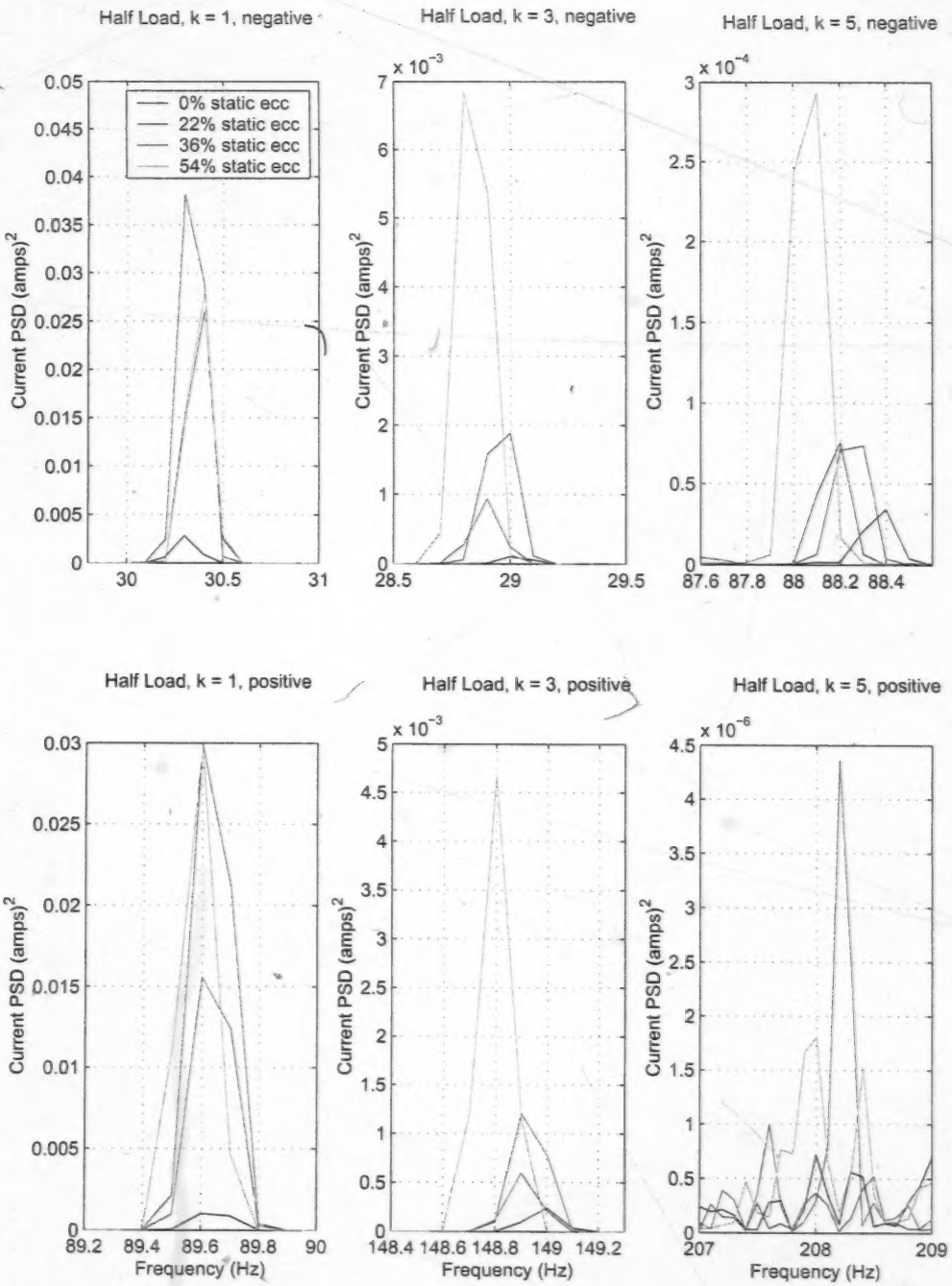

Figure 7.11: Low frequency components at 0%, 22%, 36% and 54% static eccentricity. Half load with $n = 1$ and $k = 1, 3, 5$

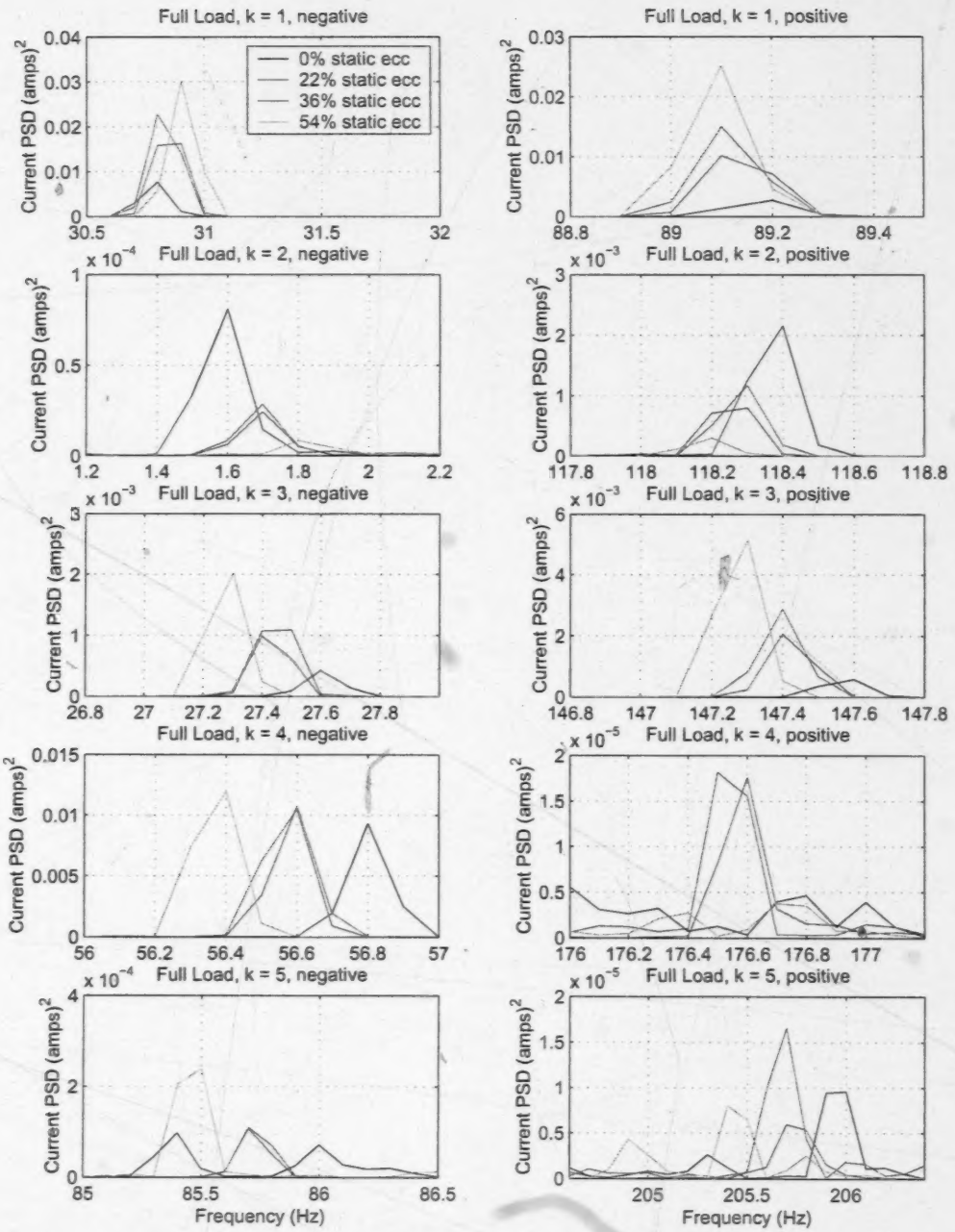
Full Load, k = 1, negative
Full Load, k = 1, positive
0% static ecc
22% static ecc
36% static ecc
54% static ecc
Current PSD (amps)^2
Full Load, k = 2, negative
Full Load, k = 2, positive
Full Load, k = 3, negative
Full Load, k = 3, positive
Full Load, k = 4, negative
Full Load, k = 4, positive
Full Load, k = 5, negative
Full Load, k = 5, positive
Frequency (Hz)

Figure 7.12: Low frequency components at 0%, 22%, 36% and 54% static eccentricity. Full load with $n = 1$ and $k = 1, 2, 3, 4, 5$

by $(\omega \pm \omega_r)$ show the most significant changes in the spectrum. Thus, having the healthy motor current spectrum as a reference, the magnitude of the sidebands when a 54% of eccentricity is introduced, have increased by 12.8 dB and 21.5 dB respectively (31 hz and 89 Hz).

Frequency components given by equation 7.3 with $n = 3$ and $k = 1, 3, 5$ are also present in the current spectrum and their respective magnitudes are also affected with a high percent of static eccentricity. Figures 7.13 and 7.14 depict these components when running the machine at half load and full load with different degrees of static eccentricity. No load frequency components for $n = 3$ and $k = 1, 3, 5$ are not presented since they are obscured by those components given with $n = 1$ and multiples of the fundamental.

Figure 7.15 shows the variation in magnitude of the low frequency components obtained from equation 7.3 with $k = 1, 2, 3$. The same components can be obtained from equation 4.90, which are related to static eccentricity. These components are compared when the motor is running at no load, half load and full load conditions and with different percentages of static eccentricity. It is clear that the sidebands at $\pm\omega_r$ around the fundamental, present the most significant effects when the motor is running at full load. The magnitude of these sideband components increase with eccentricity, although these same components tend to decrease in magnitude at no load conditions. Similarly, frequency components obtained from equation 7.3 with $k = 3$ increase in magnitude when static eccentricity also increases with the motor running at full load and half load conditions. The no load components are diminished and obscured by other components. Contrary to this, the frequency components obtained from equation 7.3 with $k = 2$ tend to decrease in magnitude when static eccentricity increase and running the motor at full load. These phenomenon may be attributed to saturation effects.

In summary, the presence of a high percent of static eccentricity in the machine can be recognized and distinguished from a healthy machine by looking at the low frequency components of the PSD current spectrum obtained from equation 7.3. Simulation results are in close agreement with the experimental results obtained for the low frequency components as shown in chapter 5 in figures 5.3 and 5.4.

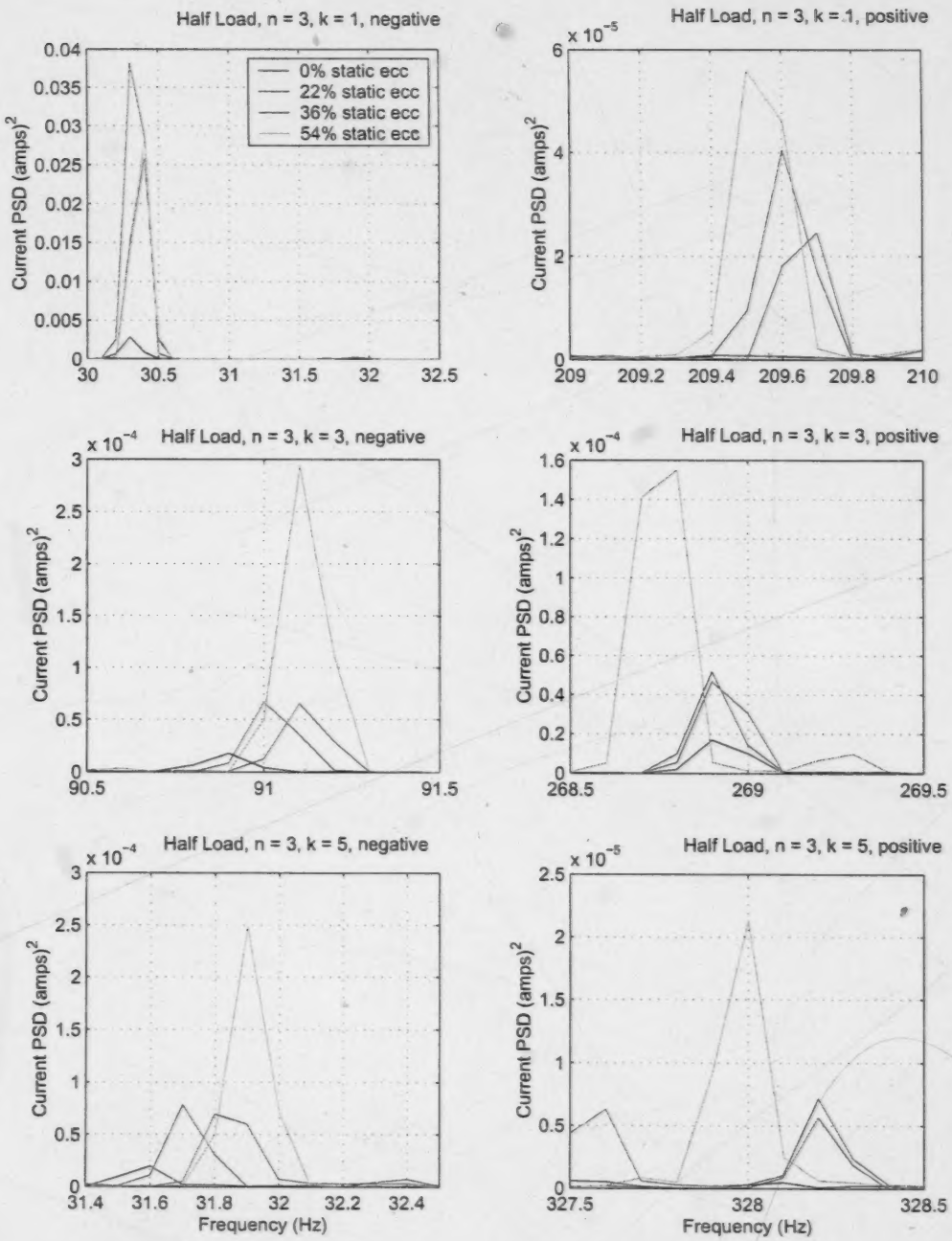
Half Load, n = 3, k = 1, negative
0% static ecc
22% static ecc
36% static ecc
54% static ecc
Current PSD (amps)^2
Half Load, n = 3, k = 1, positive
x 10^-5
Half Load, n = 3, k = 3, negative
x 10^-4
Half Load, n = 3, k = 3, positive
x 10^-4
Half Load, n = 3, k = 5, negative
x 10^-4
Half Load, n = 3, k = 5, positive
x 10^-5
Frequency (Hz)

Figure 7.13: Low frequency components at 0%, 22%, 36% and 54% static eccentricity. Half load with $n = 3$ and $k = 1, 3, 5$

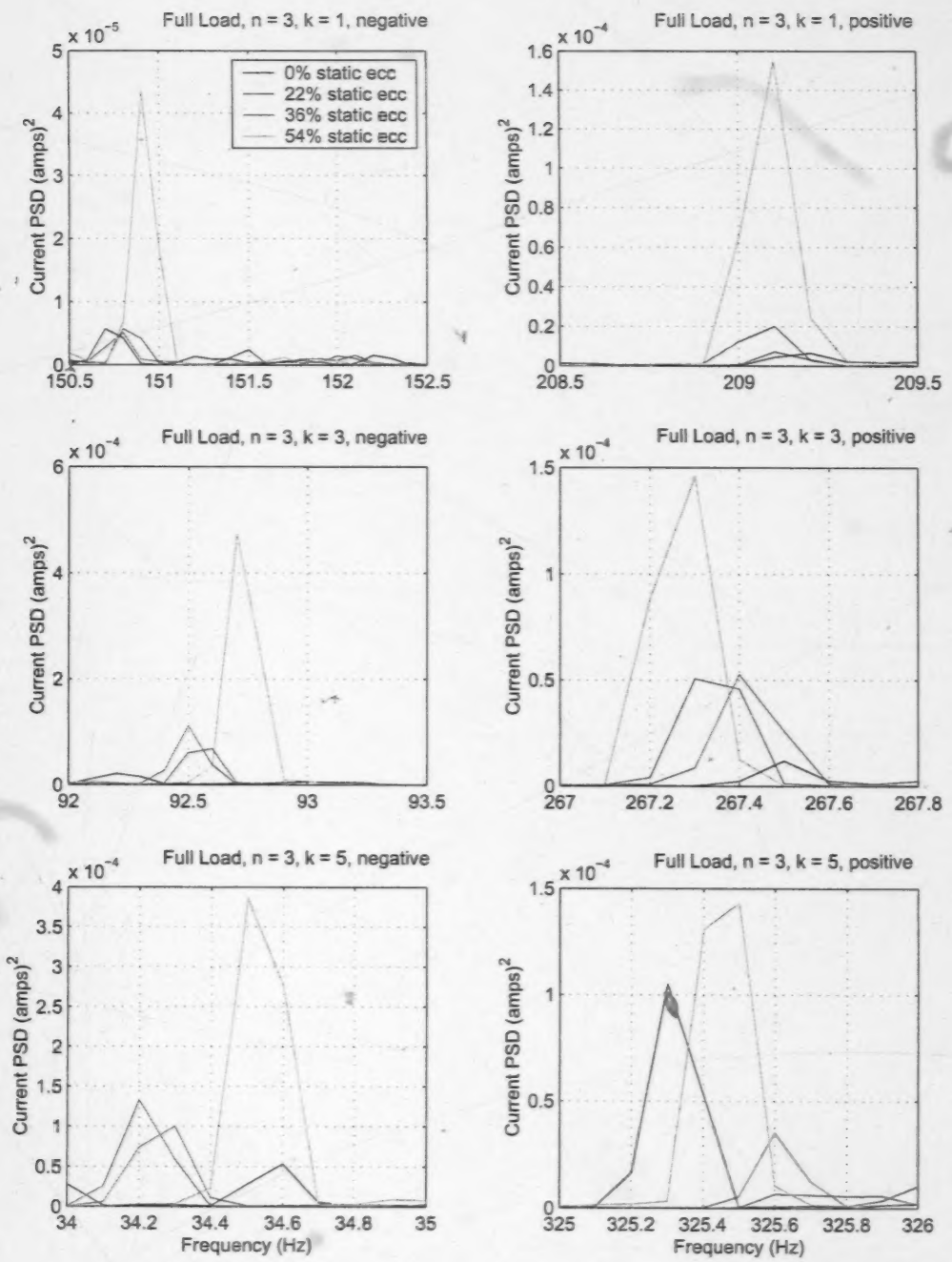
Full Load, n = 3, k = 1, negative
x 10^-5
0% static ecc
22% static ecc
36% static ecc
54% static ecc
Current PSD (amps)^2
Full Load, n = 3, k = 1, positive
x 10^-4
Full Load, n = 3, k = 3, negative
Full Load, n = 3, k = 3, positive
Full Load, n = 3, k = 5, negative
Full Load, n = 3, k = 5, positive
Frequency (Hz)

Figure 7.14: Low frequency components at 0%, 22%, 36% and 54% static eccentricity. Full load with $n = 3$ and $k = 1, 3, 5$

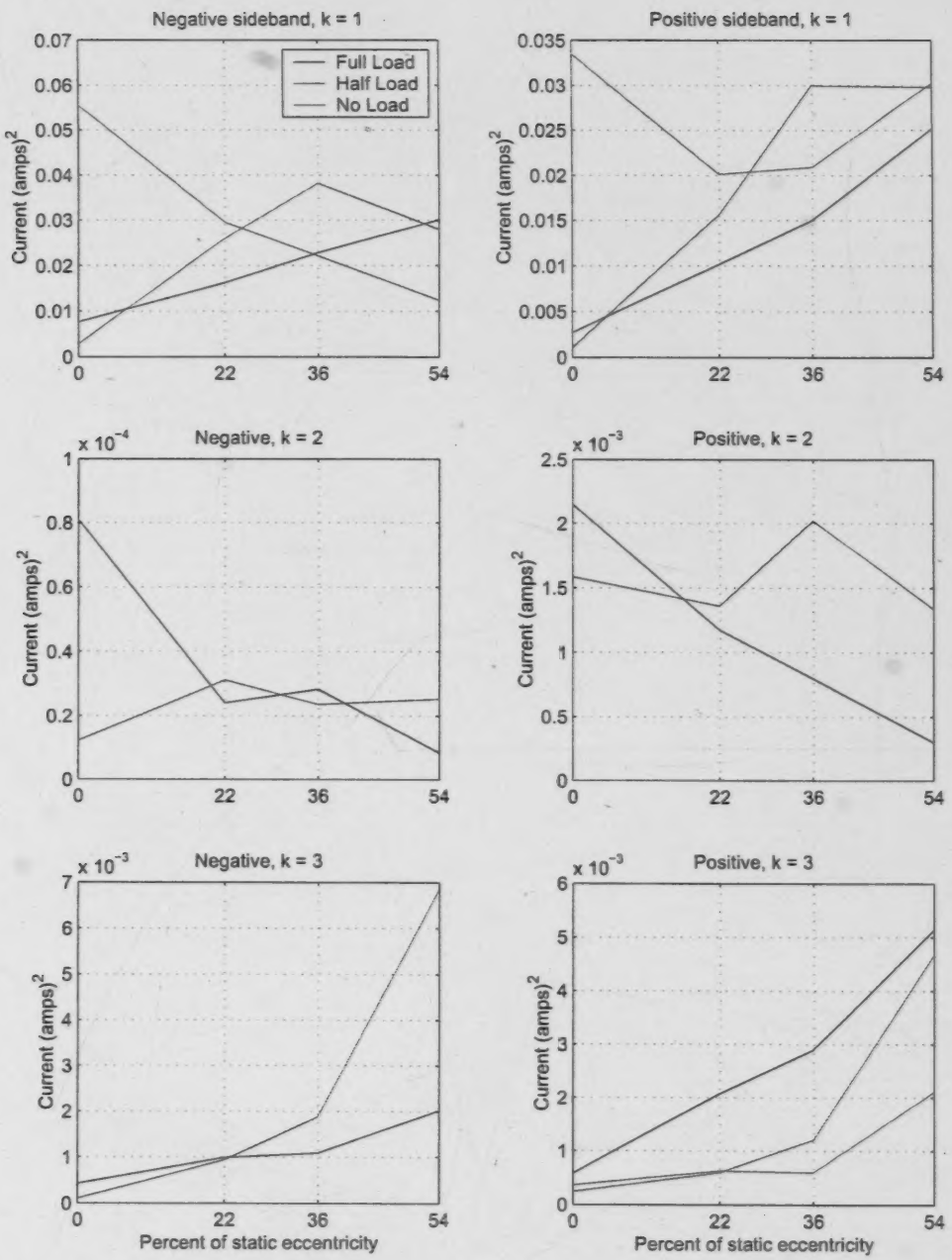

Figure 7.15: Variation in magnitude of the low frequency components obtained from $\omega \pm k\omega_r$ when the motor is running at no load, half load and full load conditions and with different percentages of static eccentricity

7.3.4 Rotor slot harmonics

Simulations results indicate that rotor eccentricity in the motor generates an increase of magnitude of the rotor slot harmonics, their multiples and the apparition of sidebands at $\pm\omega_r$ around them. The terms, rotor slot harmonics RSH_n and RSH_p, are used to define the negative and positive components respectively. Their multiples are defined as the first, second, third, etc. rotor slot harmonics RSH_n or RSH_p. Thomson et al [25] has predicted the presence of airgap eccentricity problems in large machines (1944 hp) by looking at the change in magnitude of the RSH and their sidebands at $\pm\omega_r$. Similarly, Nandi et al [43] obtained the same results while working with a 3hp induction motor. Hence, it is expected a similar effect for the machine used in the experiments (25Hp). Figures 7.16, 7.17 and 7.18 depict the first $RSH_{n,p}$ and their sidebands at $\pm\omega_r$ when the machine is running at no load, half load and full load respectively and with 0%, 22%, 36% and 54% static eccentricity.

In general, the magnitudes of the rotor slot harmonics are affected with the introduction of static eccentricity. The increase of magnitude in the sidebands of the RSH also becomes notable at different degrees of eccentricity and different load levels. Figure 7.19 shows the variation in magnitude of the first RSH_n, RSH_p and their sidebands when running the machine at no load, half load and full load conditions and with different percentages of static eccentricity. It can be observed that the first RSH_n and its sidebands present the most significant effects when running the machine at no load, half load and full load. Clearly, the magnitude of these components increase when static eccentricity is increased. Contrary, the change in magnitude of the first RSH_p does not follow any logical relationship, although the positive sideband at half load and full load conditions increase in magnitude.

Therefore, it can be stated that an increase of magnitude of the first RSH_n and its sidebands are indicators of the presence of static eccentricity in the motor.

7.3.5 RSH with time harmonics

A great variety of frequency components can be obtained from equation 7.2 with different values of n and k. Most of them are seen in the PSD current spectrum but few of them are affected when introducing different degrees of static eccentricity.

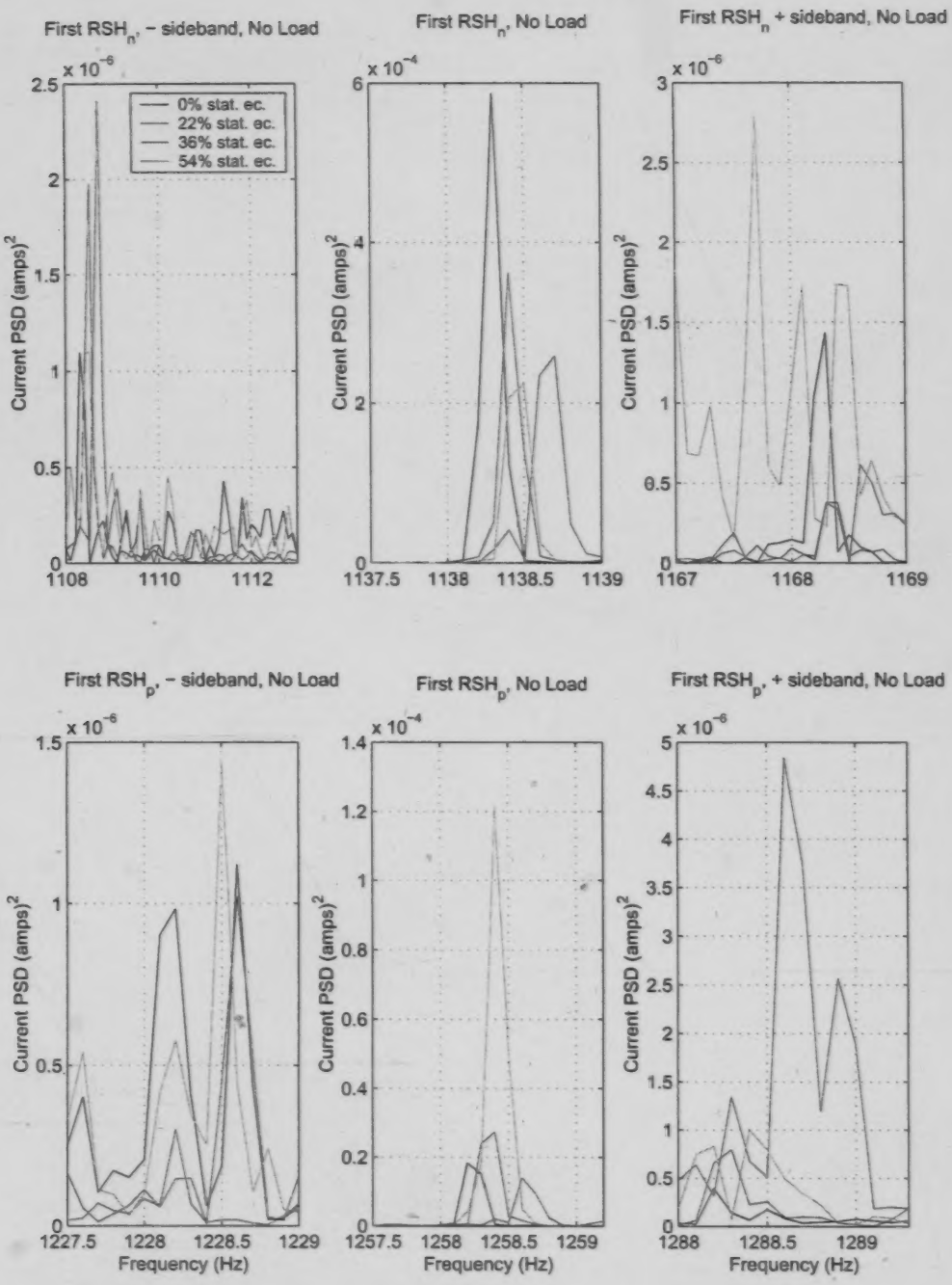
First RSH$_n$, − sideband, No Load
First RSH$_n$, No Load
First RSH$_n$ + sideband, No Load
First RSH$_p$, − sideband, No Load
First RSH$_p$, No Load
First RSH$_p$, + sideband, No Load
0% stat. ec.
22% stat. ec.
36% stat. ec.
54% stat. ec.
Current PSD (amps)^2
Frequency (Hz)

Figure 7.16: First RSH and sidebands at No Load

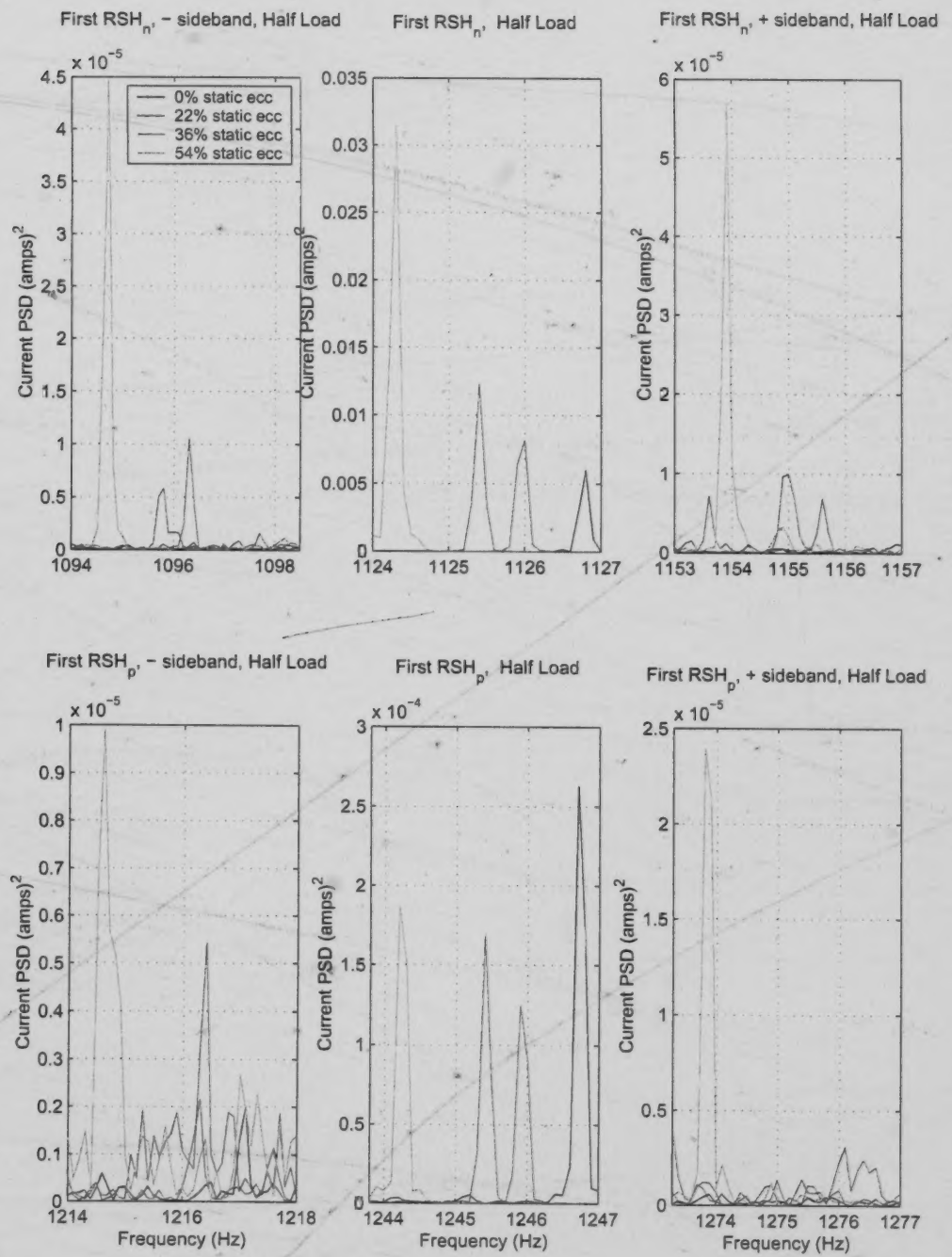
First RSH$_n$, − sideband, Half Load
First RSH$_n$, Half Load
First RSH$_n$, + sideband, Half Load
0% static ecc
22% static ecc
36% static ecc
54% static ecc
Current PSD (amps)^2
First RSH$_p$, − sideband, Half Load
First RSH$_p$, Half Load
First RSH$_p$, + sideband, Half Load
Frequency (Hz)

Figure 7.17: First RSH and sidebands at Half Load

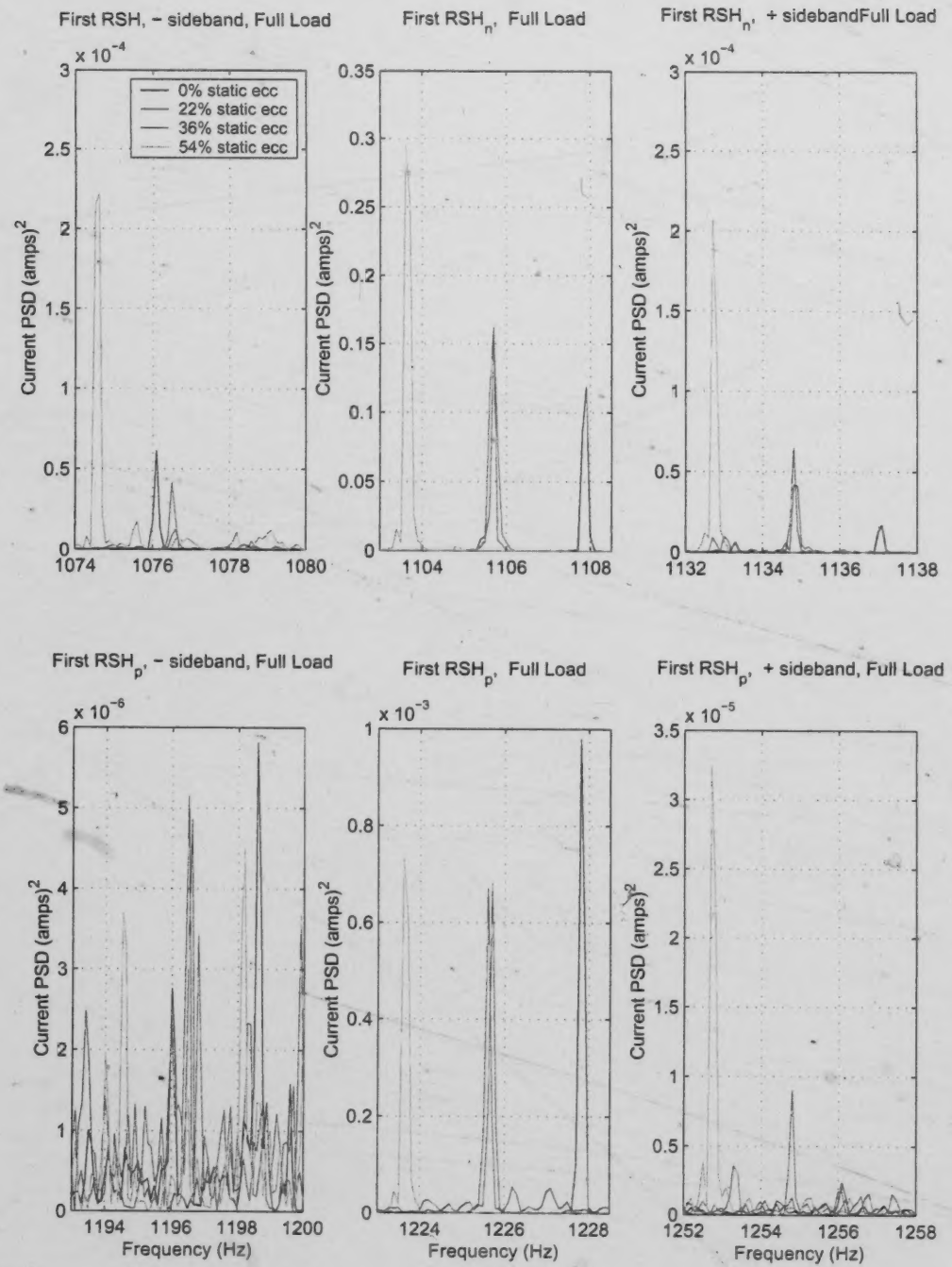
First RSH, − sideband, Full Load
First RSH$_n$, Full Load
First RSH$_n$, + sidebandFull Load
0% static ecc
22% static ecc
36% static ecc
54% static ecc
Current PSD (amps)^2
First RSH$_p$, − sideband, Full Load
First RSH$_p$, Full Load
First RSH$_p$, + sideband, Full Load
Frequency (Hz)

Figure 7.18: First RSH and sidebands at Full Load

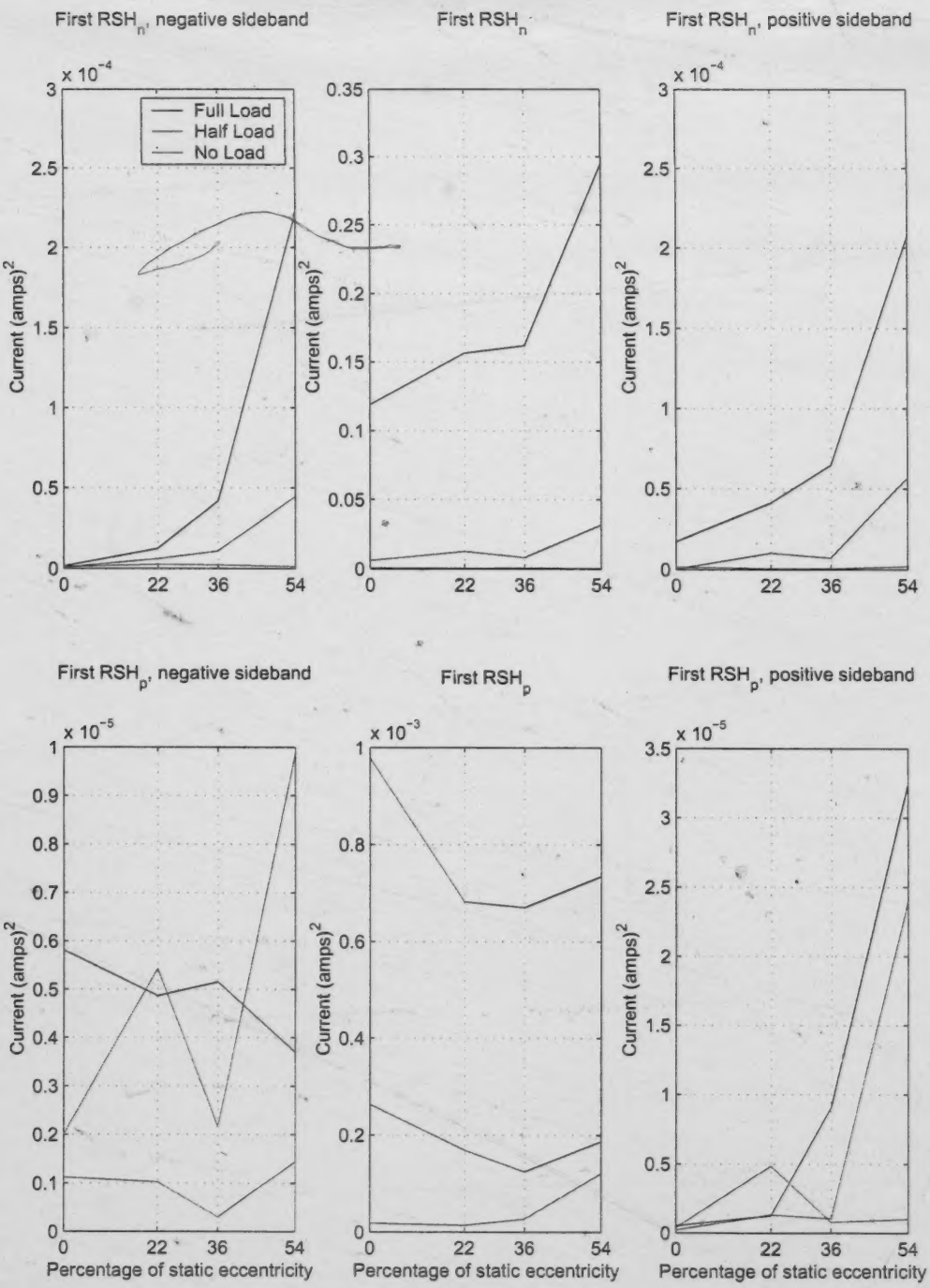

Figure 7.19: Variation in magnitude of the first $RSH_{n,p}$ and their sidebands at $\pm\omega_r$ when the motor is running at no load, half load and full load conditions and with different percentages of static eccentricity

Table 7.7 illustrates the frequencies that are affected the most when introducing various degrees of static eccentricity with the machine running at full load for various values of n and k of equation 7.2. Figure 7.20 illustrates these harmonics components.

Table 7.7: Rotor slot harmonic frequencies

k	time	1	3	5	7	19	21
1	-	1103.6				23.6	96.4
	+				1583.6		
2	-	2267.2	2147.2	2027.2			
2	+		2507.2		2747.2		

In all cases presented in this analysis, it has been seen that the magnitude of the harmonics at 54% static eccentricity has changed considerably with respect to ones with other levels of eccentricity. The frequency components observed and given by equation 7.2 should ideally be absent in the line current, however, due to machine supply and constructional unbalances, some of them are visible even in a healthy machine.

7.3.6 Experimental work with a damaged bearing

A bad rolling element in a motor may produce a slight radial movement of the rotor, disturbing the airgap geometry and introducing some degree of eccentricity in the motor. This radial movement changes the air gap permeance, thus a change in magnitude of those frequency components due to dynamic or static eccentricity should be observed in the spectrum. In order to investigate the effect of having a damaged bearing in the motor, the "healthy" bearing from the non-driving end of the machine is removed and it is replaced with a damaged bearing. The damaged bearing consists of a bearing of the same characteristics but with one the side seals removed. Aluminum chips are introduced inside the cage of the bearing in order to degrade the races and the surface of the bearing balls. The nature of the fault may introduce a small degree of eccentricity in the motor. The motor is reassembled and restored to service. Figure 7.21 presents the PSD current spectrum of the low frequency sidebands when the

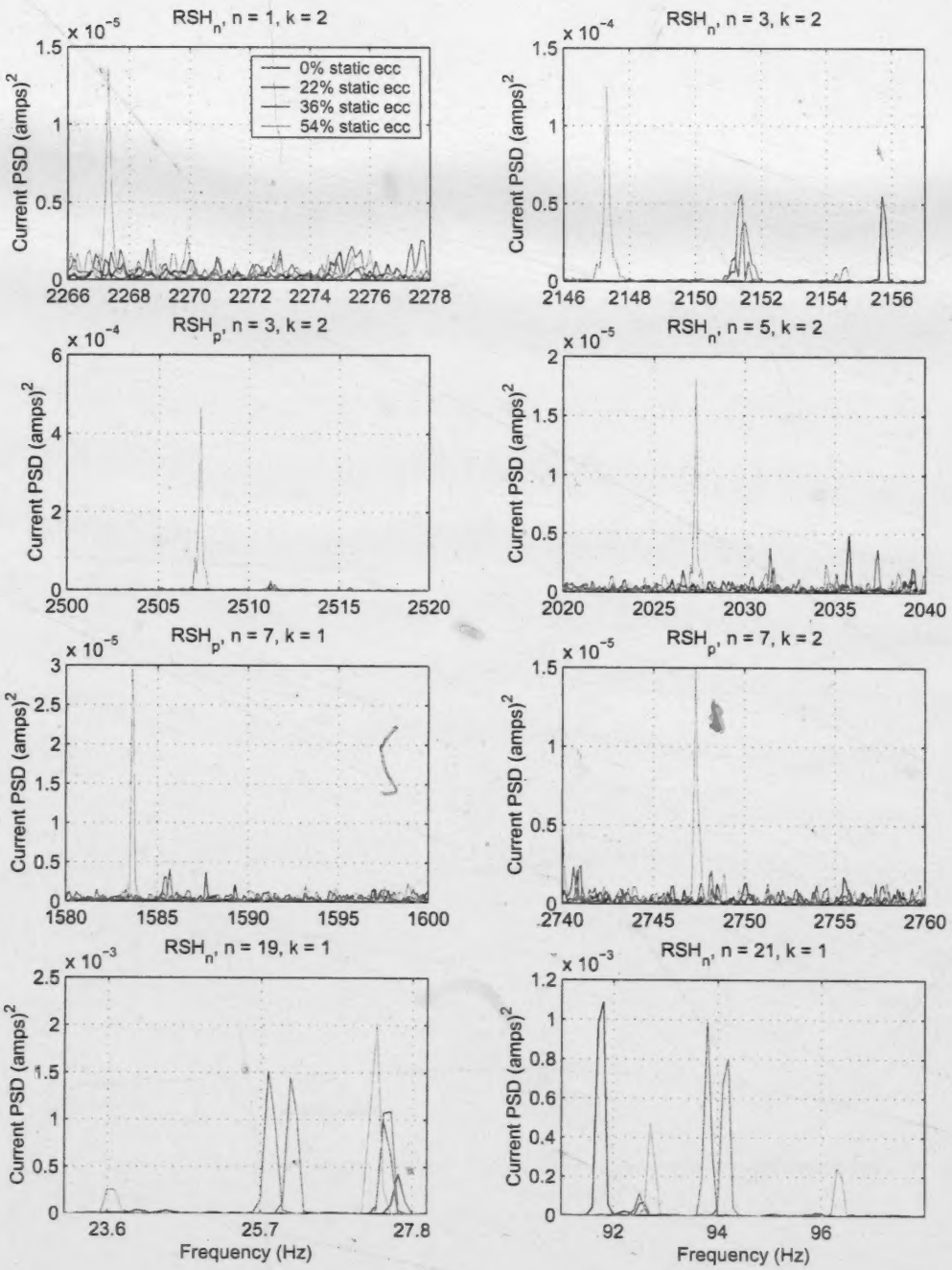
RSH_n, n = 1, k = 2
x 10^-5
0% static ecc
22% static ecc
36% static ecc
54% static ecc
Current PSD (amps)^2
RSH_n, n = 3, k = 2
x 10^-4
RSH_p, n = 3, k = 2
RSH_n, n = 5, k = 2
RSH_p, n = 7, k = 1
RSH_p, n = 7, k = 2
RSH_n, n = 19, k = 1
x 10^-3
RSH_n, n = 21, k = 1
Frequency (Hz)

Figure 7.20: RSH with different combinations of time harmonics n and integer k

motor is running at full load. A comparison of these harmonic components is made for two different cases: first, when the machine is running with a healthy bearing and a damaged bearing with 0% static eccentricity. Second, when the machine is running with a healthy bearing and a damaged bearing with 54% static eccentricity. Clearly, a gradual increase of magnitude is observed in both low frequency sidebands. The magnitude of the negative components with the damaged bearing at 0% static eccentricty increased by 8.16 dB. Similarly, an increase of static eccentricity to 54% and the presence of a damaged bearing produced an increase of magnitude in these components by 19.76 dB compared to a normal and healthy condition. Similarly, for the positive sideband, the magnitude of these components increased by 10 dB with the damaged bearing. An increase of static eccentricity to 54% and the presence of a damaged bearing produced an increased of these components of 27.92 dB.

A similar effect is produced at the $+\omega_r$ $RSH_{n,p}$ sidebands. Figure 7.22 depicts these components. It can be observed that the magnitude of the components for the RSH_n, positive sideband has increased when the damaged bearing is introduced. The same effect is observed when 54% static eccentricity is introduced. The RSH_p, positive sideband frequency components are present only when static eccentricity is introduced, but their magnitude has changed with the damaged bearing.

In summary, it is demonstrated that the magnitude of low frequency components, rotor slot harmonics and their sidebands will increase as the rotor static eccentricity increases when operating the machine at full load conditions. A slight asymmetry in the bearing introduces a small percentage of dynamic eccentricity in the machine's airgap that can be detected in the current spectra. Overall, the results indicate that current monitoring is a good method for detecting abnormal levels of airgap eccentricities in a medium size induction motor.

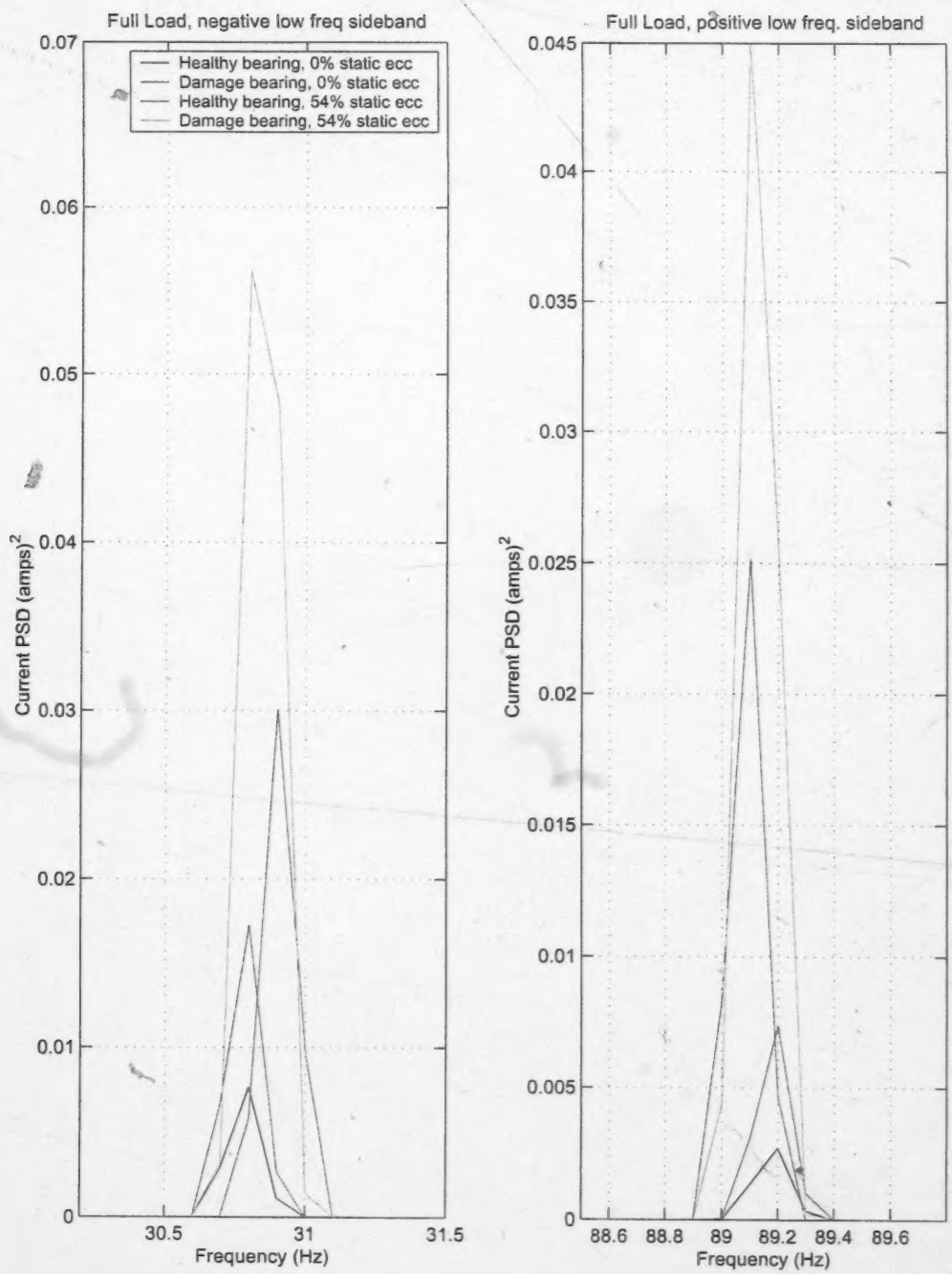

Figure 7.21: Comparison of the low frequency components when a damaged bearing and 54% eccentricity is introduced in the motor

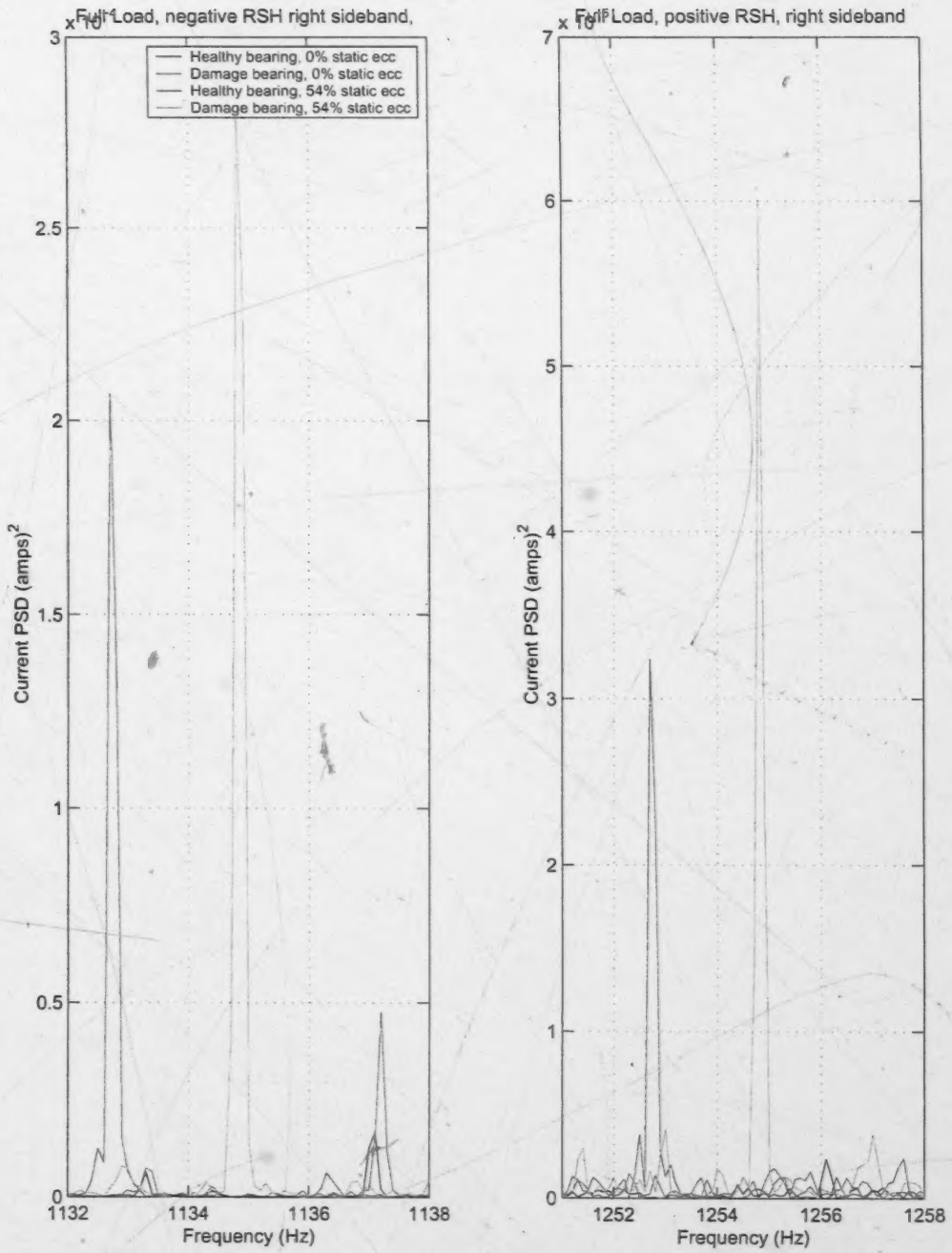

Figure 7.22: Comparison of the RSH positive sidebands when a damaged bearing and 54% eccentricity is introduced in the motor

Chapter 8

Conclusions and Future Work

This thesis evaluates a current monitoring scheme by means of stator current spectrum analysis as a reliable technique for condition monitoring and fault detection of mechanical faults in medium size random wound induction motors. Condition monitoring of electrical machines is of significant interest to industry since it provides immediate information of the equipment performance. Machinery operational reliability, optimal maintenance schedules, prevention of severe failures and maximum efficiency of a process are some of the benefits of an on-line condition monitoring system. In particular, the induction motor is the most widely used electrical machine in a great variety of industrial processes. Hence, condition monitoring of induction motors is an extensive area for research and development.

Presently, there are various possible condition monitoring schemes for fault detection in induction motors. Flux monitoring techniques give significant information of the performance of the motor, but its application is highly invasive and not totally practical in motors already in situ. Similarly, vibration spectrum analysis provides a reliable condition monitoring strategy for induction motors, especially for bearing related problems. However, the vibration sensors are relatively expensive and sometimes fragile. An on-line permanent condition monitoring scheme via vibration spectrum analysis is economically justified on large machinery. Stator current spectrum analysis represents a low cost, non invasive and powerful technique to identify on line motor performance and stator and rotor related failures.

The relationship between the mechanical displacement of the rotor against the

stator to the stator current spectra is determined by the flux density variation in the airgap of the motor. Any airgap eccentricity will produce abnormalities or deviations of the flux density distribution that in turn will induce current components in the stator winding of the machine. Consequently, it is observed that the stator supply current spectrum carries a great amount of information on the motor's performance.

The airgap flux density distribution around the periphery of the machine is derived as the product of the permeance function with the MMF generated in stator and rotor. The permeance function is defined as the inverse airgap function and it includes the effects of slotting both the stator and rotor along with airgap eccentricity conditions. The MMF is created by the spatial distribution of the windings in the machine when a time variant current is supplied. The flux density wave travels in space and time along the airgap of the motor, inducing current components in the stator winding that can be identified in the current spectrum.

Through applying the theoretical analysis to a computer simulation, the results show that the presence of low frequency components are indicative of either a dynamic or a static eccentricity condition in the machine and the existence of any small percentage of eccentricity in the motor will produce the apparition of such frequency components. An increase of magnitude of these components indicates that this condition has also increased. Similarly, the rotor and stator slot harmonic frequencies can be used to identify any progressive eccentric condition in the machine. The apparition of sidebands at $\pm\omega_r$ around the RSH or the SSH and their respective increment are also warning signals of the presence of this condition.

In order to verify the theory, a test rig composed of a medium size induction motor driving a DC generator was developed. Static eccentricity is introduced in the machine by a pair of new bearing housings that allow a radial movement of the rotor. The current monitoring scheme is achieved by means of a current probe connected to a data acquisition card and measurement and signal processing is done with LabView software in a PC.

The experimental results illustrate the current spectrum of a healthy motor running in three different load conditions. Rotor and stator slot harmonics, rotor and stator step harmonics and frequency components due to inherent levels of eccentricity conditions are identified in the spectrum. The introduction of static eccentricity in

the motor can be recognized by the change of magnitude of the frequency components given by the simulation results. It is observed that an increase of magnitude of these components is related to an increase in percentage of static eccentricity. Rotor and stator slot harmonics manifest the same behavior and the apparition of their sidebands becomes more notable when static eccentricity condition is of high percent.

Low frequency components and RSH due to the presence of time current harmonics are also identified in the spectrum. Furthermore, some combinations of these parameters (k =integer and n =time harmonics) give rise to the apparition of clearly identifiable harmonics when static eccentricity is introduced. The experimental results are in close agreement with the work carried out in large machines presented in [8] and [25] and for small machines as presented in [43].

Experimental work with a damaged bearing in the motor indicates that a small defect in the races or balls of the bearing introduces a dynamic eccentric variation of the rotor. These anomalies in the bearing generate a change in magnitude of the low frequency sidebands which verify that bearing failure introduces an eccentric condition in the motor.

Overall, current monitoring utilizes results of spectral analysis of the stator current to detect existing or incipient motor failures. The experimental results outlined in this thesis indicate that stator current spectrum analysis is an effective method to detect airgap eccentricities in the motor. Furthermore, its application should be widely considered as a primary tool to recognize the machine's condition since it can be easily implemented in different industrial environments for a reasonable cost. Future work should be aimed to predict the magnitude of the frequency components as a function of eccentricity. Hence, determination of unacceptable levels of increase in magnitude (e.g. dB) of those frequency components may avoid any severe damage to the induction motor.

Bibliography

[1] Yang D.M. *Development of novel intelligent condition monitoring procedures for rolling element bearings.* University of Aberdeen, PhD. thesis. Department of engineering, December 2001.

[2] M.E. Benbouzid. A review of induction motors signature analysis as a medium for fault detection. *IEEE Transactions on Industrial Electronics*, 47(5):984–992, October 2000.

[3] Chow M. Guest editorial special section on motor fault detection and diagnosis. *IEEE Transactions on Industrial Electronics*, 47(5):982–983, October 2000.

[4] Boldea I. and Nasar S. *The Induction Machine Handbook.* CRC Press LLC, 2002.

[5] W.T. Thomson and M. Fenger. Current signature analysis to detect induction motor faults. *IEEE Industry Applications Magazine*, pages 26–34, July/August 2001.

[6] P.J. Tavner and J. Penman. *Condition Monitoring of Electrical Machines.* Research Studies Press LTD., 1958.

[7] P. Vas. *Parameter Estimation, Condition Monitoring, and Diagnosis of Electrical Machines.* Oxford Science Publications, 1993.

[8] Cameron J.R., W.T. Thomson, and Dow A.B. Vibration and current monitoring for detecting airgap eccentricity in large induction motors. *IEE Proceedings*, 133(3):155–162, May 1986.

[9] Toliyat H.A. and S. Nandi. Fault diagnosis of electrical machines - a review. *IEEE International Electrical Machines and Drives Conference*, pages 219–221, May 1999.

[10] Isermann R. Supervision, fault-detection and fault-diagnosis methods an introduction. *Control Engineering Practice*, 5(5):638–652, 1997.

[11] Payne B., Bo L., Li. W., Gu F., and Ball A. The detection of faults in induction motors using higher order statistics. In *Electronic Proceedings of the 5th Annual Maintenance and Reliability Conference (MARCON 2001)*, Gatlinburg, Tennessee, USA, May 2001.

[12] M.E. Benbouzid, Vieira M., and Theys C. Induction motors' faults detection and localization using stator current advanced signal processing techniques. *IEEE Transactions on Power Electronics*, 14(1):14–22, January 1999.

[13] W.T. Thomson. A review of on-line condition monitoring techniques for three-phase squirrel-cage induction - past, present and future. *IEEE Symposium on Diagnostics for Electrical Machines, Power Electronics and Drives, Gijon, Spain*, pages 3–18, 1999.

[14] Bonnett A.H. and Soukup G.C. Cause and analysis of stator and rotor failures in three-phase squirrel cage induction motors. *IEEE Transactions on Industry Applications*, 28(4):921–937, July/August 1992.

[15] M.E. Benbouzid and Kliman G.B. What stator current processing-based technique to use for induction motor rotor faults diagnosis. *IEEE Transactions on Energy Conversion*, 18(2):238–244, June 2003.

[16] Nandi S. and Toliyat H.A. Novel frequency-domain based technique to detect stator interturn faults in induction machines using stator-induced voltages after switch-off. *IEEE Transactions on Industry Applications*, 38(1):101–109, January/February 2002.

[17] Stone G. and Kapler J. Stator winding monitoring. *IEEE Industry Applications magazine*, 4:15–20, September/October 1998.

[18] Penman J., Sedding H.G., Lloy B.A., and Fink W.T. Detection and location of interturn short circuits in the stator windings of operating motors. *IEEE Transactions on Energy Conversion*, 9:652–658, December 1994.

[19] Thomson W.T. On-line mcsa to diagnose shorted turns in low voltage stator windings of three-phase induction motors prior to failure. *IEEE International Electric Machines and Drives Conference, Boston, MA.*, pages 891–898, 2001.

[20] Kliman G.B. Noninvasive detection of broken bars in operating induction motors. *IEEE Transactions on Energy Conversion*, 3(4):873–879, December 1988.

[21] Haji M. and Toliyat H.A. Pattern recognition - a technique for induction machines rotor fault detection "broken bar fault". *IEEE International Electric Machines and Drives Conference, Boston, MA.*, pages 899–904, 2001.

[22] Thorse O.V. and Dalva M. Failure identification and analysis for high-voltage induction motors in the petrochemical industry. *IEEE Transactions on Industry Applications*, 14(1):810–818, July/August 1999.

[23] Yang D. and Penman J. Intelligent detection of induction motor bearing faults using current and vibration monitoring. In *Proceedings of the Congress on Condition Monitoring and Diagnostic Engineering Management*, pages 461–470, December 2000.

[24] W.T. Thomson and Barbour A. On-line current monitoring and application of a finite element method to predict the level of static airgap eccentricity in three-phase induction motors. *IEEE Transactions on Energy Conversion*, 13(4):347–357, December 1998.

[25] Thomson W.T., Rankin D., and Dorrell D.G. On-line current monitoring to diagnose airgap eccentricity in large three-phase induction motors -industrial case histories verify the predictions. *IEEE Transactions on Energy Conversion*, 14(4):1372–1378, December 1999.

[26] Donner G.L, Subler W.L., and Evon S.T. A motor primer -part 1. *IEEE Transactions on Industry Applications*, 36(5):1455–1466, September/October 2000.

[27] Johnson M.S. Vibration test for bearing wear. *ASHRAE Journal*, pages 52–56, October 2000.

[28] Yazici B. and Kliman G. An adaptative statistical time-frequency method for detection of broken bars and bearing faults in induction motors using stator current. *IEEE Transactions on Industry Applications*, 35(2):442–451, March/April 1999.

[29] A. Bellini, F. Filippetti, G. Franceschini, C. Tassoni, R. Passaglia, M. Saottini, G. Tontini, M. Giovannini, and A. Rossi. On-field experience with online diagnosis of large induction motors cage failures using mcsa. *IEEE Transactions on Industry Applications*, 38(4):1045–1052, July/August 2002.

[30] Schoen R.R and Habetler T.G. Effects of time-varying loads on rotor fault detection in induction machines. *IEEE Transactions on Industry Applications*, 31(4):900–906, July/August 1995.

[31] Walker J.S. *Fourier Analysis*. Oxford University Press, 1988.

[32] Finley W.R. and Hodowanec M.M. Sleeve versus antifriction bearings: selection of the optimal bearing for induction motors. *IEEE Transactions on Industry Applications*, 38(4):909–920, July/August 2002.

[33] Nsk website: http://www.am.nsk.com.

[34] Schoen R.R., Habetler T.G., Kamran F., and Bartfield R.G. Motor bearing damage detection using stator current monitoring. *IEEE Transactions on Industry Applications*, 31:1274–1279, Nov/Dec 1995.

[35] Ong R., Dymond J.H., Findlay R.D., and Szabados B. Shaft current in ac induction machine -an online monitoring system and prediction rules. *IEEE Transactions on Industry Applications*, 37:1189–1196, July/August 2001.

[36] Barker S. Avoiding premature bearing failure with inverter-fed induction motors. *IEE Power Engineering Journal*, 14(4):182–189, August 2000.

[37] Spotts M.F. *Design of Machine Elements.* Upper Saddre River, New Jersey 07458. Prentice Hall, 1998.

[38] Schiltz R.L. Forcing frequency identification of rolling element bearings. *Sound and Vibration*, pages 16–19, May 1990.

[39] V. Hamata and Heller B. *Harmonic Field Effects in Induction Machines.* Elsevier Scientific Publishing Company, 1977.

[40] Ferrah A., Hogben-Laing P.J., Bradley K.J., Asher G.M., and Woolfson M.S. The effect of rotor design on sensorless speed estimation using rotor slot harmonics identified by adaptive digital filtering using the maximum likelihood approach. *IEEE Industry Applications annual meeting, New Orleans, Louisiana*, pages 128–135, October 1997.

[41] McClay C.I. and Williamson S. The variation of cage motor losses with skew. *IEEE Industry Applications annual meeting*, 1:79–86, October 1998.

[42] The mathworks inc. *Matlab, the language of technical computing, version 6.1.0.450, release 12.1.* May 2001.

[43] Nandi S., Bharadwaj R.M., and Toliyat H.A. Performance analysis of a three-phase induction motor under mixed eccentricity condition. *IEEE Transactions on Energy Conversion*, 17(3):392–399, September 2002.

[44] Dorrel D. G., Thomson W.T., and Roach S. Analysis of airgap flux, current and vibration signals as a function of the combination of static and dynamic airgap eccentricity in 3-phase induction motors. *IEEE Transactions on Industry Applications*, 33(1):24–34, January/February 1997.

Appendix A: Simulation Program Listing

```
%This program calculates the FFT spectrum of the airgap flux density of an induction motor.
%The stator and rotor MMF are calculated according to the paramenters of the machine
%introduced by the user and the function defined in chapter 4. The skewed effect can also be included.
%The permeance function includes the effects of slotting the stator and the rotor
%along with dynamic and static eccentricity.
%Program created by: Sergio Bertani  with aid of Dr. Andy Knight
%University of Alberta, Edmonton, AB. CANADA
%Summer 2003.

clear all
we=60;                                  %Fundamental supply frequency
twopi=2*pi;
w=twopi*we;                             %Fundamental angular frequency
p=2;                                    %number of pole pairs
wr=(1-(60/1800))*w/p;                   %rotor angular speed
z1=48;                                  %number of stator slots
z2=40;                                  %number of rotor slots
freqrange=200;                          %Frequency range
tstep=1/(2*freqrange);
time_span=1.0;                          %time span of the waveforms
sample_size=time_span*2*freqrange;
t=linspace(0,time_span,sample_size);    %discrete points in time
angle=400                               %angular points around the machine
Manual=0;                               %if ==1, stator MMF is obtained by winding configuration
Series=1;                               %if ==1, stator MMF is obtained by calculation
stacklength=161e-3;                     %lenght of the machine 'm
radius=86.36e-3;                        % 'm
u0=4*pi*1e-7/1;                         %permeability of free space  'henries/meter = wb/(A*m)
g0=.92e-3;                              %average airgap  'm
el=twopi/z1;                            %determines the angle between stator slots
elr=twopi/z2;                           %determines angle between rotor slots
q=z1/(2*p*3);                           %slots per pole per phase in the stator
m=z2/p;                                 %number of phases in the rotor
qr=40/(p*m);                            %slots per pole per phase in the rotor
os=2.735e-3;                            %stator slot opening 'm
tds=11.3045e-3;                         %stator slot pitch   'm
otds=os/tds;
bes=0.23;                               %stator function of ratio o/g0
kc1=tds/(tds-1.6*bes*os);               %Stator Carter factor
or=1e-3;                                %rotor slot opening 'm
tdr=13.4201e-3;                         %rotor slot pitch   'm
otdr=or/tdr;
ber=0.048;                              %rotor function of ratio o/g0
kc2=tdr/(tdr-1.6*ber*or);               %Rotor Carter factor
barbit=linspace(0,stacklength,5);       %bit of lenght of the bar, divided in n points
long=length(barbit);
alphaz=barbit*elr/stacklength;          %increment of theta when the rotor is skewed
dalphaz=stacklength/(long-1);

a=[0:twopi/(angle):twopi-twopi/angle];  %angle in radians
ab1=[0+alphaz(1):twopi/(angle):twopi];            %angle in radian, a complete cycle
ab2=[0+alphaz(2):twopi/(angle):twopi+alphaz(2)];  %angle in radian, a complete cycle and
ab3=[0+alphaz(3):twopi/(angle):twopi+alphaz(3)];  %shifted to take into account the
ab4=[0+alphaz(4):twopi/(angle):twopi+alphaz(4)];  %skewed rotor
ab5=[0+alphaz(5):twopi/(angle):twopi+alphaz(5)];
```

```
j=1:sample_size;%+3;
fg=length(j);
%********** ------------------- ******************
%defining the MMF spatial disbritution of a induction machine
%The machine has concetric windings in 48 stator slots, 3phase, 4 poles.
if Manual==1
    N=18*90*sqrt(2)/(p*pi); %18 turns and magnitude of voltage
    a1=square(2*ab1-1*4*pi/48,((16-1)*el)/pi*100);
    a2=square(2*ab1-2*4*pi/48,((15-2)*el)/pi*100);
    a3=square(2*ab1-3*4*pi/48,((14-3)*el)/pi*100);
    a4=square(2*ab1-4*4*pi/48,((13-4)*el)/pi*100);

%a*,b*,c* are the coils for each phase. There are 4 coils per phase per pole. The square
%wave function generates the 'square' MMF spatial distribution for each coil. The square function
%defines a complete cycle with period 2pi. Since we need two cycle, the period is multiplied
%by 2 and also, we are substracting the first angle between slots for coil a1. It is multiplied
%by for to compensate for the 2 cylces that are taken into account. The duty cycle is also
%defined. It takes the percentage of the positive part of the wave. The postive part goes
%for coil a1 goes from slot 16 to 1. a2 goes from slot 15 to 2 and so on. The 1,2,3...12 is the
%space shifting the coils by that angle to start the square waveform.

b1=square(2*ab1-5*4*pi/48,((20-5)*el)/pi*100);
b2=square(2*ab1-6*4*pi/48,((19-6)*el)/pi*100);
b3=square(2*ab1-7*4*pi/48,((18-7)*el)/pi*100);
b4=square(2*ab1-8*4*pi/48,((17-8)*el)/pi*100);

c1=square(2*ab1-9*4*pi/48,((24-9)*el)/pi*100);
c2=square(2*ab1-10*4*pi/48,((23-10)*el)/pi*100);
c3=square(2*ab1-11*4*pi/48,((22-11)*el)/pi*100);
c4=square(2*ab1-12*4*pi/48,((21-12)*el)/pi*100);

phA1=zeros(fg,angle+1);phA2=zeros(fg,angle+1);phA3=zeros(fg,angle+1);phA4=zeros(fg,angle+1);
phB1=zeros(fg,angle+1);phB2=zeros(fg,angle+1);phB3=zeros(fg,angle+1);phB4=zeros(fg,angle+1);
phC1=zeros(fg,angle+1);phC2=zeros(fg,angle+1);phC3=zeros(fg,angle+1);phC4=zeros(fg,angle+1);

phA1=N*cos(w*t)'*a1;          %phase A
phA2=N*cos(w*t)'*a2;
phA3=N*cos(w*t)'*a3;
phA4=N*cos(w*t)'*a4;

phB1=N*cos(w*t + 2*pi/3)'*-b1;  %phase B
phB2=N*cos(w*t + 2*pi/3)'*-b2;
phB3=N*cos(w*t + 2*pi/3)'*-b3;
phB4=N*cos(w*t + 2*pi/3)'*-b4;

phC1=N*cos(w*t + 4*pi/3)'*c1;   %phase C
phC2=N*cos(w*t + 4*pi/3)'*c2;
phC3=N*cos(w*t + 4*pi/3)'*c3;
phC4=N*cos(w*t + 4*pi/3)'*c4;

sumaA=zeros(fg,angle+1);sumaB=zeros(fg,angle+1);sumaC=zeros(fg,angle+1);
sumaA=phA1+phA2+phA3+phA4;      %MMF created by coils phase A
sumaB=phB1+phB2+phB3+phB4;      %MMF created by coils phase B
sumaC=phC1+phC2+phC3+phC4;      %MMF created by coils phase C

mmft=zeros(fg,angle+1);
mmft(j,:)=(sumaA+sumaB+sumaC);  %Total MMF
```

```
clear ph*;clear suma*
end
%Stator and rotor MMF calculation
if Series==1
    n=1:10;
    kdp1=(sin(q*p*1*el/2)/(q*sin(1*p*el/2)));
    kdr1=(sin(qr*1*p*elr/2)/(qr*sin(1*p*elr/2)));
    kdrp(n)=(sin(qr*(20*n+1)*p*elr/2))/(qr*sin((20*n+1)*p*elr/2)); %rotor distribution factor
    kdrn(n)=(sin(qr*(20*n-1)*p*elr/2))/(qr*sin((20*n-1)*p*elr/2));

    mmf1=zeros(1,angle+1); mmfr1=zeros(1,angle+1,long); mmfp=zeros(12,angle+1); mmfn=zeros(12,angle+1);
    mmfrp=zeros(12,angle+1,long); mmfrn=zeros(12,angle+1,long); mmft=zeros(fg,angle+1);
    mmftr=zeros(fg,angle+1,long);

    for jk=1:sample_size;%+3
  mmf1(1,:)=((1/(p*pi))*kdp1*p*el/2)))*3*(4*18)*90*sqrt(2)*(cos(w*t(jk)-p*(1)*ab1)));
        mmfr1(1,:,1)=(((z2/p)/(p*pi))*kdr1*20*sqrt(2)*(cos(w*t(jk)-p*(1)*ab1)));
        mmfr1(1,:,2)=(((z2/p)/(p*pi))*kdr1*20*sqrt(2)*(cos(w*t(jk)-p*(1)*ab2)));
        mmfr1(1,:,3)=(((z2/p)/(p*pi))*kdr1*p*elr/2)))*20*sqrt(2)*(cos(w*t(jk)-p*(1)*ab3)));
        mmfr1(1,:,4)=(((z2/p)/(p*pi))*kdr1*20*sqrt(2)*(cos(w*t(jk)-p*(1)*ab4)));
        mmfr1(1,:,5)=(((z2/p)/(p*pi))*kdr1*20*sqrt(2)*(cos(w*t(jk)-p*(1)*ab5)));

        for n=1:10  %number of harmonics
            kdp(n)=(sin(q*p*(6*n+1)*el/2))/(q*sin((6*n+1)*p*el/2));
            kdn(n)=(sin(q*p*(6*n-1)*el/2))/(q*sin((6*n-1)*p*el/2));
            mmfp(n,:)=(1/(p*(6*n+1)*pi)*kdp(n)*4*18*3*90*sqrt(2)*(cos(w*t(jk)-p*(6*n+1)*ab1)));
            mmfn(n,:)=-(1/(p*(6*n-1)*pi)*kdn(n)*4*18*3*90*sqrt(2)*(cos(w*t(jk)+p*(6*n-1)*ab1)));
            mmfrp(n,:,1)=((z2/p)/(p*(20*n+1)*pi)*kdrp(n)*20*sqrt(2)*(cos(w*t(jk)-p*(20*n+1)*ab1)));
            mmfrn(n,:,1)=-((z2/p)/(p*(20*n-1)*pi)*kdrn(n)*20*sqrt(2)*(cos(w*t(jk)+p*(20*n-1)*ab1)));
            mmfrp(n,:,2)=((z2/p)/(p*(20*n+1)*pi)*kdrp(n)*20*sqrt(2)*(cos(w*t(jk)-p*(20*n+1)*ab2)));
            mmfrn(n,:,2)=-((z2/p)/(p*(20*n-1)*pi)*kdrn(n)*20*sqrt(2)*(cos(w*t(jk)+p*(20*n-1)*ab2)));
            mmfrp(n,:,3)=((z2/p)/(p*(20*n+1)*pi)*kdrp(n)*20*sqrt(2)*(cos(w*t(jk)-p*(20*n+1)*ab3)));
            mmfrn(n,:,3)=-((z2/p)/(p*(20*n-1)*pi)*kdrn(n)*20*sqrt(2)*(cos(w*t(jk)+p*(20*n-1)*ab3)));
            mmfrp(n,:,4)=((z2/p)/(p*(20*n+1)*pi)*kdrp(n)*20*sqrt(2)*(cos(w*t(jk)-p*(20*n+1)*ab4)));
            mmfrn(n,:,4)=-((z2/p)/(p*(20*n-1)*pi)*kdrn(n)*20*sqrt(2)*(cos(w*t(jk)+p*(20*n-1)*ab4)));
            mmfrp(n,:,5)=((z2/p)/(p*(20*n+1)*pi)*kdrp(n)*20*sqrt(2)*(cos(w*t(jk)-p*(20*n+1)*ab5)));
            mmfrn(n,:,5)=-((z2/p)/(p*(20*n-1)*pi)*kdrn(n)*20*sqrt(2)*(cos(w*t(jk)+p*(20*n-1)*ab5)));
        end

    mmft(jk,:)=sum(mmfp(:,:)+mmfn(:,:))+mmf1(1,:);  %total stator MMF
    mmftr(jk,:,1)=sum(mmfrp(:,:,1)+mmfrn(:,:,1))+mmfr1(1,:,1);  %total rotor MMF
    mmftr(jk,:,2)=sum(mmfrp(:,:,2)+mmfrn(:,:,2))+mmfr1(1,:,2);  %total rotor MMF
    mmftr(jk,:,3)=sum(mmfrp(:,:,3)+mmfrn(:,:,3))+mmfr1(1,:,3);  %total rotor MMF
    mmftr(jk,:,4)=sum(mmfrp(:,:,4)+mmfrn(:,:,4))+mmfr1(1,:,4);  %total rotor MMF
    mmftr(jk,:,5)=sum(mmfrp(:,:,5)+mmfrn(:,:,5))+mmfr1(1,:,5);  %total rotor MMF
    end
end
%Slotting Harmonics
v=1:2;  %number of slotting harmonics
Mrs(v)=(ber/g0)*(4./(v*pi).*(0.5+(v.*v*(otdr)^2./(0.78-2*v.*v*(otdr)^2))).*sin(1.6*pi*v*otdr));
Mss(v)=(bes/g0)*(4./(v*pi).*(0.5+(v.*v*(otds)^2./(0.78-2*v.*v*(otds)^2))).*sin(1.6*pi*v*otds));

rst=zeros(fg,angle+1,long); sst2=zeros(fg,angle+1); ese1=zeros(1,angle+1,long);
ede1=zeros(fg,angle+1,long); ede2=zeros(1,angle+1,long); ese2=zeros(fg,angle+1,long);
g1=zeros(fg,angle+1,long); PE1=zeros(fg,angle+1,long); g2=zeros(fg,angle+1,long);
PE2=zeros(fg,angle+1,long);
```

```
ese1(1,:,1)=g0*0.60*cos(ab1);
ese1(1,:,2)=g0*0.60*cos(ab2);
ese1(1,:,3)=g0*0.60*cos(ab3);
ese1(1,:,4)=g0*0.60*cos(ab4);
ese1(1,:,5)=g0*0.60*cos(ab5);
ede2(1,:,1)=g0*0.20*cos(ab1);

for d=1:2      %Stator slotting harmonics
    ss(d,:)=Mss(d)*cos(d*z1*(ab1));
    rs2(d,:)=Mrs(d)*cos(d*z2*ab1);
end

sst=1/(kc1*g0) - sum(ss(:,:));
rst2=1/(kc2*g0) - sum(rs2(:,:));  %rotor slotting in rotor ref. frame
for ga=1:sample_size;%+3
    for d=1:2
        %Rotor slotting harmonics
        rs(d,:,1)=Mrs(d)*cos(d*z2*(ab1+wr*t(ga)));
        rs(d,:,2)=Mrs(d)*cos(d*z2*(ab2+wr*t(ga)));
        rs(d,:,3)=Mrs(d)*cos(d*z2*(ab3+wr*t(ga)));
        rs(d,:,4)=Mrs(d)*cos(d*z2*(ab4+wr*t(ga)));
        rs(d,:,5)=Mrs(d)*cos(d*z2*(ab5+wr*t(ga)));
        ss2(d,:)=Mss(d)*cos(d*z1*(ab1+wr*t(ga))); %stator slotting harmonics in rotor ref. frame
    end

    rst(ga,:,1)=1/(kc2*g0) - sum(rs(:,:,1));
    rst(ga,:,2)=1/(kc2*g0) - sum(rs(:,:,2));
    rst(ga,:,3)=1/(kc2*g0) - sum(rs(:,:,3));
    rst(ga,:,4)=1/(kc2*g0) - sum(rs(:,:,4));
    rst(ga,:,5)=1/(kc2*g0) - sum(rs(:,:,5));
    sst2(ga,:)=1/(kc1*g0) - sum(ss2(:,:));

%Defining the dynamic eccentricities functions
    ede1(ga,:,1)=g0*0.20*cos(ab1+wr*t(ga));
    ede1(ga,:,2)=g0*0.20*cos(ab2+wr*t(ga));
    ede1(ga,:,3)=g0*0.20*cos(ab3+wr*t(ga));
    ede1(ga,:,4)=g0*0.20*cos(ab4+wr*t(ga));
    ede1(ga,:,5)=g0*0.20*cos(ab5+wr*t(ga));
    ese2(ga,:,1)=g0*60.0*cos(ab1+wr*t(ga));  %static ecc in the rotor ref. frame

%Defining the total permeance function
    g1(ga,:,1)=-ese1(1,:,1) - ede1(ga,:,1) + 1./sst(1,:) + 1./rst(ga,:,1) + g0;
    g1(ga,:,2)=-ese1(1,:,2) - ede1(ga,:,2) + 1./sst(1,:) + 1./rst(ga,:,2) + g0;
    g1(ga,:,3)=-ese1(1,:,3) - ede1(ga,:,3) + 1./sst(1,:) + 1./rst(ga,:,3) + g0;
    g1(ga,:,4)=-ese1(1,:,4) - ede1(ga,:,4) + 1./sst(1,:) + 1./rst(ga,:,4) + g0;
    g1(ga,:,5)=-ese1(1,:,5) - ede1(ga,:,5) + 1./sst(1,:) + 1./rst(ga,:,5) + g0;
    g2(ga,:,1)=-ede2(1,:,1) - ese2(ga,:,1) + 1./sst2(ga,:) + 1./rst2(1,:) + g0;

    PE1(ga,:,1)=u0./g1(ga,:,1);  %permeance function stator ref. frame
    PE1(ga,:,2)=u0./g1(ga,:,2);
    PE1(ga,:,3)=u0./g1(ga,:,3);
    PE1(ga,:,4)=u0./g1(ga,:,4);
    PE1(ga,:,5)=u0./g1(ga,:,5);
    PE2(ga,:,1)=u0./g2(ga,:,1);  %permeance function rotor ref. frame
end
```

```
nB1=zeros(fg,angle+1,long); nB1t=zeros(fg,angle+1); B1fft=zeros(fg,angle); nB1tfft=zeros(fg,angle);
nBfft=zeros(fg,angle); nB2=zeros(fg,angle+1,1); nB2tfft=zeros(fg,angle);

B1(:,:)=mmft(1:ga,:,1).*PE1(1:ga,:,1);    %%Flux density function due to stator
nB1(:,:,1)=(mmftr(1:ga,:,1)+mmft(1:ga,:)).*PE1(1:ga,:,1);    %total flux density: stator plus rotor
nB1(:,:,2)=(mmftr(1:ga,:,2)+mmft(1:ga,:)).*PE1(1:ga,:,2);
nB1(:,:,3)=(mmftr(1:ga,:,3)+mmft(1:ga,:)).*PE1(1:ga,:,3);    %total flux density: stator plus rotor
nB1(:,:,4)=(mmftr(1:ga,:,4)+mmft(1:ga,:)).*PE1(1:ga,:,4);    %total flux density: stator plus rotor
nB1(:,:,5)=(mmftr(1:ga,:,5)+mmft(1:ga,:)).*PE1(1:ga,:,5);    %total flux density: stator plus rotor
nB2(:,:,1)=(mmftr(1:ga,:,1)+mmft(1:ga,:)).*PE2(1:ga,:,1);    %total flux density: rotor ref. frame
nB1t(:,:)=sum(nB1(:,:,:),3)/long;   %total flux density with skew effect

for i=1:angle                              %Calculating the FFT
    B1fft(:,i)= fft(B1(:,i,1))/(sample_size/2);
    nB1tfft(:,i)= fft(nB1t(:,i))/(sample_size/2);
    nBfft(:,i)=fft(nB1(:,i,1))/(sample_size/2);
    nB2tfft(:,i)=fft(nB2(:,i,1))/(sample_size/2);
end

stator_b_fft(:,:)=abs(B1fft(:,:));   %stator flux density FFT spectrum
total_b_fft(:,:)=abs(nB1tfft(:,:));  %total flux density, unskewed rotor
total2_b_fft(:,:)=abs(nBfft(:,:));   %total flux density, skewed,
total3_b_fft(:,:)=abs(nB2tfft(:,:)); %total flux density, skewed,

clear B1fft;clear nB1tfft;clear nBfft;clear nB2fft

aa=[1:1:angle];
frequ=(0:freqrange/(sample_size/2):freqrange);

anglet_max=max(total_b_fft(60*time_span+1,:));
angles_max=max(stator_b_fft(60*time_span+1,:));

for po=1:angle
   if angles_max==stator_b_fft(60*time_span+1,po)
       maxsangle=po;
    end
    if anglet_max==total_b_fft(60*time_span+1,po)
       maxtangle=po;
    end
end
%calculating the amplitude of the FFT in dB
dbmaxstat=max(stator_b_fft(1:(2+sample_size)/2,maxtangle));
dbstat=10*log10(stator_b_fft(1:(2+sample_size)/2,maxtangle)/dbmaxstat);
dbmaxtot=max(total_b_fft(1:(2+sample_size)/2,maxtangle));
dbtot=10*log10(total_b_fft(1:(2+sample_size)/2,maxtangle)/dbmaxtot);
dbmaxtot2=max(total2_b_fft(1:(2+sample_size)/2,maxtangle));
dbtot2=10*log10(total2_b_fft(1:(2+sample_size)/2,maxtangle)/dbmaxtot2);
dbmaxtot3=max(total3_b_fft(1:(2+sample_size)/2,maxtangle));
dbtot3=10*log10(total3_b_fft(1:(2+sample_size)/2,maxtangle)/dbmaxtot3);

figure(5);plot(frequ,dbstat)
figure(6);plot(frequ,dbtot)
figure(7);plot(frequ,dbtot2)
figure(8);plot(frequ,dbtot3)
```

Appendix B: Bearing Housing Detailed Drawings

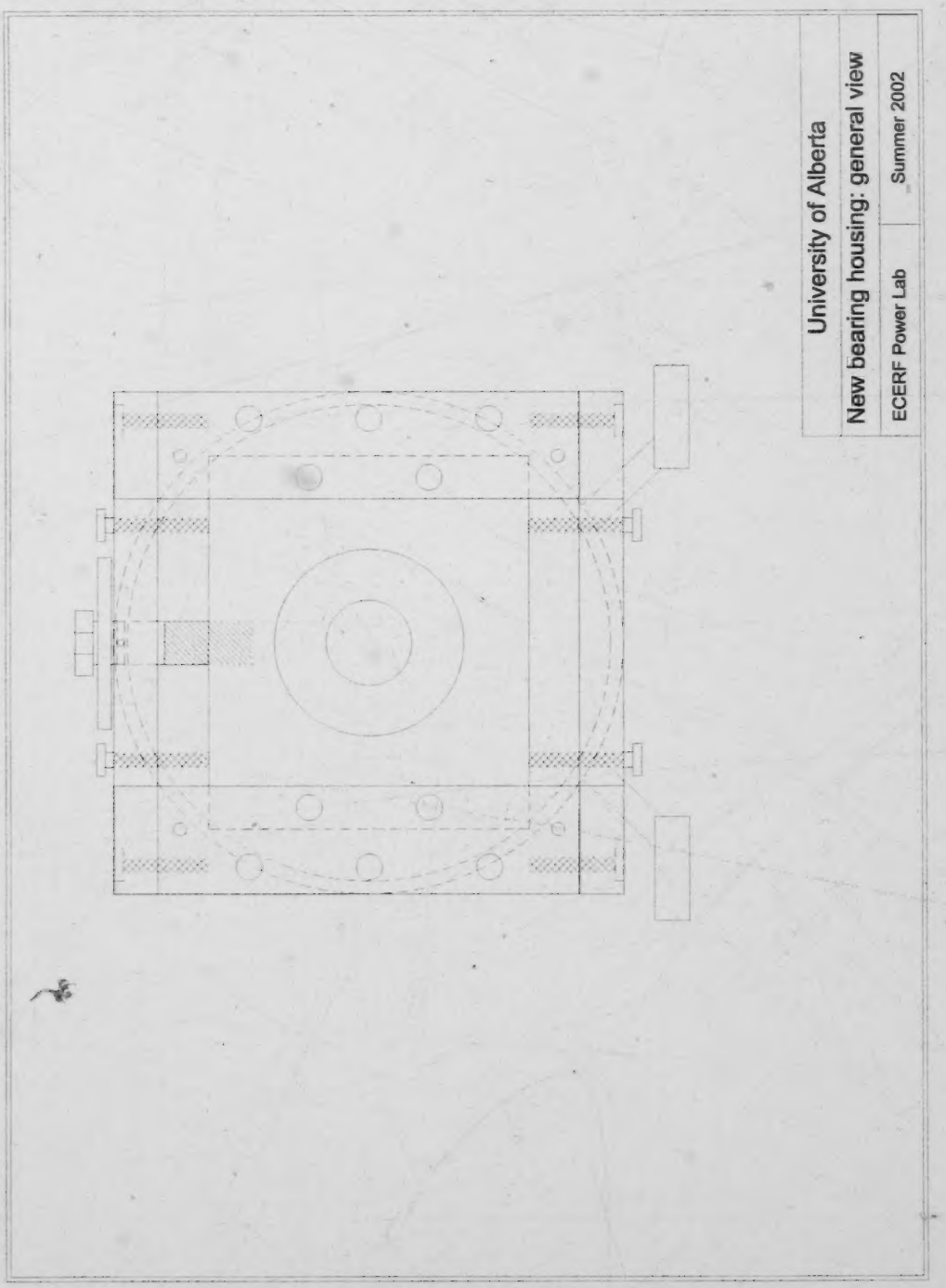

Figure 1: Bearing housing drawing a)

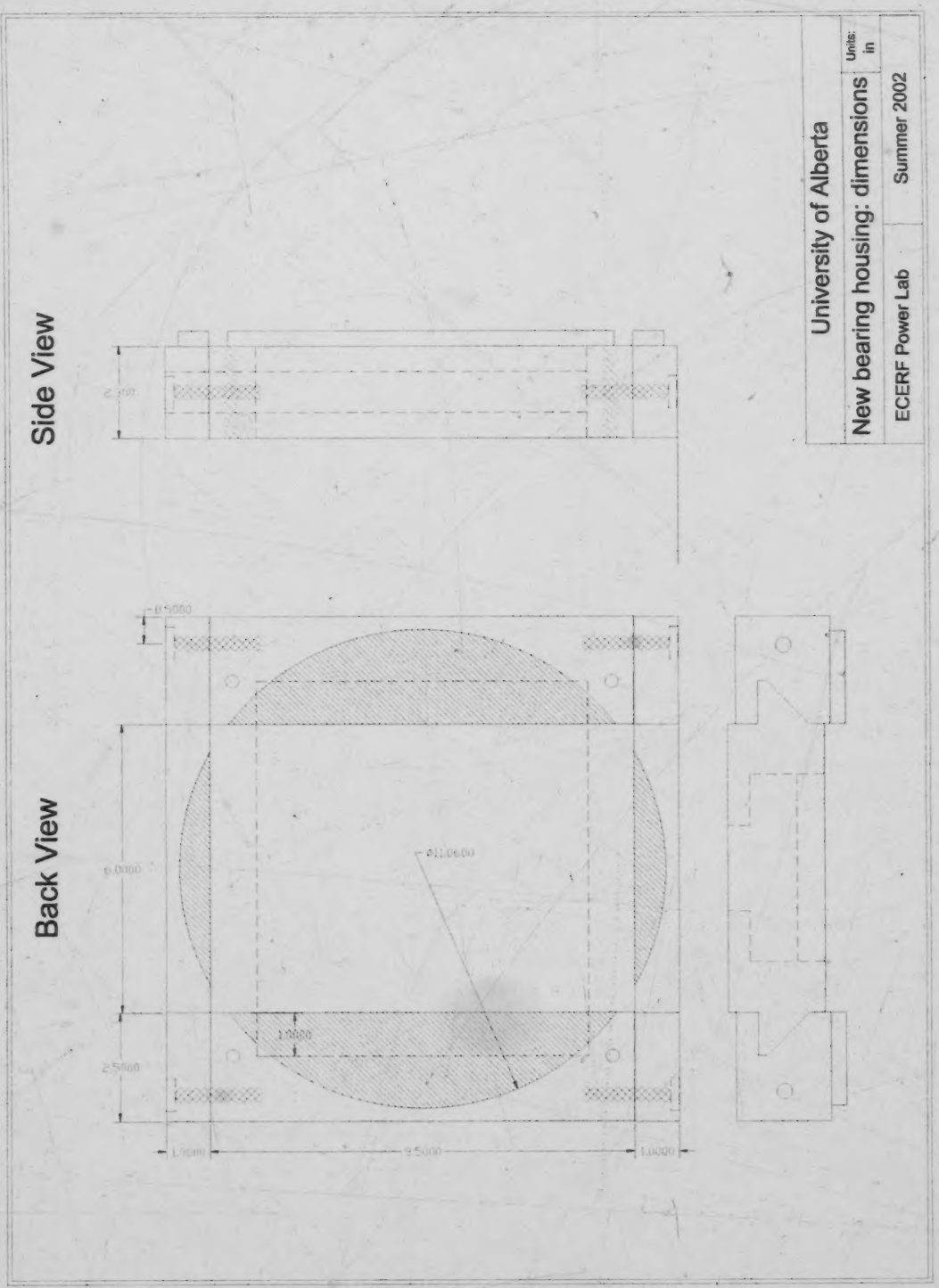

Figure 2: Bearing housing drawing b)

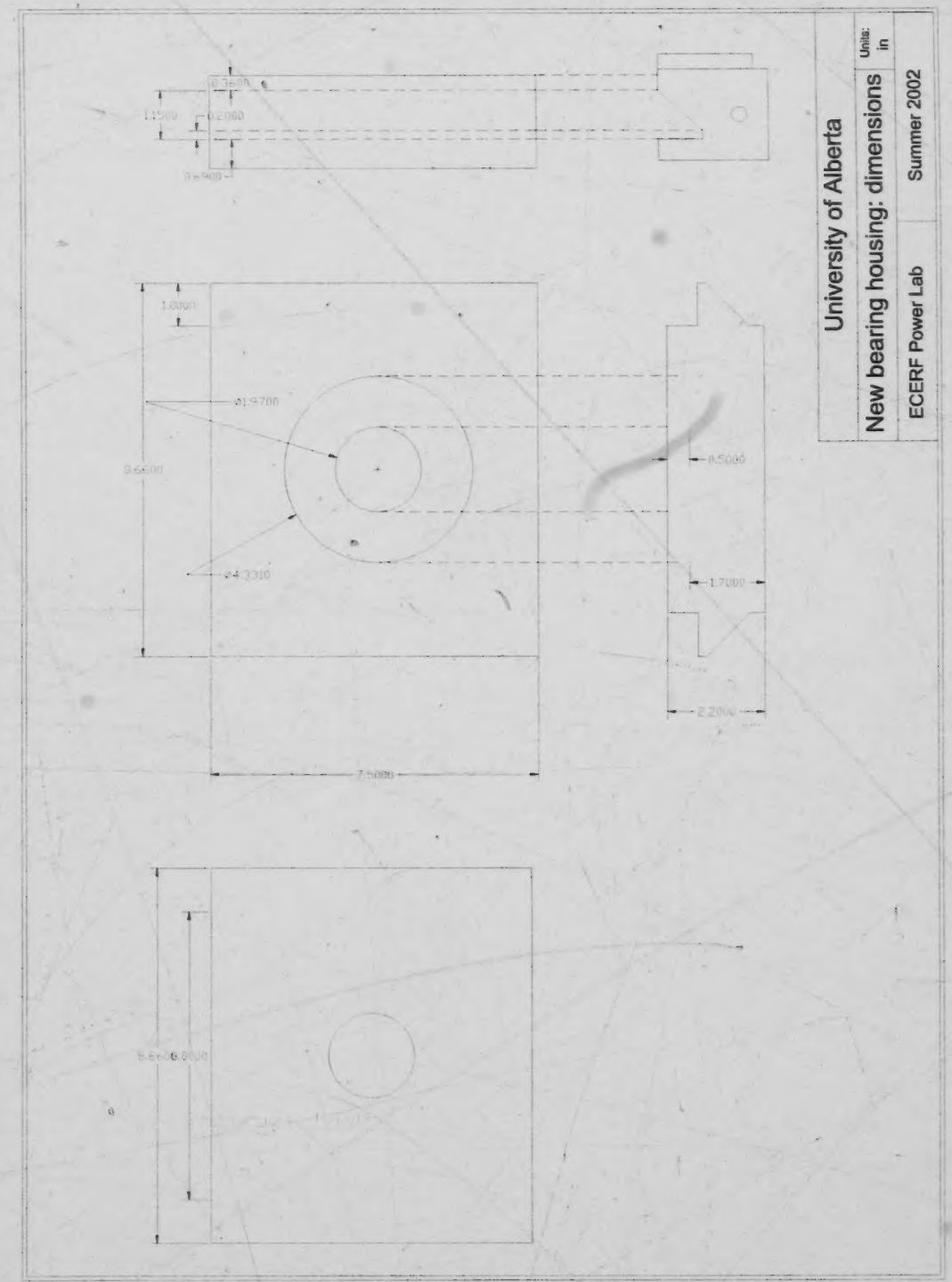

Figure 3: Bearing housing drawing c)

Curriculum Vitae

SI :Z

ser .ca

HIGHLIGHTS OF SKILLS AND QUALIFICATIONS

- Research in fault detection and condition monitoring of industrial electric motors by means of stator current spectrum analysis
- Good organizational skills and strong work ethic demonstrated by academic achievements and professional responsibilities
- Strong interpersonal and communications skills developed by working as laboratory assistant and community involvement
- Experience working in multidisciplinary and results oriented teams through my education and professional development

EDUCATION

Master of Science **University of Alberta** ***Edmonton, AB. CANADA***

- Graduated Fall 2003, Electrical and Computer Engineering Research Facility
- Received full graduate entrance scholarship and sponsorship from the Mexican government (CONACYT) to study in Canada (2001-2003)

B.Sc. Electrical Engineering ***Universidad Autonoma de Guadalajara, MEXICO***

- Specialization in Power Engineering
- Best overall academic average (9.8 on a 10 point scale)

PROFESSIONAL EXPERIENCE

Jan 2002 - May 2003 **University of Alberta** ***Edmonton, AB. CANADA***
Teaching Assistantship Positions:

- Electrical Machines laboratory assistant: - Supervise and evaluate students who are conducting experiments on synchronous motors, DC machines and induction motors
- Electrical Circuits laboratory assistant: - Evaluation and feed-back to students on basic circuitry design - Train students to manage voltmeters, ammeters and oscilloscopes
- Variable Speed AC Drives laboratory assistant: - Instruction and feed-back to students on the analysis, performance and applications of different types of AC drives

Feb 2000-Jul 2001 **Cereal Partners Worldwide CPW** ***Lagos de Moreno, Jal. MEXICO***
Process Engineer

- Upgraded machinery and implemented new set of high-pressure colorant pumps
- Performed and evaluated a production line maintenance program
- Leader of a team responsible for machinery operation and production

Aug-Dec 1999 **Power Quality Engineering** ***Guadalajara, Jal. MEXICO***
Junior Design Engineer (Co-op program)

- Designed power system protections for electrical substations
- Conducted relay configuration for the systems with SEL technology.
- Assessed CAD circuitry

COMMUNITY INVOLVEMENT

International Centre, University of Alberta
Bridges: Student speaker for global awareness ***November 2001-2003***

- Share my experience on cultural, social and regional topics about my native country to school groups and community organizations

International Centre Newsletter ***September 2002***

- Published an article about my experiences at the University of Alberta

Transitions program ***July-September 2002-2003***

- Facilitator for welcoming and orientating new foreign students to the University of Alberta and the city of Edmonton
- Peer leader volunteer responsible for organizing activities to help new students settle at the university campus

AFJ Christian campus student club, University of Alberta ***September 2001 - 2003***

- Student coordinator for local and community outreach
- Play a leadership role on service and commitment to foreign and local students

ADDITIONAL INFORMATION

Associations:

- Member of the Institute of Electrical and Electronics Engineers (IEEE): IEEE Power Engineering society member, IEEE Industrial Applications society member, IEEE Student-Branch President at Universidad Autonoma de Guadalajara, 1997

Computer Skills:

- Word Processing, Spreadsheets, AutoCAD, Matlab, LabView, PSpice, Power System Harmonic Analysis (PSA-H), Dreamweaver MX

Languages:

- Written and verbal fluency in English and Spanish